ASSISTED CONVECTIVE FLOW THROUGH NANOFLUID FILLED-FLAT PLATE SOLAR COLLECTOR: EFFECT OF SOLID VOLUME FRACTION

Rehena Nasrin*, Salma Parvin, and M.A. Alim

Department of Mathematics, Bangladesh University of Engineering and Technology,
Dhaka-1000, Bangladesh
*E-mail- rehena@math.buet.ac.bd

ABSTRACT: Numerical analysis of assisted convective laminar flow and heat transfer characteristics of nanofluid through a flat plate solar collector is performed in this article. The water-copper nanofluid is used as the heat transfer medium through the fluid passing pipe of the solar collector. The governing partial differential equations with proper boundary conditions are solved by Finite Element Method using Galerkin's weighted residual scheme. The behaviors of nanofluid related to the performance such as average rate of heat loss by the collector, percentage of collector efficiency, mid-height dimensional temperature, mean temperature, velocity, mean entropy generation and Bejan number are investigated systematically. These performance includes the variation of solid volume fraction (ϕ) of Cu nanoparticles of the flow. The results show that the better performance of heat loss through the pipe of the flat plate solar collector is found by using the solid volume fraction ϕ from 1% to 5%. Comparison and validation with the standard experimental/numerical data is given in brief.

Keywords: Forced convection, flat plate solar collector, finite element method, water based Cu nanoparticles, solid volume fraction.

1. INTRODUCTION

The fluids with solid-sized nanoparticles suspended in them are called "nanofluids." Applications of nanoparticles in thermal field are to **e**nhance heat transfer from solar collectors to storage tanks, to improve efficiency of coolants in transformers. Forced convection is a mechanism in which fluid motion is generated by an external source. The flat-plate solar collector is commonly used today for the collection of low temperature solar thermal energy. It is used for solar water-heating systems in homes and solar space heating.

Struckmann [1] analyzed flat-plate solar collector where efforts had been made to combine a number of the most important factors into a single equation and thus formulate a mathematical model which would describe the thermal performance of the collector in a computationally efficient manner. Martín et al. [2] also analyzed experimental heat transfer research in enhanced flat-plate solar collectors. To test the enhanced solar collector and compare with a standard one, an experimental side-by-side solar collector test bed was designed and constructed. Zambolin [3] theoretically and experimentally performed solar thermal collector systems and components. Testing of thermal efficiency and optimization of these solar thermal collectors were addressed and discussed in this work. Karuppa et al. [4] experimentally investigated a new solar flat plate collector. Experiments had been carried out to test the performance of both the water heaters under water circulation with a small pump and the results were compared. The results showed that the system could reach satisfactory levels of efficiency.

Selected nanofluids might improve the efficiency of direct absorption solar thermal collectors. To determine the effectiveness of nanofluids in solar applications, their ability to convert light energy to thermal energy must be known. That is, their absorption of the solar spectrum must be established. Enhancement of flat-plate solar collector thermal performance with silver nano-fluid was conducted by Polvongsri and Kiatsiriroat [5]. With higher thermal conductivity of the working fluid the solar collector performance could be enhanced compared with that of water. The solar collector efficiency with the nano-fluid was still high even the inlet temperature of the working fluid was increased. Natarajan & Sathish [6] studied role of nanofluids in solar water heater. Heat transfer enhancement in solar devices is one of the key issues of energy saving and compact designs. The aim of this paper

was to analyze and compare the heat transfer properties of the nanofluids with the conventional fluids. Physical properties of a solar water collector with water based nanofluid were studied by Nasrin and Alim [7].

Amrutkar et al. [8] studied solar flat plate collector analysis. The objective of their study was to evaluate the performance of FPC with different geometric absorber configuration. It was expected that with the same collector space higher thermal efficiency or higher water temperature could be obtained. Karanth et al. [9] performed numerical simulation of a solar flat plate collector using discrete transfer radiation model (DTRM)–a CFD Approach. Dynamics (CFD) by employing conjugate heat transfer showed that the heat transfer simulation due to solar irradiation to the fluid medium, increased with an increase in the mass flow rate. Also it was observed that the absorber plate temperature decreased with increase in the mass flow rate. Álvarez et al. [10] studied finite element modelling of a solar collector. A mathematical model of a serpentine flat-plate solar collector using finite elements was presented. The numerical simulations focused on the thermal and hydrodynamic behavior of the collector. Conduction convection radiation processes of a solar collector using FEA was performed by Moningi [11]. Radiation dominated the other two processes. It being non-linear phenomena required an iterative procedure to solve problems analytically, which was quite difficult. So, he tried to find the temperature distribution of the solar collector using FEA.

All thermofluidic processes involve irreversibilities and therefore incur an efficiency loss. In practice, the extent of these irreversibilities can be measured by the entropy generation rate. In designing practical systems, it is desirable to minimize the rate of entropy generation so as to maximize the available energy by Delavar and Hedayatpour [12]. Overall, the results have shown that the rate of entropy generation increases as the irreversibility distribution ratio increase. Moreover, for given values of the irreversibility distribution ratio, the entropy generation rate is determined by the heat transfer irreversibility and / or fluid friction irreversibility. Heat recovery from hot fluids in material processing industries is important for environmental and thermal management. The 'heatline' method of visualizing the true path of convection heat transfer was studied in Morega and Bejan [13]. It was developed as the convection counterpart (or the generalization) of the technique of heat flux lines used routinely in heat conduction.

In the light of above discussions, it is seen that there has been a good number of works in the field of heat loss system through a flat plate solar collector. In spite of that there is some scope to work with fluid flow, heat loss, entropy generation and enhancement of collector efficiency, using nanofluid. In this paper, we investigate numerically the forced convection flow through the riser pipe of a flat plate solar collector. The objective of this paper is to present temperature, streamfunction and heatfunction profile as well as heat loss system for the effect of solid volume fraction.

2. PROBLEM FORMULATION

Fig. 1 shows a typical liquid flat plate solar collector. A precise and detailed analysis of a flat plate solar collector is quite complicated because of the many factors involved. It is important to combine a number of the most important factors into a single equation. Thus formulation of mathematical model of Struckmann [1] is used in this study. Fig. 2 shows a schematic drawing of the heat flow through a collector. It is essential to measure its thermal performance, i.e. the useful energy gain or the collector efficiency. Thus it is necessary to define step by step the singular heat flow equations in order to find the governing equations of the collector system.

If I be the intensity of solar radiation, incident on the aperture plane of the solar collector having a collector surface area of A, then the amount of solar radiation received by the collector is:

$$Q_i = I.A \tag{1}$$

Basically, it is the product of the rate of transmission of the cover (λ) and the absorption rate of the absorber (κ). Thus,

$$Q_{recv} = I(\lambda\kappa)A \tag{2}$$

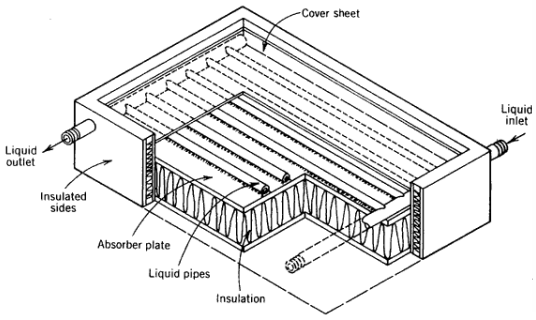

Fig. 1: Typical flat plate solar collector

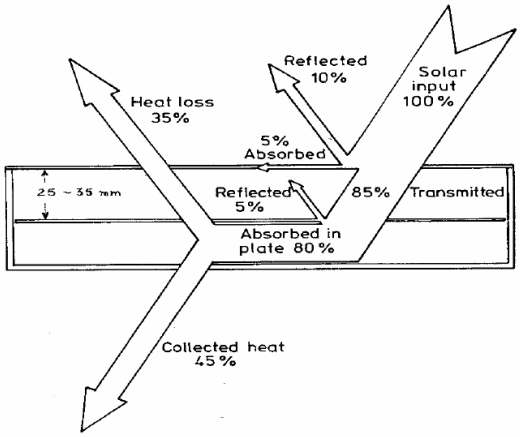

Fig.2: Heat transfer through a flat plate solar collector

As the collector absorbs heat its temperature is getting higher than that of the surrounding and heat is lost to the atmosphere by convection and radiation. The rate of heat loss (Q_{loss}) depends on the collector overall heat transfer coefficient (h) and the collector temperature.

$$Q_{loss} = hA(T_{col} - T_{amb}) \tag{3}$$

Thus, the rate of useful energy extracted by the collector (Q_{usfl}), expressed as a rate of extraction under steady state conditions, proportional to the rate of useful energy absorbed by the collector, less the amount lost by the collector to its surroundings. This is expressed as follows:

$$Q_{u\,sfl} = Q_{recv} - Q_{loss} = I(\lambda\kappa)A - hA(T_{col} - T_{amb}) \tag{4}$$

The heat flux per unit area q is now denoted as $\frac{Q_{u\,sfl}}{A} = q = I\lambda\kappa - h(T_{col} - T_{amb})$, where T_{col} and T_{amb} are collector average temperature and ambient temperature outside the collector respectively. It is also known that the rate of extraction of heat from the collector may be measured by means of the amount of heat carried away in the fluid passed through it. Thus

$$Q_{usfl} = mC_p(T_{out} - T_{in}) \tag{5}$$

Equation (4) may be inconvenient because of the difficulty in defining the collector average temperature. It is convenient to define a quantity that relates the actual useful energy gain of a collector to the useful gain if the whole collector surface were at the fluid mean temperature. This quantity is known as "the collector heat removal factor (F_R)" and is expressed as:

$$F_R == \frac{mC_p(T_{out} - T_{in})}{A\left[I(\lambda\kappa) - h(T_m - T_{amb})\right]} \tag{6}$$

where T_{in} and T_{out} are inlet and outlet fluid temperatures, respectively. Also $T_m = \frac{T_{out} + T_{in}}{2}$ is the fluid mean temperature.

The maximum possible useful energy gain in a solar collector occurs when the whole collector is at the inlet fluid temperature. The actual useful energy gain (Q_{usfl}), is found by multiplying the collector heat removal factor (F_R) by the maximum possible useful energy gain. This allows the rewriting of equation (4):

$$Q_{u\,sfl} = F_R A\left[I(\lambda\kappa) - h(T_m - T_{amb})\right] \tag{7}$$

Equation (7) is a widely used relationship for measuring collector energy gain and is generally known as the "**Hottel-Whillier-Bliss equation"**.

A measure of a flat plate collector performance is the collector efficiency (η) defined as the ratio of the useful energy gain (Q_{usfl}) to the incident solar energy. Using [3] it can be written as:

$$\eta = \frac{\text{useful gain}}{\text{available energy}} = \frac{mC_p\left(T_{out} - T_{in}\right)}{AI} \tag{8}$$

The instantaneous thermal efficiency of the collector is:

$$\eta = \frac{Q_{usfl}}{A\ I} = \frac{F_R\ A\ \left[I\left(\lambda\kappa\right) - h\left(T_m - T_{amb}\right)\right]}{AI} = F_R\left(\lambda\kappa\right) - F_R\, h\frac{\left(T_m - T_{amb}\right)}{I} \tag{9}$$

where m is the mass flow rate of the fluid flowing through the collector; C_p is the specific heat at constant pressure.

The present numerical system consists of a flat plate solar collector. A cross section along a riser pipe of the system considered in the present study is shown in Fig. 3. The fluid through the copper riser pipe is water-based nanofluid containing Cu nanoparticles. The nanofluid is assumed incompressible and the flow is considered to be laminar. It is taken that water and nanoparticles are in thermal equilibrium and no slip occurs between them. The flat-plate solar collector is an insulated metal box with a glass cover (called the glazing) and a dark-colored absorber plate. Flat-plate collectors are used for residential water heating and hydronic space-heating installations. A, L and d are the surface area of the collector, length and inner diameter of the riser pipe. The density of the nanofluid is approximated by the Boussinesq model. Only steady state case is considered. The computation domain is a fluid passing copper riser pipe which is attached ultrasonically to the absorber plate. The thermo-physical properties of the nanoparticle are taken from ogut [14] and given in Table 1.

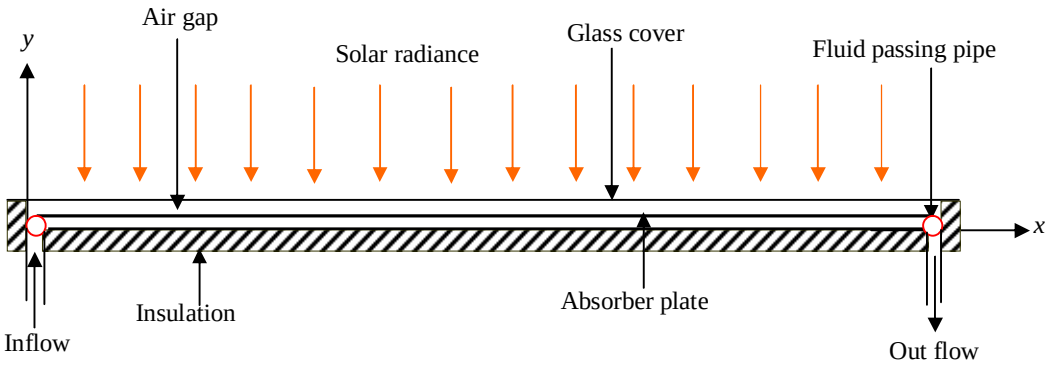

Fig. 3: Schematic diagram of the solar collector

The governing equations for laminar forced convection through a solar collector filled with water-copper nanofluid in terms of the Navier-Stokes and energy equation (non-dimensional form) are given as:

$$\frac{\partial U}{\partial X} + \frac{\partial V}{\partial Y} = 0 \tag{10}$$

$$U\frac{\partial U}{\partial X} + V\frac{\partial U}{\partial Y} = -\frac{\rho_f}{\rho_{nf}}\frac{\partial P}{\partial X} + \frac{\nu_{nf}}{\nu_f}\frac{1}{Re}\left(\frac{\partial^2 U}{\partial X^2} + \frac{\partial^2 U}{\partial Y^2}\right) \tag{11}$$

$$U\frac{\partial V}{\partial X} + V\frac{\partial V}{\partial Y} = -\frac{\rho_f}{\rho_{nf}}\frac{\partial P}{\partial Y} + \frac{\nu_{nf}}{\nu_f}\frac{1}{Re}\left(\frac{\partial^2 V}{\partial X^2} + \frac{\partial^2 V}{\partial Y^2}\right) \tag{12}$$

$$U\frac{\partial \theta}{\partial X} + V\frac{\partial \theta}{\partial Y} = \frac{1}{RePr}\frac{\alpha_{nf}}{\alpha_f}\left(\frac{\partial^2 \theta}{\partial X^2} + \frac{\partial^2 \theta}{\partial Y^2}\right) \tag{13}$$

where, $Pr = \frac{\nu_f}{\alpha_f}$ is the Prandtl number, $Re = \frac{U_{in} L}{\nu_f}$ is the Reynolds number, $\rho_{nf} = (1-\phi)\rho_f + \phi\rho_s$ is the density, $(\rho C_p)_{nf} = (1-\phi)(\rho C_p)_f + \phi(\rho C_p)_s$ is the heat capacitance, $\alpha_{nf} = k_{nf} / (\rho C_p)_{nf}$ is the thermal diffusivity, the viscosity of the nanofluid is considered by the Pak and Cho correlation [15] $\mu_{nf} = \mu_f (1 + 39.11\phi + 533.9\phi^2)$ and the thermal conductivity of Maxwell Garnett (MG) model [16] is $k_{nf} = k_f \frac{k_s + 2k_f - 2\phi(k_f - k_s)}{k_s + 2k_f + \phi(k_f - k_s)}$

The boundary conditions are:
at all solid boundaries: $U = V = 0$

at the upper and lower walls: $\frac{\partial\theta}{\partial Y} = -\frac{k_f}{k_{nf}}$

at the inlet boundary: $\theta = 0$, $U = 1$
at the outlet boundary: convective boundary condition $P = 0$
The above equations are non-dimensionalized by using the following dimensionless dependent and independent variables:

$$X = \frac{x}{L}, Y = \frac{y}{L}, U = \frac{u}{U_{in}}, V = \frac{v}{U_{in}}, D = \frac{d}{L}, P = \frac{p}{\rho_f U_{in}^2}, \theta = \frac{(T - T_{in})k_f}{qL} \quad (14)$$

The average Nusselt number (*Nu*) at the top surface is $Nu = \int_0^1 -\frac{k_{nf}}{k_f}\frac{\partial\theta}{\partial Y} dX$.

The mean bulk temperature and average sub domain velocity of the fluid inside the collector may be written as $\theta_{av} = \int \theta \, d\bar{V} / \bar{V}$ and $V_{av} = \int V \, d\bar{V} / \bar{V}$, where $\bar{V}$ is the volume of the collector.

Streamfunction ψ is obtained from velocity components U and V. The relationships between stream function and velocity components is $U = \frac{\partial\psi}{\partial Y}$, $V = -\frac{\partial\psi}{\partial X}$. *Thus*

$$\frac{\partial^2\psi}{\partial X^2} + \frac{\partial^2\psi}{\partial Y^2} = \frac{\partial U}{\partial Y} - \frac{\partial V}{\partial X} \quad (15)$$

Heatfunction ξ is obtained from conductive heat fluxes $\left(-\frac{\partial\theta}{\partial X}, -\frac{\partial\theta}{\partial Y}\right)$ *as well as convective heat fluxes (*$U\theta$, $V\theta$*). It satisfies the steady energy balance equation such that* $U\theta - \frac{\partial\theta}{\partial X} = \frac{\partial\xi}{\partial Y}$, $V\theta - \frac{\partial\theta}{\partial Y} = -\frac{\partial\xi}{\partial X}$. *Thus*

$$\frac{\partial^2\xi}{\partial X^2} + \frac{\partial^2\xi}{\partial Y^2} = \frac{\partial}{\partial Y}(U\theta) - \frac{\partial}{\partial X}(V\theta) \quad (16)$$

The entropy generation in the flow field is caused by the non-equilibrium flow imposed by boundary conditions. In the convection process, the entropy generation is due to the irreversibility caused by the heat transfer phenomena and fluid flow friction. According to Bejan [17], the dimensional local entropy generation, s_{gen}, can be expressed by:

$$s_{gen} = \frac{k_{nf}}{T_0^2}\left[\left(\frac{\partial T}{\partial x}\right)^2 + \left(\frac{\partial T}{\partial y}\right)^2\right] + \frac{\mu_{nf}}{T_0}\left[2\left(\frac{\partial u}{\partial x}\right)^2 + 2\left(\frac{\partial v}{\partial y}\right)^2 + \left(\frac{\partial u}{\partial x} + \frac{\partial v}{\partial y}\right)^2\right] \quad (17)$$

where $T_0 = \frac{T_{col} + T_{in}}{2}$.

In equation (17), the first term represents the dimensional entropy generation due to heat transfer ($s_{gen,h}$), while the second term represents the dimensional entropy generation due to viscous

dissipation ($s_{gen,v}$). By using dimensionless parameters presented in Eq. (14), the expression of the nondimensional entropy generation, S_{gen} can be written by:

$$S_{gen} = s_{gen}\frac{T_0 L^2}{k_f\left(T_{col}-T_{in}\right)^2}$$
$$= \frac{k_{nf}}{k_f}\left[\left(\frac{\partial\theta}{\partial X}\right)^2+\left(\frac{\partial\theta}{\partial Y}\right)^2\right]+\chi\frac{\mu_{nf}}{\mu_f}\left[2\left(\frac{\partial U}{\partial X}\right)^2+2\left(\frac{\partial V}{\partial Y}\right)^2+\left(\frac{\partial U}{\partial X}+\frac{\partial V}{\partial Y}\right)^2\right] \quad (18)$$
$$= S_{gen,h}+S_{gen,v}$$

Here $S_{gen,\,h}$ and $S_{gen,\,v}$ are the dimensionless entropy generation for heat transfer and viscous effect respectively. In Eq. (18), χ is the irreversibility factor which represents the ratio of the viscous entropy generation to thermal entropy generation. It is given as: $\chi = \frac{T_0\mu_f}{k_f}\frac{U_i^2}{\left(T_{col}-T_{in}\right)^2}$

The dimensionless average entropy generation, S for the entire computational domain is as follows:

$$S = \frac{1}{\overline{V}}\int S_{gen}\, d\overline{V} = S_{gen,h,m}+S_{gen,v,m} \quad (19)$$

where $\overline{V}$ is the volume occupied by the nanofluid and $S_{gen,\,h,\,m}$ and $S_{gen,\,v,\,m}$ are the average entropy generation for heat transfer and viscous effect respectively.

The Bejan number, *Be*, defined as the ratio between the entropy generation due to heat transfer by the total entropy generation, is expressed as $Be = \frac{S_{gen,h,m}}{S}$ (20)

It is known that the heat transfer irreversibility is dominant when Be approaches to 1. When Be becomes much smaller than 1/2 the irreversibility due to the viscous effects dominates the processes and if Be = 1/2 the entropy generation due to the viscous effects and the heat transfer effects are equal [17].

Table 1: Thermo physical properties of fluid and nanoparticles

Physical Properties	Fluid phase (Water)	Cu
C_p(J/kgK)	4179	352
ρ (kg/m^3)	997.1	8933
k (W/mK)	0.6	400
$\alpha\times10^7$ (m^2/s)	1.47	1163.1

3. NUMERICAL IMPLEMENTATION

The Galerkin finite element method (Taylor and Hood [18]) is used to solve the non-dimensional governing equations along with boundary conditions for the considered problem. The equation of continuity has been used as a constraint due to mass conservation and this restriction may be used to find the pressure distribution. In the Eqs. (11) - (13), the pressure *P* is eliminated by a constraint. The continuity equation is automatically fulfilled for large values of this constraint. Then the velocity components (*U*, *V*) and temperature (θ) are expanded using a basis set. The Galerkin finite element technique yields the subsequent nonlinear residual equations. Three points Gaussian quadrature is used to evaluate the integrals in these equations. The non-linear residual equations are solved using Newton–Raphson method to determine the coefficients of the expansions. The convergence of solutions is assumed when the relative error for each variable between consecutive iterations is recorded below the convergence criterion such that $\left|\psi^{n+1}-\psi^{n}\right|\le10^{-4}$, where *n* is the number of iteration and Ψ is a function of *U*, *V* and θ.

3.1 GRID INDEPENDENT TEST

An extensive mesh testing procedure is conducted to guarantee a grid-independent solution for *Re* = 400 and *Pr* = 6.6 in a solar collector. In the present work, we examine five different non-uniform grid systems with the following number of elements within the resolution field: 60, 240, 960, 3840 and 15360. The numerical scheme is carried out for highly precise key in the average Nusselt number for water-Cu nanofluid (ϕ = 5%) as well as base fluid (ϕ = 0%) for the aforesaid elements to develop an understanding of the grid fineness as shown in Fig. 4. The scale of the average Nusselt number for 3840 elements shows a little difference with the results obtained for the other elements. Hence, considering the non-uniform grid system of 3840 elements is preferred for the computation.

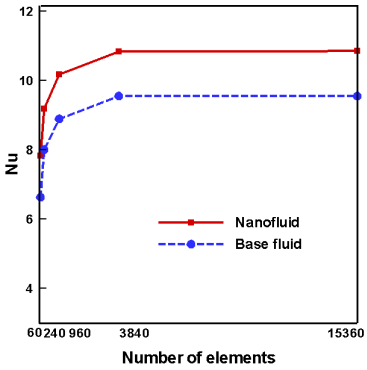

Fig. 4: Grid test for riser pipe of the solar collector

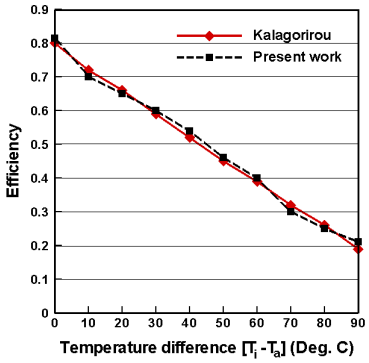

Fig. 5: Comparison of collector efficiency between present code and Kalagorirou [19] at I = 1000 W/m^2

3.2 CODE VALIDATION

The present numerical solution is validated by comparing the current code results for collector efficiency - temperature difference [T_i - T_a] profile of water with the graphical representation of Kalagorirou [19] for flat plate solar thermal collector at irradiation level 1000 W/m^2. Solar thermal collectors and applications were reported by Kalagorirou [19]. The mass flow rate per unit area for this validation was 0.015 (kg/s m^2). Fig. 5 demonstrates the above stated comparison. The numerical solutions (present work and Kalagorirou [19]) are in good agreement.

4. RESULTS AND DISCUSSION

In this section, numerical results of streamlines and isotherms for various values of solid volume fraction (ϕ) of the nanofluid with Cu /water nanofluid in a flat plate solar collector are displayed. The considered values of ϕ are ϕ = (1%, 3%, 5%, 7% and 10%) while the Reynolds number (*Re* = 400) and Prandtl number (*Pr* = 6.6) are chosen.

The performance of water based Cu nanoparticles i.e. water-Cu nanofluid on the dimensionless temperature, streamfunction and heatfunction are presented in Fig. 6 (a) - (c) while collector angle of inclination $\psi = 0^0$. The isotherms are smooth monotonic curves symmetric to the mid-horizontal axis. The temperature lines through the horizontal riser pipe become more heated for growing values of solid volume fraction ϕ from 1% to 5%. But after that there is almost no change in the thermal current activities for ϕ from 5% to 10%. This may be for the fact that more solid concentrated fluid velocity devalues. At ϕ = 1% the isothermal lines are distinct through the pipe. Rising solid volume fraction from 1% to 5% of the Cu nanoparticles enhances the thermal conductivity of the water-Cu nanofluid.

As a result isothermal lines become more heated and try to gather near the exit boundary. As well as the thermal boundary layer develops for ϕ = 5%. The strength of the flow circulation is much more deactivated for nanofluids respectively. In the velocity vector, the flow covers the whole domain of the pipe for nanofluid with 1% solid volume fraction. Then it concentrates near the middle of the riser pipe due to rising solid concentration of the water/Cu nanofluid. Heatlines are smooth and it is

observed that the lines are perfectly perpendicular to the isothermal lines and the upper and lower walls. This further indicates that the heat flow is conduction dominant. From the Fig. 6(c) it is clearly observed that the heatlines with greater strength become smaller in size at the middle of the flow pipe for ϕ = 5%. This happens due to more thermal conductive heat flux and as it is seen the case of the lowest solid volume fraction, the strength of heatline goes to low. The heatlines remain constant for further increasing ϕ from 5% to 10%. This means that major amount of heat flux or transport occurs for ϕ = 5% of water-Cu nanofluid.

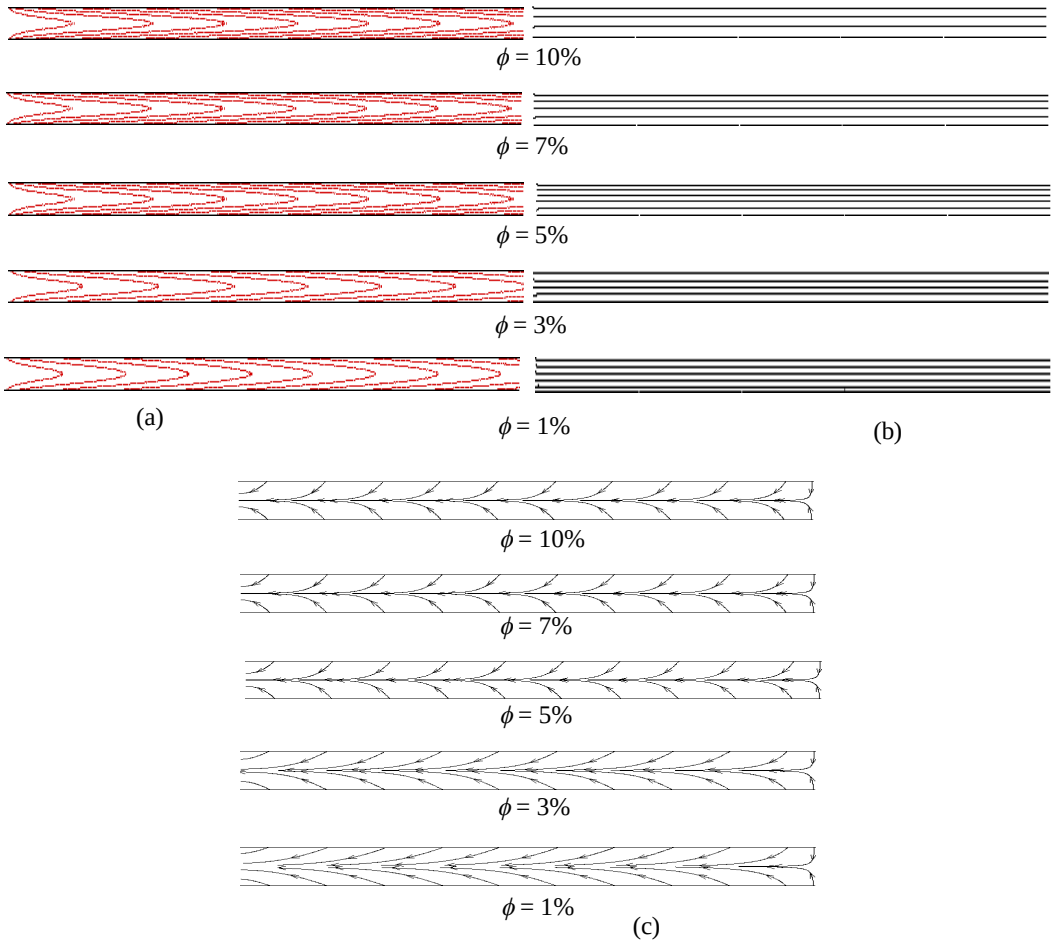

Fig. 6: Effect of ϕ on (a) temperature and (b) streamfunction and (c) heatfunction

The Nu - ϕ, θ_{av} - ϕ, η - ϕ, T - ϕ, S - ϕ and Be - ϕ profiles for water-Cu nanofluid as well as base fluid are depicted in Fig. 7(i)-(vi). From the plot of the average Nusselt number (Nu)-solid volume fraction (ϕ) it is observed that rate of heat transfer rises monotonically upto 5% of solid volume fraction. And then there is almost no change in Nu-ϕ profile for extra variation of ϕ from 5% to 10%. Here rate of heat transfer remains constant for clear water (ϕ = 0%) with the variation of ϕ. Heat transfer rate increases by 10% with the variation of ϕ from 1% to 5% of water-Cu nanofluid. Thus, adding more nanoparticles is not beneficial. Mean temperature grows sequentially for ϕ upto 5%. θ_{av} remains constant for further increasing values of solid volume fraction. It is well known that higher concentration of solid particle enhances thermal conductivity as well as temperature of the working water-Cu nanofluid. It is observed from Fig. 7 (iii) that rising solid volume fraction (upto 5%) enhances the collector efficiency. From 51% to 65% enhancement of collector efficiency is found in this case. Greater ϕ represents higher thermal conductivity simultaneously higher density properties

(i)

of the nanofluid. Thus motion of the nanofluid diminishes with enhancing ϕ. So heat transfer phenomena does not improved for further mixing nanoparticles with clear water.

Dimensional temperature of water-copper nanofluid at mid-height of the riser pipe is shown in Fig. 7 (iv). The inlet temperature of fluid is maintained at 300K and then it increases gradually with the contact of heated solid upper and lower boundaries of the riser pipe. And finally the output temperature of fluid becomes 344K, 348K, 351K, 354K, 354K and 354K for ϕ = 0%, 1%, 3%, 5%, 7% and 10% respectively. The entropy generation increases by ϕ upto 5%. The increment of nanoparticles, in terms of enhancing heat transfer rate, observed in Fig. 7(v) is also obtained in terms of increasing entropy production. It is seen that for a fixed value of $\psi = 0^0$, the *S* enhances slightly as the volume fraction of nanoparticles increases upto 5%. This result is to be expected since the addition of a greater number of nanoparticles increases the thermal conductivity and viscosity of the working fluid. The higher thermal conductivity results in a smaller temperature gradient within the riser pipe of the flat plate solar collector, and thus the average entropy generation caused by heat transfer irreversibility increases. The greater viscosity of the working fluid increases the local entropy generation due to fluid friction irreversibility. After the level of ϕ = 5%, there is no change in mean entropy generation. From *Be*-ϕ profile it is seen that increasing *Be* is observed for increasing solid volume fraction of copper nanoparticles within the level 0% to 5%. For further increment of ϕ no variation is found in the Bejan number.

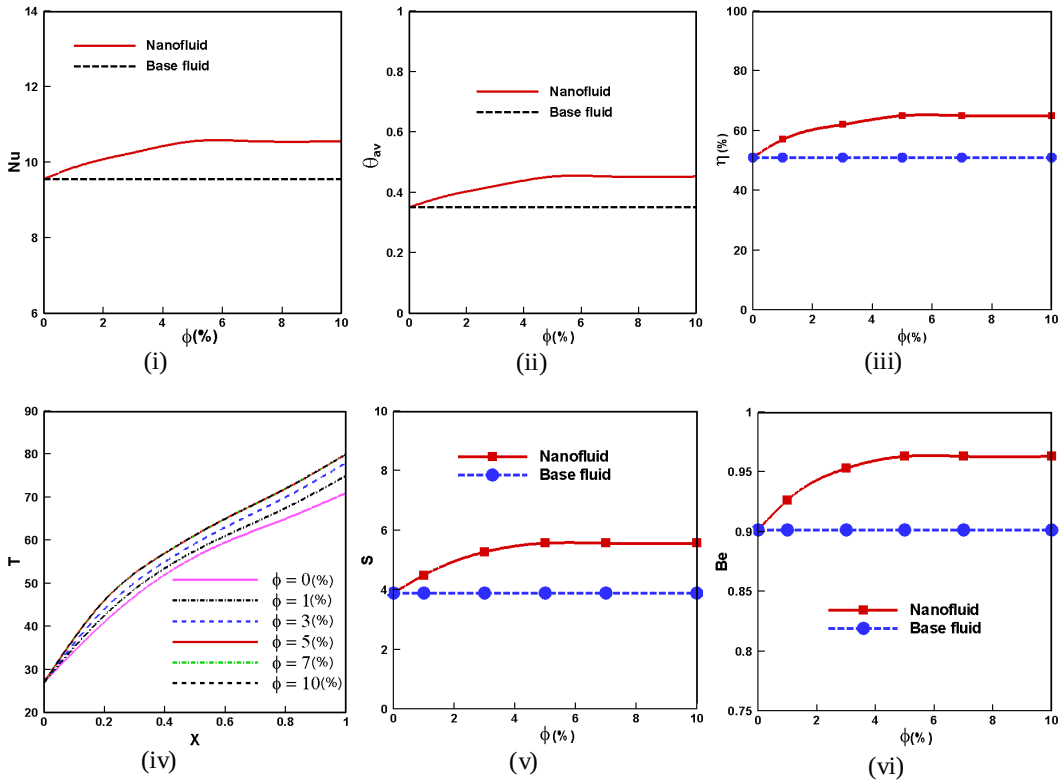

Fig. 7: Effect of solid volume fraction on (i) *Nu*, (ii) θ_{av}, (iii) η, (iv) *T*, (v) *S* and (vi) *Be*

5. ACKNOWLEGDEMENT

This work is done in the Department of Mathematics, Bangladesh University of Engineering & Technology, Dhaka, Bangladesh.

6. CONCLUSION

The influences of solid volume fraction and angle of inclination on forced convection boundary layer flow inside the riser pipe of a flat plate solar collector with water-Cu nanofluid are accounted. Various ϕ have been considered for the temperature, flow and heat flux fields as well as heat transfer rate, mean bulk temperature, collector efficiency, mid-height temperature, mean entropy generation and Bejan number of the fluids through the riser pipe. The results of the numerical analysis lead to the following conclusions:

- The structure of the fluid isotherms, streamlines and heatlines through the solar collector is found to appreciably depend upon ϕ.
- Cu nanoparticles with ϕ = 5% are established to be most effective in enhancing performance of heat loss rate than base fluid.
- Collector efficiency is obtained higher for 5% solid volume fraction.
- Mean temperature diminishes for both fluids with rising ϕ and ψ upto 5%.
- Average velocity decreases due to growing ϕ.
- Mean entropy generation is obtained higher for rising ϕ .
- Bejan number approaches to 1 for solid volume fraction variation upto 5%.

REFERENCES

[1] F. Struckmann, Project Report 2008 MVK160 Heat and Mass Transport, Lund, Sweden, 2008.

[2] R.H. Martín, A.G. Pinar, J.P. García, Solar Thermal Applications, World Renewable Energy Congress, 3844-3851, 2011.

[3] E. Zambolin, Scuola di Dottorato di Ricerca in Ingegneria Industriale, Indirizzo Fisica Tecnica, 2011.

[4] R.R.T. Karuppa, P. Pavan and D.R. Rajeev, Research J. of Engg. Sciences, 1, 4, 1-8, 2012.

[5] S. Polvongsri and T. Kiatsiriroat, The 2nd TSME Int. Conf. on Mech. Engg., Krabi, 2011.

[6] E. Natarajan & R. Sathish, Int. J. Adv. Manuf. Techno., DOI 10.1007/s00170-008-1876-8.

[7] R. Nasrin, M.A. Alim and A.J. Chamkha, Heat Transfer—Asian Research, 42 1, 73-88, 2013

[8] S.K. Amrutkar, S. Ghodke, Dr.K.N. Patil, IOSR J. of Engg., 2, 2, 207-213, 2012.

[9] K.V. Karanth, M.S. Manjunath, N.Y. Sharma, Proc. of the World Congress on Engg., III, WCE 2011, London, U.K, 2011.

[10] Álvarez, M.C. Muñiz, L.M. Varela, O. Cabeza, Int. Conf. on Renew. Energies and Power Quality, Granada (Spain), 2010.

[11] M.K. Moningi, University of Massachusetts, Amherst.

[12] M.A. Delavar, M. Hedayatpour, Heat Transf.-Asian Res., 41 (7), pp. 580–600, 2012

[13] AL.M. Morega and A. Bejan, Int. J. of Heat and Mass Trans. 36, 16, 3957-3966, 1993.

[14] E.B. Ogut, , Int. J. of Thermal Sci., 48, 11, 2063-2073, 2009.

[15] B.C. Pak, Y. Cho, Experim. Heat Trans. 11, 151-170, 1998.

[16] J.C. Maxwell-Garnett, Philos. Trans. Roy. Soc. A 203, 385-420, 1904.

[17] Bejan, Boca Raton:CRC Press;1996.

[18] Taylor, P. Hood, Computer and Fluids 1, 73–89, 1973.

[19] S.A. Kalogirou, Progress in Energy and Combustion Science, 30, 231–295, 2004.

NUMERICAL AND EXPERIMENTAL STUDIES OF WINGLET TYPE PLASMA ACTUATOR INDUCED FLOW IN QUIESCENT AIR

[1]A.N.M. Mominul Islam Mukut, [2]Hiroshi Mizunuma & Obara Hiromichi, [3]Takehiko Segawa

[1]Department of Mechanical Engineering, Dhaka University of Engineering & Technology (DUET), Gazipur-1700. Bangladesh
E-mail: mukut@duet.ac.bd
[2]Department of Mechanical Engineering, Tokyo Metropolitan University, 1-1Minami-Osawa, Hachioji, Toky 0192-0397,
[3]National Institute of Advanced Industrial Science and Technology (AIST), Tsukuba, Japan

ABSTRACT: The term plasma actuator has now been a part of popular research topics in the field of fluid dynamics due to some advantages of simple mechanism, easy maintenance, having no moving parts, low cost and fast response compared with the other actuator as blow, suction or heating process. The surface Dielectric Barrier Discharge (DBD) plasma actuator is known to be effective for flow control process. This paper mainly investigated the winglet type DBD plasma actuators having exposed electrode on both sides in quiescent air that was investigated by means of particle image velocimetry. Numerical simulation has been carried out to clarify near electrode flow. High induced velocity has been found near the exposed electrode that was placed at leading edge. From two exposed electrodes on both sides of plasma actuator, two separate jet flows were induced after the winglet trailing edge and were unified to a single jet. The electrode location influenced the maximum velocity downstream. The longer distance between trailing edge and embedded electrode reduced the downstream unified velocity.

Keywords: dielectric barrier discharge plasma actuator, velocity profile, flow control, PIV, jet, CFD.

1. INTRODUCTION

Dielectric barrier discharges (DBD) has seen a tremendous growth in Aerodynamic flow control in the past years because of its demonstrated ability and potential applications. Some of them are active airfoil leading edge separation control [1,2], control of airfoil dynamic stall [3], bluff body flow control [4,5], boundary layer flow control [6,7], high-lift applications [8], and turbomachinery flow control [9,10] and so on. A simple plasma actuator is consists of two electrodes that are separated by a dielectric material. One of the electrode is typically exposed to the air. The other electrode is fully covered by the dielectric material. The electrodes are supplied with an AC voltage with enough magnitude which ionize the air over the covered electrode. Here the term ionized referred as plasma, that's why they are referred as Plasma Actuator. The word ''plasma'' was introduced into the physics literature by Langmuir [11] to denote an electrically neutral region of gas discharge. The ionized air, in the presence of the electric field produced by the electrode geometry produce a body force vector that acts on the ambient (neutrally charged) air. The body force is the mechanism for active aerodynamic control.

The plasma actuator is thin and controllable electrically. Until now, the actuators have been mounted on the wall surface. For example, a vortex generator is located on the wall surface and LEBU (Large Eddy Break Up) device is located with some distance from the wall surface. These devices are composed of thin plates which are requested to have simple structure and minimum sizes. Thus the applications are limited to passive flow control. On the other hand, the DBD plasma actuator has a function of the active control in spite of its simple structure. Thus if the combination of those passive control devices and the DBD plasma actuator is possible, it is expected to bring a new active method for the flow control. From this point of view, a plate-like plasma actuator located with a distance from the wall surface has been developed. In this paper three type of plasma actuators are numerically and experimentally evaluated to figure out their effectiveness so that they can be used as vortex generator to control flow separation.

2. METHOD

2.1. EXPERIMENTAL SETUP

Three types of Plasma Actuator (hereafter PA) namely: Leading edge type PA (hereafter L PA), Middle edge type PA (hereafter M PA) and Trailing edge type PA (hereafter T PA) have been used in experiment. All of these PA have two exposed electrode on both sides with common embedded electrode; convectional two PA have been glued together to make our desired PA. The width and chord length of mini-plate wing were 96 mm and 19.6 mm respectively. The electric wind was generated in the absence of external flow by the plasma actuator. Exposed and grounded electrodes were separated by a Kapton thin wing plate. Detailed dimension (all in mm) have been shown in figure 1. The induced flow was compared as a function of the distance from the leading edge to the actuator position. Due to use of two exposed electrodes plasma was created on both sides of actuator surfaces. All experiments were carried out with a frequency of 5 kHz and the corresponding applied voltage were 2.5kV, 3kV, 3.5kV and 4kV respectively. All experiments were carried out in absence of external air flow. Particle image velocimetry (PIV) was employed to quantify the behavior of the flow field during testing at AIST Tsukuba [12]. The laser is a 25 mJ/pulse, double-pulse Nd-YAG laser (New Wave Research Co. Ltd., MiniLase II: 20 Hz). A horizontal laser sheet would strike at the midpoint of the plasma actuator from downstream, so that only suction side was in shadow. This enabled us to measure a two dimensional cross-section of the flow field around the airfoil. The schematic diagram of PIV experiment is presented in figure 2.

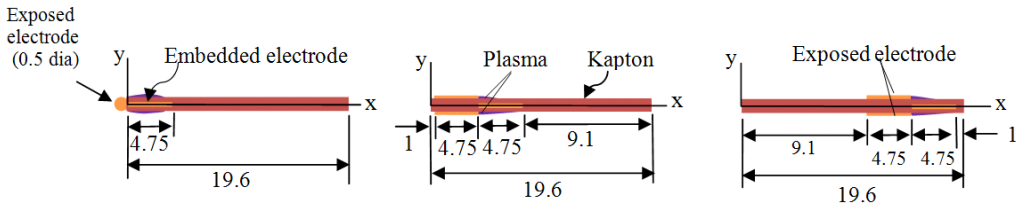

Fig.1: Plasma actuator geometry (a) L PA (b) M PA (c) T PA (all dimension in mm)

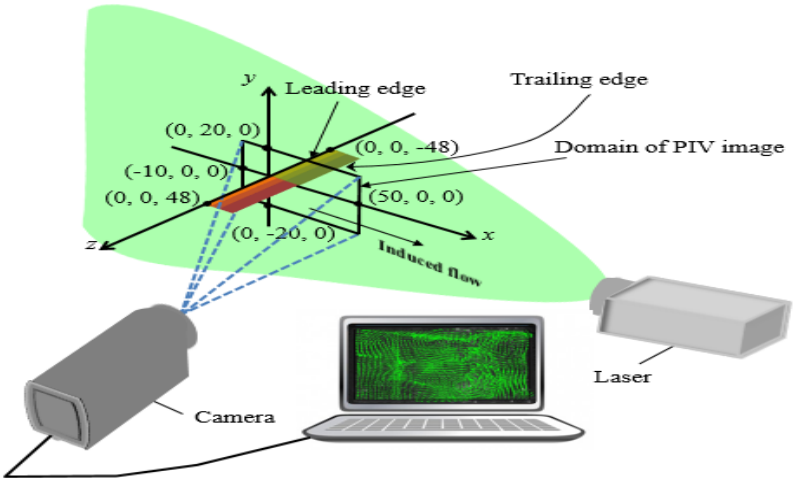

Fig.2: PIV setup

2.2. SIMULATION

Due to use of two exposed electrodes, plasma was created on both side of embedded electrode. In PIV measurement, near electrode flow was not so clear due to plasma and laser light reflection, that's why numerical simulation has been carried out to investigate flow at near electrode region. Modeling and numerical simulation have been performed based on Suzen et al. [13]. Main concept is same but difference in PA size and shape. Embedded type electrode was used by Suzen but in this present research mini plate wing type PA has been investigated, this is due to the aim of combining active and passive flow control device.

The governing equation is 2D unsteady Navier-Stocks equation which is given below:

$$\frac{\partial u}{\partial x}+\frac{\partial u}{\partial y}=0 \quad (1)$$

$$\frac{DU}{Dt}=-\frac{1}{\rho}\nabla p+\mu\nabla^2 U+\overrightarrow{f_B} \quad (2)$$

Finite volume method has been applied in simulation using above mentioned equations. PHOENICS 2009 solver which is developed by CHAM, UK has been used for simulation. Simulation is consist of two steps: at first the electrical potential, the particle charge density and EHD forces were calculated, secondly using those values induced flow was calculated. Unsteady flow was considered in simulation and the average was calculated to compare those with the time averaged result of PIV.

3. RESULT AND DISCUSSION

Due to pair of exposed electrodes, two induced flow were produced that were unified downstream of winglet. The image resolution of PIV in near electrode region was not good due to huge reflection of LASER light and plasma from both exposed electrodes, the thickness of winglet type PA was 0.75mm only. Hence numerical simulation has been carried out to figure out near electrode flow.

Downstream unification of two separate induced flows was clear and well match in both experiment and simulation; to clarify it, peak velocity have been shown in figure 3. Comparison of experimental and simulated velocity profiles have been plotted at x=30mm and is presented in figure 4 for 4kV applied voltage only. Velocity profiles from simulation showed two peaks which were absent in experimental velocity profiles this is because in simulation mesh grid is too smaller than experimental measuring grid as a result two peaks clearly appeared in simulation.

Figure 5 represents the maximum induced flow velocity for each type of PA with corresponding applied voltage to figure out the effect of applied voltage on induced flow velocity. The induced velocity increases with the voltage because the electric field also increases and ions undergo higher Columbian forces [14].

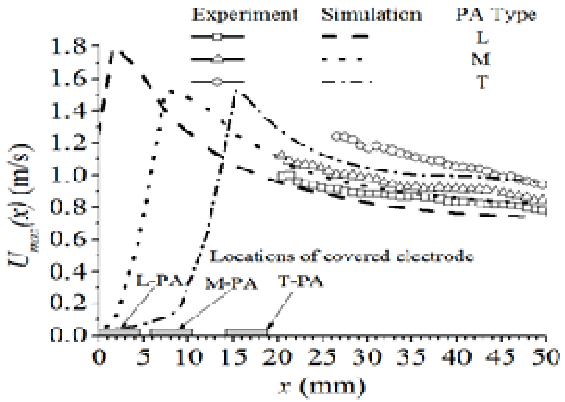

Fig.3: Peak velocity Umax(x) as a function of x.

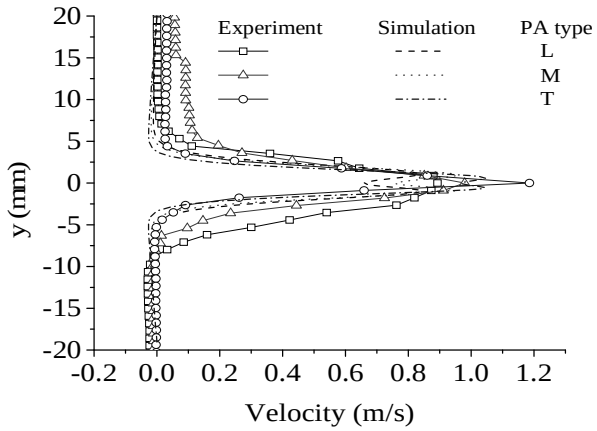

Fig.4: Simulated and experimental velocity profile [voltage amplitude is ±4kV]

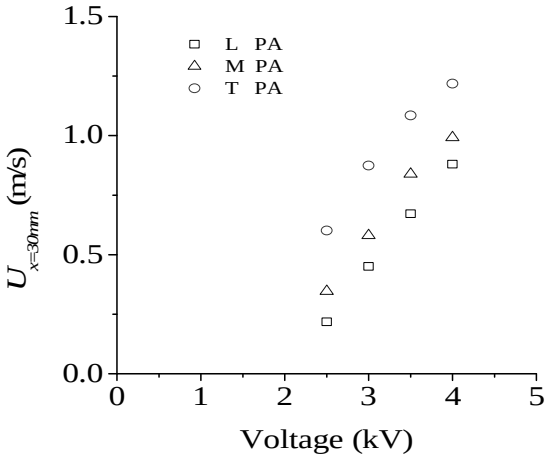

Fig.5: Change of induced velocity (at x=30mm) with applied voltage

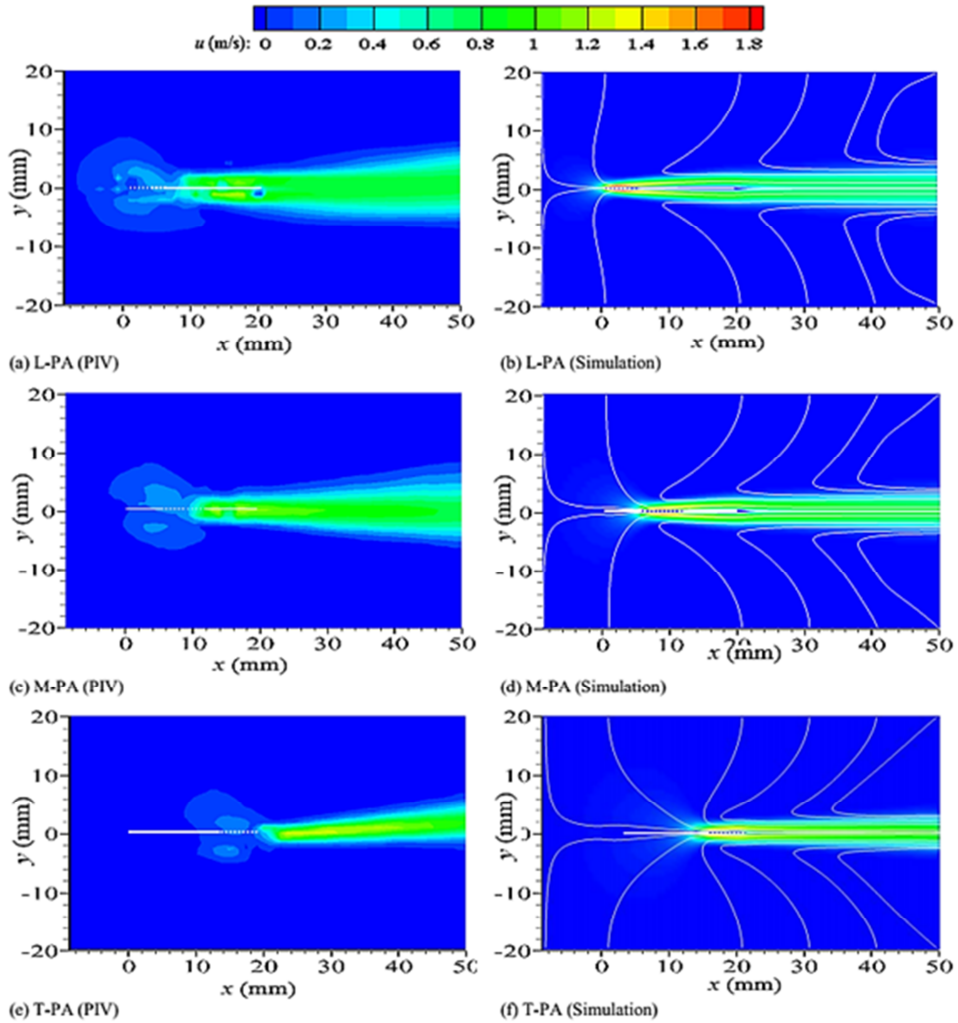

Fig.6: Velocity contour maps around winglets: (a), (c), and (e) PIV measurements, and (b), (d), and (f) computational results. The applied voltage is ±4 kV. The dotted line indicates the location of covered electrode.

Velocity contour maps have been represented in figure 6 in which white line indicated the location of winglet PA with dotted line as a location of covered electrode. Both experiment and simulation indicate wider jet width like L>M>T PA. This is because the electrode arrangement on mini wing plate. Behavior of near electrode flow has been investigated easily from simulation. M and T PA have same shape of electrode except location over plate, gave same trend of induced flow but M PA provides lower induced flow at trailing end than T PA.

On the other hand, L PA gives maximum induced velocity than M and T PA but at downstream unified velocity is lower than other two types. Trend of flow reduction over embedded electrode has been shown in figure 7 based on peak velocity at each x locations (from simulation). The reason is the end gap between the embedded electrode and trailing end of wing. Higher the end gap increase frictional loss which reduces downstream flow. In all three types of PA, maximum induced flow has been found at 0.44mm above (both side) of actuator surface. Along this y location, percentage of flow reduction has been calculated from velocity changes along x axis and presented at table 1.

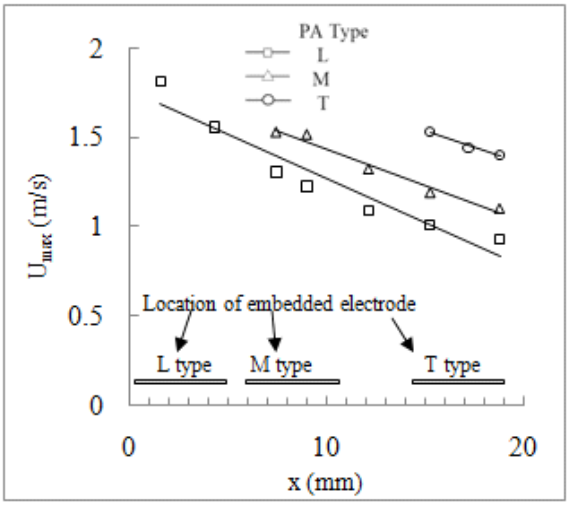

Fig.7: Trend of flow reduction over wing

Table 1. Calculation of flow reduction over wing

Type of Actuator	Max. induced flow velocity (m/s)	Velocity at the end of wing plate (m/s)	% of flow reduction
L type PA	1.81	0.35	80.51%
M type PA	1.53	0.599	60.74%
T type PA	1.53	1.2	21.597%

It is found that increase in distance between embedded electrodes and tailing end of wing, decrease the induced velocity at the end of tailing edge as a result lower unified velocity at downstream

4. CONCLUSION

In this paper, experimental analysis and numerical modelling have been performed to evaluate special design plasma actuator. Effect of end gap and shape of exposed electrodes have been investigated. From the above mentioned analyses it is clear that velocity reduction over wing is less for that type of PA which has smallest gap between embedded electrode and trailing edge. Higher the gap higher the reduction at downstream. As a result lowest velocity reduction has been found in T PA and higher unified velocity at downstream than other two types of PA. Shape of exposed electrode has a great role on near electrode flow. Only L PA has wire type exposed electrode, from simulation it is found that this type of PA provides maximum induced flow over embedded electrode than that of M PA and T PA as shape of exposed electrode is different. Both M PA and T PA have same shape of exposed electrode but only difference is in electrode position on mini-plate wing and both of these PA gave same magnitude of induced flow velocity. So, it is clear that shape of exposed electrode has a great influence on induced flow.

5. ACKNOWLEDGEMENTS

This research work has been carried out as part of PhD research at Tokyo Metropolitan University, Japan under the supervision of Prof. Hiroshi Mizunuma.

REFERENCES

[1] Post, M. L., and Corke, T. C., 2004, “Separation Control on a High Angle of Attack Airfoil Using Plasma Actuators,” AIAA Journal, Vol. 42, No. 11, pp. 2177–2184.
[2] Benard, N., Braud, P., and Jolibois, J.2008,“Airflow Reattachment Along a NACA 0015 Airfoil by Surface SDBD Actuator-Time Resolved PIV Investigation,” AIAA Paper 2008-4202.

[3] Post, M. L., and Corke, T. C.,2006, "Separation Control Using Plasma Actuators—Dynamic Stall Vortex Control on an Oscillating Airfoil," AIAA Journal, Vol. 44, No. 12, pp. 3125–3135.
[4] Do, H., Kim, W., Mungal, M. O., and Cappelli, M. A., 2007, "Bluff Body Flow Separation Control Using Surface Dielectric Barrier Discharges," AIAA Paper 2007-939.
[5] Thomas, F. O., Kozlov, A., and Corke, T. C., 2008, "Plasma Actuators for Cylinder Flow Control and Noise Reduction", AIAA Journal, Vol. 46, No. 8, pp. 1921–1931
[6] Schatzman, D., and Thomas, F. O., 2008, "Turbulent Boundary Layer Separation Control Using Plasma Actuators,"AIAA Paper 2008-4199
[7] Baughn, J.W., Porter, C., Peterson, B.L., McLaughlin, T.E., Enloe, C.L., Font, G. I., and Baird, C. 2006,"Momentum Transfer for an Aerodynamic Plasma Actuator with an Imposed Boundary Layer," AIAA Paper 2006-168.
[8] Corke, T. C., He, C., and Patel, M., 2004, "Plasma Flaps and Slats: An Application of Weakly-Ionized Plasma Actuators," AIAA Paper 2004-2127.
[9] Huang, J., Corke, T. C., and Thomas, F. O., 2006, "Plasma Actuators for Separation Control of Low-Pressure Turbine Blades," AIAA Journal, Vol. 44, No. 1 pp. 51–57.
[10] Van Ness, D. K., II, Corke, T. C., and Morris, S. C., 2006, "Turbine Tip Clearance Flow Control Using Plasma Actuators," AIAA Paper 2006-0021.
[11] Langmuir I (1926) Proc Nat Acad Sci 14:627
[12] Seth Walker, Takehiko Segawa, Timothy Jukes, Hirohide Furutani, Norihiko Iki, Shinya Takekawa. 2012, "Active Control Of Flow Separation Over a NACA 0024 Airfoil By DBD Plasma Actuator And FBG Sensor", Journal of Fluid Science and Technology, Volume 7, Issue 1, pp. 39-52
[13] Y. B. Suzen, P.G. Huang, J.D. Jacob and D.E. Ashpis, "Numerical simulation of plasma based flow control applications", 35th Fluid Dynamics Conference and Exhibit, AIAA-4633
[14] M. Forte, J. Jolibois, F. Baudoin, E. Moreau, G. Touchard, M. Cazalens, "Optimization of a dielectric barrier discharge actuator by stationary and non-stationary measurements of the induced flow velocity: application to airflow control", Exp Fluids 43:917–928

AN INTEGRATED DUCTING SYSTEM DESIGN FOR LEAD ACID BATTERY FORMATION ROOM

Engr. Abdul Alim[1] and Engr. Nahid Niazi[2]
[1]Electro Battery Co. Ltd. and [2]Standard Garments Ltd.; Bangladesh
E-mail: nniloy_15@yahoo.com

ABSTRACT: Formation is one of the key processes of lead acid battery production system. It is usually a series of soaking, charging, discharging of battery plates to raise the durability of battery. In this stage of battery production, a huge amount of O_2 & H_2 evolved, a huge amount of heat generated as a byproduct of acid dilation & plate formation reactions, simultaneously humidity of formation room falls and air gets contaminated with massive amount of acid aerosol & SLS (sodium lauryl sulfate) dust. As a result, air of formation room becomes explosive, worker irritating, corrosive and non-conforming to environmental regulatory bodies. This paper is actually a case study to solve this kind of problems occurring in formation room or so. Here four alternative solutions have been designed & discussed with their merits and shortcomings. In the end, the best alternative solution, the integrated ducting system, has been highlighted how it would integrally work for ventilation, dust collection, equipment corrosion resistance and air treatment.

Keywords: Lead acid battery, Formation room, Ducting design, Air treatment.

1. INTRODUCTION

Formation is the most critical process of lead acid battery production because of its exposures to environment. To mitigate the exposures, it needs to design the formation room as well as its ducting system. In this case study, we have studied a formation room of most common size; we have studied about the volume capacity, gas generation form the formation vats etc. As per the requirements of formation room (ventilation, dust collection, equipment corrosion resistance and air treatment) we have generated four models of ducting system: Direct ventilation system, Ducting with exhaust fan system, Ducting with exhaust fan & filter system, Integrated ducting system. We have gone through the models one by one & found out their merits & demerits. Direct ventilation system is the simplest system but it is dependent on the weather of environment as well as it does not provide any air treatment. Ducting with exhaust fan system ensures proper ventilation but here the exhaust fans & ducts are corroded gradually and this system does not do any air treatment. Ducting with exhaust fan & filter system is good for dust collecting and partially good for air treatment but this system's mas flow (ventilation) rate decreases very soon due to the dust particles being embedded with the filter. The integrated ducting system is the best in any consideration of ventilation, dust collection, equipment corrosion resistance and air treatment. The integrated ducting system is consisting of main four parts: dust particle collector, clarifier tank, AGM separator & blower. Blower ensures proper air flow & ventilation; the dust particle collector primarily collects the dust; the AGM separator finely collects the dust particle & primarily absorbs acid aerosol; at last the clarifier solution of clarifier tank finely mitigates the acid aerosol.

NOMENCLATURE

Q	Fluid discharge rate	L	Length of pipe
$\bar{u}$	Fluid flow rate, average velocity	μ	Fluid velocity
A	Duct's cross-sectional area	ρ	Fluid density
r	Radius of pipe		

2. MATHEMATICAL EQUATIONS

The equations are drawn from reference [1] (equations' no. 8.13d, 8.13e, 8.13c, 6.2):

Average velocity of fluid through a pipe, $\bar{u} = Q/A = Q/\pi r^2$ … … … (1)

Point of maximum velocity, $u_{max} = 2\bar{u}$ … … … (2)

Pressure loss in a pipe due to frictional effect, $\Delta P = 128\mu LQ/\pi d^4$ … … … (3)

Pressure loss in a duct due to bend, $\Delta P = \rho\bar{u}^2 \ln\frac{r_2}{r_1}$ … … … (4)

3. DESIGN & DISCUSSION

3.1. A TYPICAL FORMATION ROOM

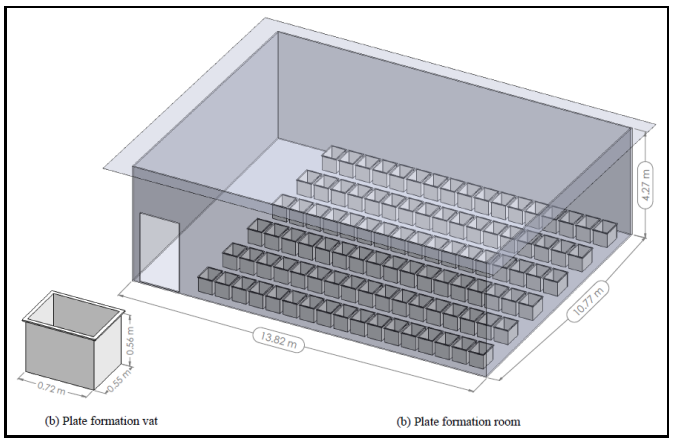

Fig. 1: Plate formation space, Lead acid battery

Discharge requirement:

Formation room space = 635 m^3

Gas formation per vat (approximately) = 0.02 m^3/min

Gas formation from 102 vats = 2.4 m^3/min

If we assume that the room needs to be totally evacuated within a minute, so,

Air flow rate (i.e. required discharge) = 637.4 m^3/min

3.2. MODEL NO. 1 (DIRECT VENTILATION)

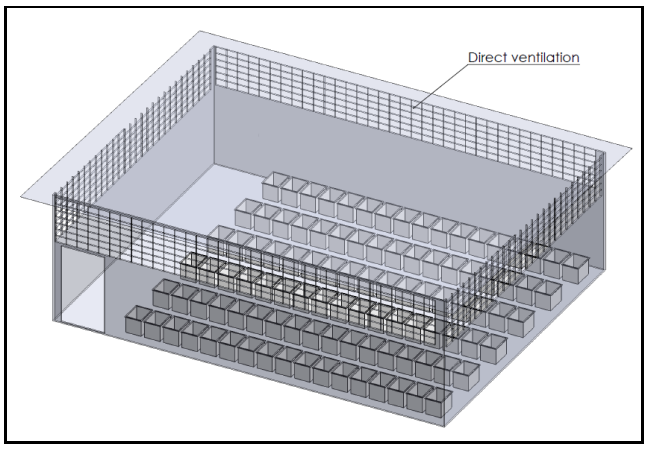

Fig. 2: Direct ventilation system

The advantages of this model no. 1 are: it provides a free & open way of air movement; it is of very cheap or no installation cost; it provides no chance of corrosion of duct or exhaust fans. The shortcomings of this model are: it neither includes dust collection system nor air treatment system; moreover it may cause hassle while it rains or storms or so. This system is mostly depended on air flow & the weather of the environment.

3.3. MODEL NO. 2 (DUCTING WITH EXHAUST FAN)

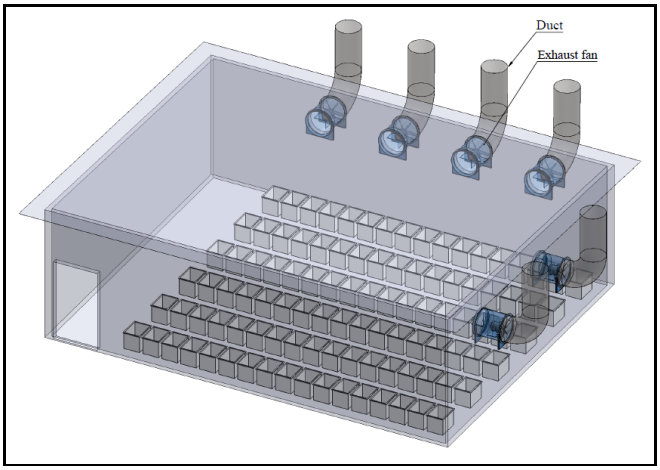

Fig. 3(a): Ducting with exhaust fan system

The advantages of this model no. 2 are: it provides proper ventilation of the room; exhaust fan requirements can be calculated for certain so this system can be tuned as per necessity. The shortcomings of this model are: this system is sharply hampered by corrosion of fans & ducts; it neither includes dust collection system nor air treatment system.

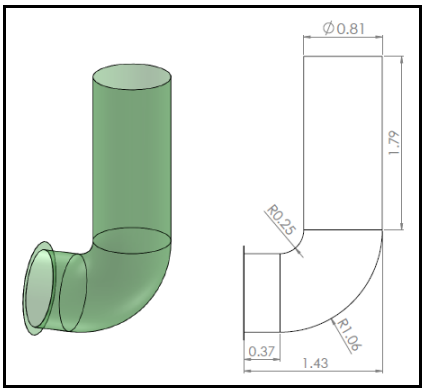

Fig. 3(b): Duct size

Our required discharge = 637.4 m^3/min

If we use exhaust fan of 3800 CFM (Q=107.6 m^3/min), we will require 6 exhaust fans.

Total pressure loss = frictional loss + loss due to bend (using eq. (1), (2), (3), (4))

$= 128\mu LQ/\pi d^4 + \rho \bar{u}^2 \ln \frac{r_2}{r_1}$

$= 128*(18.6*10^{-6})*(0.37+1.79)*1.92 /(\pi*0.81^4) +1.23 * 3.73^2 * \ln \frac{1.06}{0.25}$

$= 1.42+24.7 = 26.12$ N.m^{-2}

3.4. MODEL NO. 3 (DUCTING WITH EXHAUST FAN & FILTER)

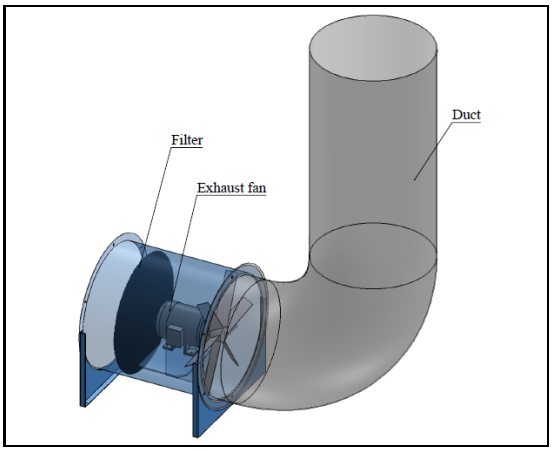

Fig. 4: Ducting with exhaust fan & filter system

The advantages of this model no. 3 are: it ensures dust collection; it partially clarifies the exhausted air; it partially ensures the resistance of corrosion on fan & duct. The shortcomings of this model are: its filter resists proper ventilation of the room; filter embedded with the dusts significantly hampers the air flow; filter needs to be replaced frequently; ducting requirements cannot be calculated properly due to the uncertain mass flow rate of the filter.

3.5. MODEL NO. 4 (INTEGRATED DUCTING SYSTEM)

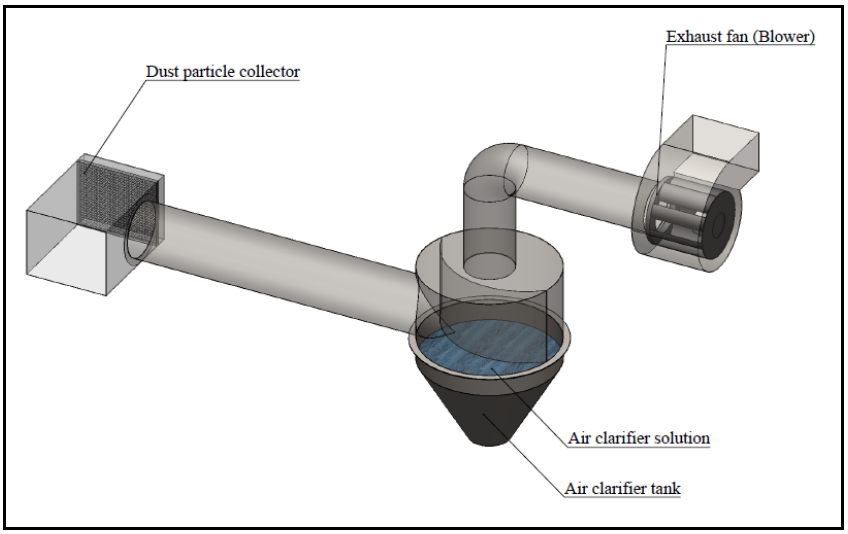

Fig. 5(a): Integrated ducting system

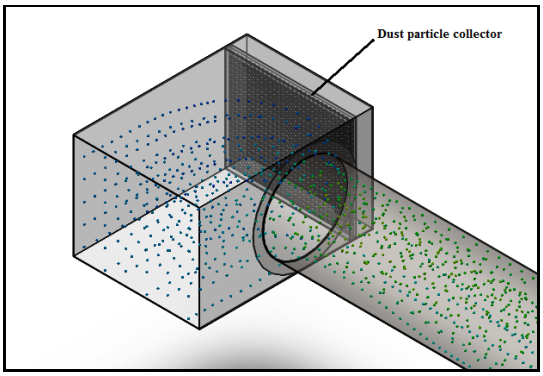

Fig. 5(b): Dust particle collector

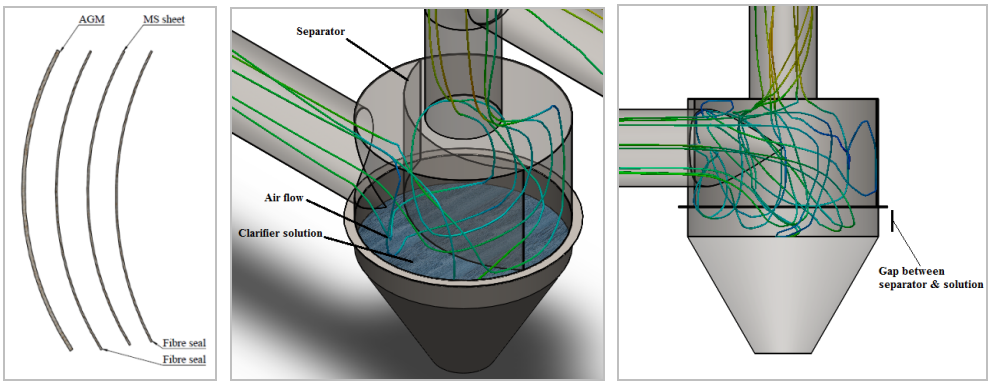

Fig. 5(c): structure of separator; (d) air flow through clarifier; (e) side view of air clarifier

Figure 5(a) illustrates the basic design of the integrated ducting system. As illustrated in the fig. 5(b), the dust particles are primarily shucked & collected by the dust particle collector. Only the fine particles pass the way of pipe & get collected by next filter & clarifier. Fig. 5(c), the separator is composed of three components: the MS sheet is sealed with fiber & glue for protection from acid aerosol; on the front side of this sheet an AGM (Absorbent Glass Mate) paper is attached which finely collects the fine dust particles & primarily mitigates the acid aerosol. Finally the neutralizing solution (caustic soda, hydrated lime or any other neutralizing solution) of clarifier tank mitigates the acid aerosol. For periodic replacement of expired solution, the clarifier tank includes two channels as inlet & outlet of solution. The paths of air flow are shown by the fig. 5(d) & fig. 5(e). The centrifugal blower of forward carve blades, the driver of ventilation or air flow, stands at the last portion of the model. The chemical equation of neutralization of sulfuric acid aerosol is given below.

$2NaOH\ (l) + H_2SO_4\ (g) = Na_2SO_4\ (l) + 2H_2O\ (l)$

Or, $Ca(OH)_2\ (l) + H_2SO_4\ (g) = CaSO_4.2H_2O\ (\downarrow)$

The advantages of this model no. 4 are: it ensures uninterrupted ventilation unlike the model no. 3; it ensures complete dust collection in two stages; it ensures clarification of air; it ensures resistance of corrosion of fan & duct. This integrated ducting system satisfies all the requirements we have for a lead acid battery formation room. The main shortcoming of this model is its more complex design than the others, as well as it needs periodic replacement of AGM paper and periodic replacement of neutralizing solution.

4. CONCLUSION

Here the four models have been designed & discussed under the consideration of a formation room of lead acid battery manufacture. It is shown by this study that how the model 4 (integrated ducting system) is superior to other three models. It is undoubted that this integrated model will be the best for any other production system.

5. REFERENCES

[1]. Philip J. Pritchard, "Fox and McDonald's INTRODUCTION TO FLUID MECHANICS", ISBN-13 9780470547557, 8th Edition.
[2]. John F. Douglas, Janusz M. Gasiorek, John A. Swaffield, Lynne B. Jack, "FLUID MECHANICS", ISBN-13: 978-0-13-129293-2, 5th edition
[3]. Detchko Pavlov, "Lead-Acid Batteries: Science and Technology", ISBN: 978-0-444-52882-7

Nanofluid Flow over a Semi-infinite Plate in a Rotating System with Radiation and Viscous Dissipation

[*]Tanvir Ahmed, M. M. Mukitul Hasan and [**]Md. Mahmud Alam
Mathematics Discipline, Khulna University, Khulna-9208, Bangladesh
Department of Mathematics, Khulna Public College, Khulna-9000, Bangladesh
Email: [**]alam_mahmud2000@yahoo.com, [*]tanvir1989bd@gmail.com

ABSTRACT*:* The unsteady MHD heat and mass transfer nanofluid flow past a semi-infinite horizontal plate with viscous dissipation in a rotating system have been investigated. To obtain dimensionless non-similar coupled nonlinear momentum, energy and concentration equations, usual non-dimensional variables have been used. The explicit finite difference method has been used to solve the dimensionless equations. The obtained numerical results have been presented graphically and discussed in details.

Keywords: MHD; Nanofluid; Rotating system; Explicit finite difference method.

1. INTRODUCTION

Nanofluid is an engineered colloidal suspension of nanoparticle in base fluid. The potentiality of the nanofluids for the heat and mass transfer depends on the characteristics of the base fluids and nanoparticles. Many researchers have shown in their experiments that nanofluids are better than the conventional fluids. There are some features of nanaofluids. These features are increased thermal conductivity at low nanoparticle concentrations, strong temperature dependent. These features of nanofluids make them next generation heat and mass transfer fluids. In recent studies, we see the application of nanofluids is growing very rapidly. Nanofluids are used in many industrial, scientific and engineering problems. Nanofluids are also used in microelectronics, fuel cells, engine cooling, domestic refrigeration, pharmaceutical processes, hybrid-powered engines, nuclear reactor coolant, in grinding, machining, in space technology, defense and ships, biomedical technology, ceramic industries, plastic industries, etc. The word “nanofluid” was first introduced in fluid flow by Choi [1] to develop the heat transfer fluid significantly superior conductivities. The laminar boundary layer flow of nanofluid past a stretching sheet has been investigated by Khan and Pop [2]. The MHD flow in the presence of radiation has been studied Raptis and Massalas [3]. The boundary layer flow of a nanofluid past a stretching sheet with a convective boundary condition in presence of magnetic field and thermal radiation has been analyzed by Gabadeyan et al. [4]. It has been studied that the abnormal increase of thermal conductivity of nanofluids by Buongiorno [5]. The unsteady free convection and mass transfer flow of a viscous, incompressible and electrically conducting fluid past a moving finite vertical porous plate with thermal diffusion has been investigated by Sattar and Alam [6]. The problem of three dimensional fluid flows due to stretching flat plate has been studied by Wang [7]. The radiation effects on MHD free convective boundary layer flow of nanofluids over a nonlinear stretching sheet has been analyzed by Poornima and Readdy [8].

Hence our aim is to study nanofluid flow over a semi-infinite plate in a rotating system with radiation and viscous dissipation. The nondimensional governing boundary layer equations are solved by explicit finite difference method. Numerical results have been presented in graphically.

3. MATHEMATICAL MODEL OF FLOW

Consider an MHD free convection and mass transfer flow of an electrically conducting viscous fluid through a plate $y = 0$ in a rotating system. The positive x coordinate is measured along the plate and y is the coordinate measured normal to the plate and z is the coordinate normal to the plate. The flow is assumed to be in the x direction.

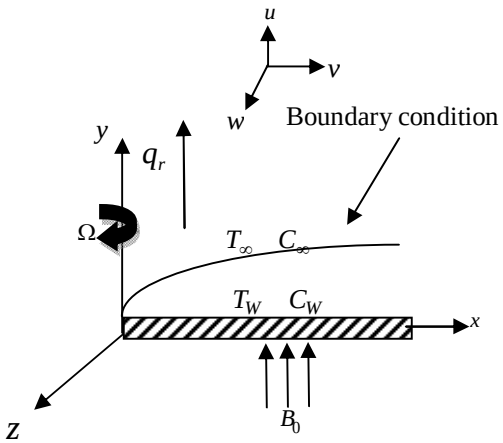

Fig.1 Physical configuration and coordinate system.

The physical configuration and coordinate system are shown in Fig1. Initially the fluid as well as the plate is at rest, after the whole system is allowed to rotate with a constant angular velocity Ω about y-axis. The temperature and the species concentration at the plate are constantly raised from T_w and C_w to T_∞ and C_∞ respectively, which are there after maintained constant, where T_∞ and C_∞ are the temperature and species concentration of the uniform flow respectively. A uniform magnetic field B_0 is imposed to the flow region. Let us consider that $\mathbf{B} = (0, B_0, 0)$ and the magnetic lines of force are fixed relative to the fluid. The radiative heat flux is q_r . The basic governing equations are as follows;
The continuity equation;

$$\frac{\partial u}{\partial x} + \frac{\partial v}{\partial y} = 0 \tag{1}$$

The momentum equation in x-direction;

$$\frac{\partial u}{\partial t} + u\frac{\partial u}{\partial x} + v\frac{\partial u}{\partial y} = \upsilon\left(\frac{\partial^2 u}{\partial y^2}\right) + 2w\Omega - \frac{\sigma B^2{}_0 u}{\rho} \tag{2}$$

The momentum equation in z-direction;

$$\frac{\partial w}{\partial t} + u\frac{\partial w}{\partial x} + v\frac{\partial w}{\partial y} = \upsilon\left(\frac{\partial^2 w}{\partial y^2}\right) - 2u\Omega - \frac{\sigma B^2{}_0 w}{\rho} \tag{3}$$

The energy equation;

$$\frac{\partial T}{\partial t} + u\frac{\partial T}{\partial x} + v\frac{\partial T}{\partial y} = \alpha\left(\frac{\partial^2 T}{\partial y^2}\right) - \frac{\alpha}{k}\left(\frac{\partial q_r}{\partial y}\right) + \frac{\upsilon}{c_p}\left\{\left(\frac{\partial u}{\partial y}\right)^2 + \left(\frac{\partial w}{\partial y}\right)^2\right\} + \tau\left\{\mathrm{D_B}\left(\frac{\partial \mathrm{C}}{\partial \mathrm{y}}\cdot\frac{\partial \mathrm{T}}{\partial \mathrm{y}}\right) + \frac{\mathrm{D_T}}{\mathrm{T}_\infty}\left(\frac{\partial \mathrm{T}}{\partial \mathrm{y}}\right)^2\right\} \tag{4}$$

The concentration equation;

$$\frac{\partial C}{\partial t} + u\frac{\partial \mathrm{C}}{\partial x} + v\frac{\partial C}{\partial y} = D_B\left(\frac{\partial^2 C}{\partial y^2}\right) + \frac{\mathrm{D_T}}{\mathrm{T}_\infty}\left(\frac{\partial^2 T}{\partial y^2}\right) \tag{5}$$

The initial and boundary conditions are;

$$u = U_0, \quad v = 0, w = 0, \quad T = T_w, \quad \mathrm{C} = \mathrm{C}_w, \qquad \text{at y} = 0 \tag{6}$$
$$u = 0, v = 0, w = 0, \quad T \to T_\infty, \quad \mathrm{C} \to \mathrm{C}_\infty, \quad \text{as y} \to \infty$$

where ρ is the density of the fluid , υ is the kinematic viscosity , D_B is the Brownian diffusion coefficient, D_T is the thermophoresis diffusion coefficient, α is the thermal diffusivity , κ is the thermal conductivity , U is the uniform velocity, σ is the electric conductivity of the fluid.

The Rosseland approximation is expressed for radiative heat flux and leads to the form as,

$$q_r = -\frac{4\sigma^*}{3\kappa^*}\frac{\partial T^4}{\partial y} \tag{7}$$

Where κ^* is the mean absorption coefficient, σ^* is the Stefan-Boltzmann constant. The temperature difference with in the flow is sufficiently small. So that T^4 may be expressed as a linear function of the temperature, then the Taylor's series for T^4 about T_∞ after neglecting higher order terms,

$$T^4 \cong 4T\,T_\infty^4 - 3T_\infty^3 \tag{8}$$

The dimensionless variables that are using in the equations (1)- (5)are as follows ;

$$X = \frac{xU_0}{\upsilon}, Y = \frac{yU_0}{\upsilon}, U = \frac{u}{U_0}, V = \frac{v}{U_0}, W = \frac{w}{U_0}, \tau = \frac{tU_0^2}{\upsilon}, \overline{T} = \frac{T - T_\infty}{T_w - T_\infty}, \overline{C} = \frac{C - C_\infty}{C_w - C_\infty}$$

Using these above dimensionless variables, the following dimensionless equations have been obtained as;

$$\frac{\partial U}{\partial X} + \frac{\partial V}{\partial Y} = 0 \tag{9}$$

$$\frac{\partial U}{\partial \tau} + U\frac{\partial U}{\partial X} + V\frac{\partial U}{\partial Y} = \frac{\partial^2 U}{\partial Y^2} + 2R'W - MU \tag{10}$$

$$\frac{\partial W}{\partial \tau} + U\frac{\partial W}{\partial X} + V\frac{\partial W}{\partial Y} = \frac{\partial^2 W}{\partial Y^2} - 2R'U - MW \tag{11}$$

$$\frac{\partial \overline{T}}{\partial \tau} + U\frac{\partial \overline{T}}{\partial X} + V\frac{\partial \overline{T}}{\partial Y} = \left(\frac{1+R}{P_r}\right)\frac{\partial^2 \overline{T}}{\partial Y^2} + E_c\left\{\left(\frac{\partial U}{\partial Y}\right)^2 + \left(\frac{\partial W}{\partial Y}\right)^2\right\} + N_b\left(\frac{\partial \overline{T}}{\partial Y}\cdot\frac{\partial \overline{C}}{\partial Y}\right) + N_t\left(\frac{\partial \overline{T}}{\partial Y}\right)^2 \tag{12}$$

$$\frac{\partial \overline{C}}{\partial \tau} + U\frac{\partial \overline{C}}{\partial X} + V\frac{\partial \overline{C}}{\partial Y} = \frac{1}{L_e}\left[\frac{\partial^2 \overline{C}}{\partial Y^2} + \left(\frac{N_t}{N_b}\right)\frac{\partial^2 \overline{T}}{\partial Y^2}\right] \tag{13}$$

The corresponding non-dimensional boundary conditions are as;

$$\begin{aligned} &U = 1,\quad V = 0,\quad W = 0,\quad \overline{T} = 1,\quad \overline{C} = 1, \text{ at } \quad Y = 0 \\ &U = 0,\quad V = 0,\quad W = 0,\quad \overline{T} \to 0,\quad \overline{C} \to 0, \text{ as } \quad Y \to \infty \end{aligned} \tag{14}$$

The non-dimensional quantities are; $M = \frac{\sigma B_0^2 \upsilon}{\rho U_0^2}$ (Magnetic parameter), $R = \frac{16\sigma^* T_\infty^3}{3kk^*}$ (Radiation parameter), $P_r = \frac{\upsilon}{\alpha}$ (Prandtl number), $L_e = \frac{\upsilon}{D_B}$ (Lewis number), $N_b = \frac{\tau D_B (C_w - C_\infty)}{\upsilon}$ (Brownian parameter), $N_t = \frac{D_T}{T_\infty}\frac{\tau}{\upsilon}(T_w - T_\infty)$ (Thermophoresis parameter), $R' = \frac{\Omega\upsilon}{U_0^2}$ (Rotational Parameter). $E_c = \frac{U_0^2}{c_p(T_w - T_\infty)}$ (Eckert number).

4. NUMERICAL SOLUTIONS

To solve the non-dimensional system by the explicit finite difference method, it is required a set of finite difference equation. To obtain the difference equations the region of the flow is divided into a grid or mesh of lines parallel to X and Y axes where X -axis is taken along the plate and Y -axis is normal to the plate.

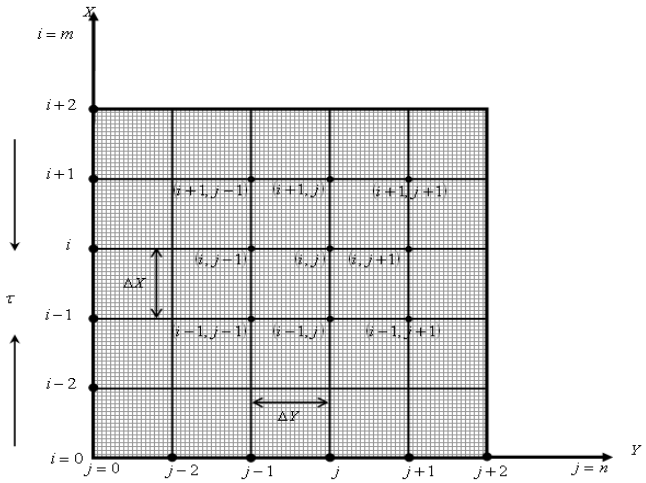

Fig. 2. Explicit finite difference system grid.

Here the plate of height $X_{\max}(=100)$ is measured i.e. X varies from 0 to 100 and assumed $Y_{\max}(=25)$ as corresponding to $Y\to\infty$ i.e. Y varies from 0 to 25. There are $m(=200)$ and $n(=200)$ grid spacing in the X and Y directions respectively as shown Fig. 2. ΔX , ΔY are constant mesh size along X and Y directions respectively and taken as follows, $\Delta X = 1.00(0 \le X \le 100)$ and $\Delta Y = 0.25(0 \le Y \le 25)$ with the smaller time-step, $\Delta\tau = 0.005$. Let $U', W', \overline{T}'$ and $\overline{C}'$ denote the values of $U, W, \overline{T}$ and $\overline{C}$ at the end of a time-step respectively. Using the explicit finite difference approximation, the system of partial differential equations (9)-(13) and the boundary conditions (14), an appropriate set of finite difference equations have been obtained as;

$$\frac{U'_{i,j}-U'_{i-1,j}}{\Delta X}+\frac{V'_{i,j}-V'_{i,j-1}}{\Delta Y}=0 \tag{15}$$

$$\frac{U'_{i,j}-U_{i,j}}{\Delta\tau}+U_{i,j}\frac{U_{i,j}-U_{i-1,j}}{\Delta X}+V_{i,j}\frac{U_{i,j+1}-U_{i,j}}{\Delta Y}=\frac{U_{i,j+1}-2U_{i,j}+U_{i,j-1}}{(\Delta Y)^2}+2R'W_{i,j}-MU_{i,j} \tag{16}$$

$$\frac{W'_{i,j}-W_{i,j}}{\Delta\tau}+U_{i,j}\frac{W_{i,j}-W_{i-1,j}}{\Delta X}+V_{i,j}\frac{W_{i,j+1}-W_{i,j}}{\Delta Y}=\frac{W_{i,j+1}-2W_{i,j}+W_{i,j-1}}{(\Delta Y)^2}-2R'U_{i,j}-MW_{i,j} \tag{17}$$

$$\frac{\overline{T}'_{i,j}-\overline{T}_{i,j}}{\Delta\tau}+U_{i,j}\frac{\overline{T}_{i,j}-\overline{T}_{i-1,j}}{\Delta X}+V_{i,j}\frac{\overline{T}_{i,j+1}-\overline{T}_{i,j}}{\Delta Y}=\left(\frac{1+R}{P_r}\right)\left(\frac{\overline{T}_{i,j+1}-2\overline{T}_{i,j}+\overline{T}_{i,j-1}}{(\Delta Y)^2}\right)$$
$$+E_c\left\{\left(\frac{U_{i,j+1}-U_{i,j}}{\Delta Y}\right)^2+\left(\frac{W_{i,j+1}-W_{i,j}}{\Delta Y}\right)^2\right\}+N_b\left(\frac{\overline{T}_{i,j+1}-\overline{T}_{i,j}}{\Delta Y}\cdot\frac{\overline{C}_{i,j+1}-\overline{C}_{i,j}}{\Delta Y}\right)+N_t\left(\frac{\overline{T}_{i,j+1}-\overline{T}_{i,j}}{\Delta Y}\right)^2 \tag{18}$$

$$\frac{\overline{C}'_{i,j}-\overline{C}_{i,j}}{\Delta\tau}+U_{i,j}\frac{\overline{C}_{i,j}-\overline{C}_{i-1,j}}{\Delta X}+V_{i,j}\frac{\overline{C}_{i,j+1}-\overline{C}_{i,j}}{\Delta Y}=$$
$$\frac{1}{L_e}\left[\left(\frac{\overline{C}_{i,j+1}-2\overline{C}_{i,j}+\overline{C}_{i,j-1}}{(\Delta Y)^2}\right)+\left(\frac{N_t}{N_b}\right)\left(\frac{\overline{T}_{i,j+1}-2\overline{T}_{i,j}+\overline{T}_{i.j-1}}{(\Delta Y)^2}\right)\right] \tag{19}$$

With initial and boundary conditions;

$$U^n_{i,0}=1,\ V^n_{i,0}=0,\ W^n_{i,0}=0,\ \overline{T}^n_{i,0}=1,\ \overline{C}^n_{i,0}=1 \tag{20}$$
$$U^n_{i,L}=0,\ V^n_{i,L}=0,\ W^n_{i,L}=0,\ \overline{T}^n_{i,L}=0,\ \overline{C}^n_{i,L}=0,\quad \text{where}\ L\to\infty$$

Here the subscripts i and j designate the grid points with X and Y coordinates respectively and the subscript n represents a value of time, $\tau = n\Delta\tau$ where $n = 0,1,2,3,\ldots.\ \ldots.\ \ldots.$.

5. RESULTS AND DISCUSSION

In order to investigate the physical significance of the problem, the numerical values of primary velocity, secondary velocity, temperature and concentration within the boundary layer have been computed for different values of various parameters. To obtain the steady-state solutions, the calculation has been carried out up to non-dimensional time $\tau = 5$ to 80. It is observed that the numerical values of U, W, $\overline{T}$ and $\overline{C}$ however, show little changes after $\tau = 50$. Hence at $\tau = 50$ the solutions of all variables are steady-state solutions. The primary and secondary velocity distributions are displayed in Fig. 3 for different values of Magnetic parameter. These results show that the primary velocity increases with the increase of Magnetic parameter while the secondary velocity decreases. In Fig. 4., the primary and secondary velocity are illustrated for various values of Rotational parameter. It is noted that the primary velocity decreases with the increase of Rotational parameter while the secondary velocity also increases.

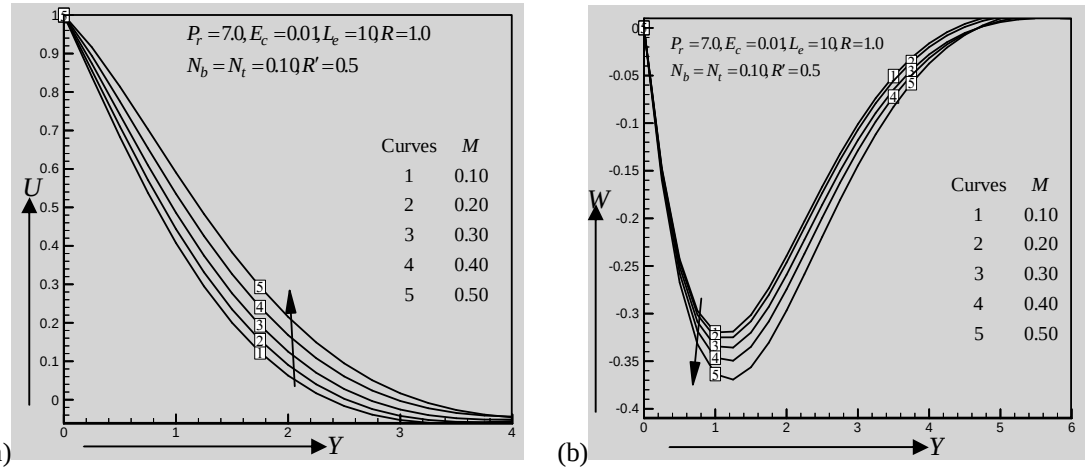

Fig.3 (a) Primary velocity profile and (b) secondary velocity profile for different values of magnetic parameter.

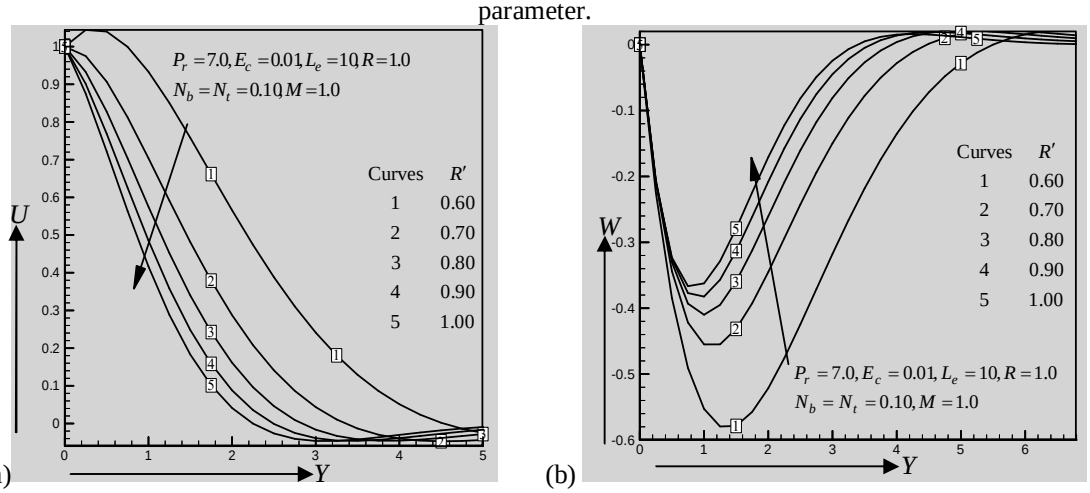

Fig.4 (a) Primary velocity profile and (b) secondary velocity profile for different values of Rotational parameter.

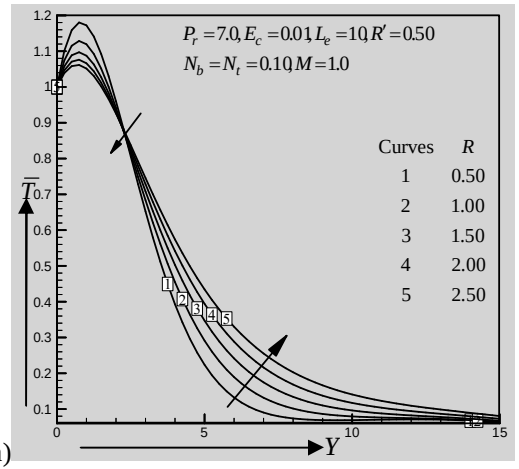

(a)

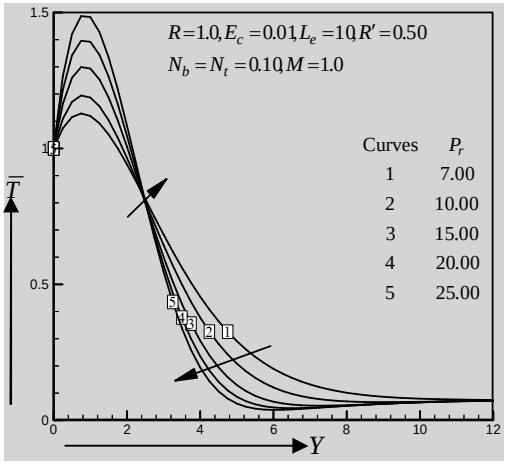

(b)

Fig.5 (a) Temperature profile for different values of Radiation parameter and (b) Temperature profile for different values of Prandtl number.

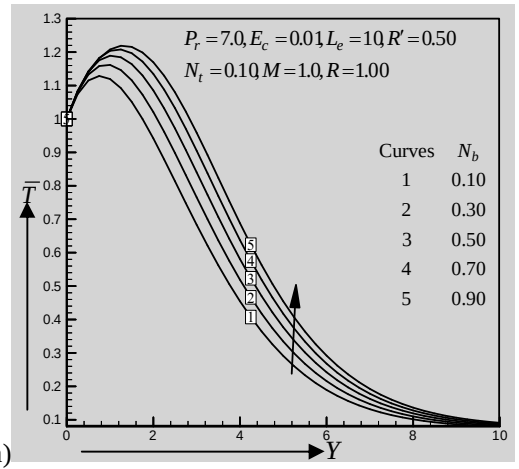

(a)

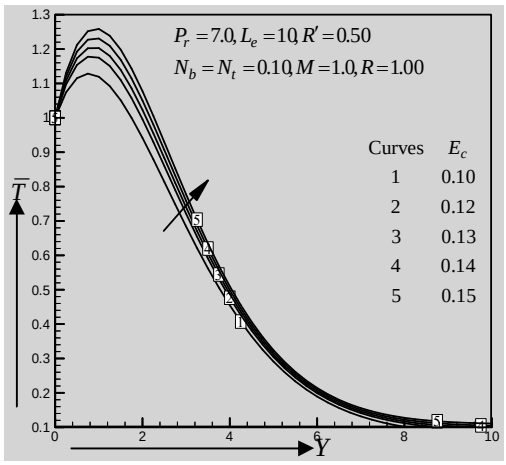

(b)

Fig.6 (a) Temperature profile for different values of Brownian motion parameter and (b) Temperature profile for different values of Eckert number.

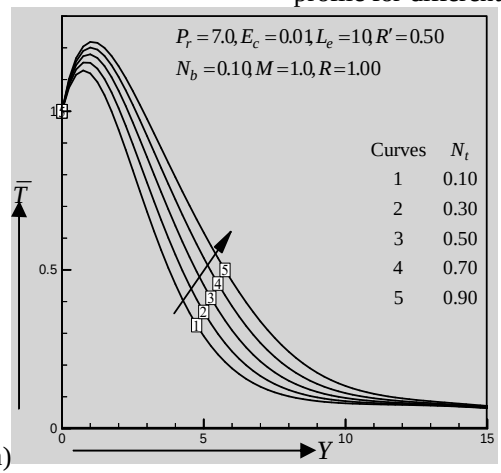

(a)

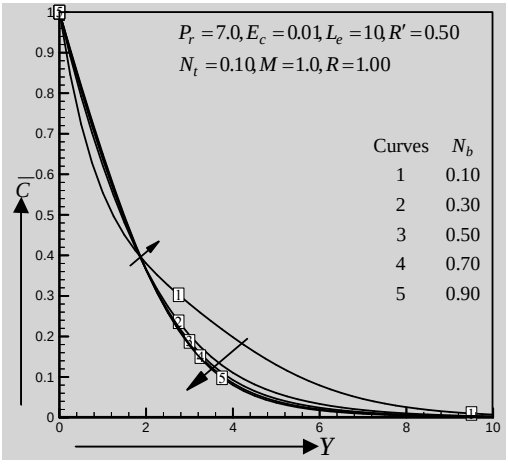

(b)

Fig.7 (a) Temperature profile for different values of Thermophoresis parameter and (b) Concentration profile for different values of the Brownian motion parameter.

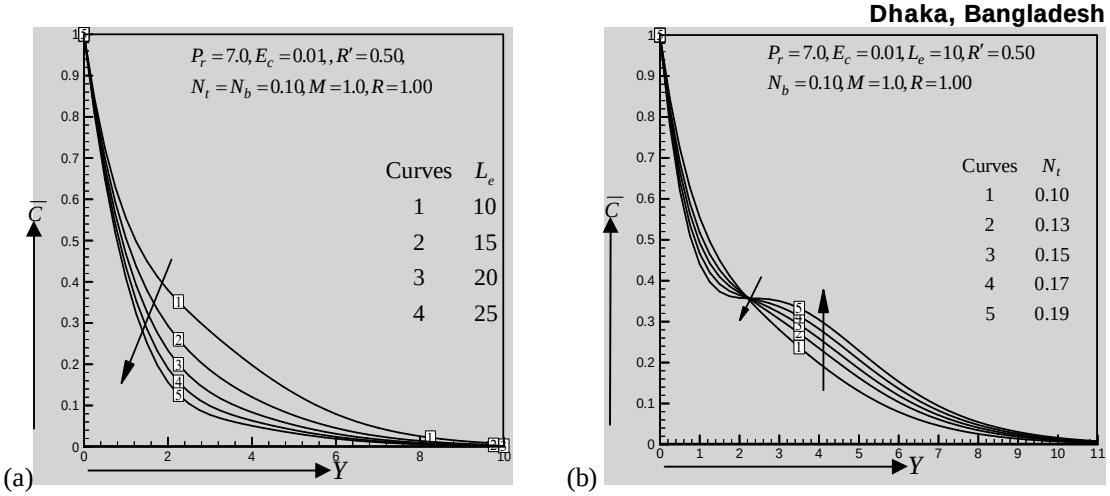

Fig.8 (a) Concentration profile for different values of Lewis number and (b) Concentration profile for different values of Thermophoresis parameter.

The Temperature distributions have been shown in Fig.5(a) to Fig.7(a) for different values of Radiation parameter, Prandtl number, Brownian motion parameter, Eckert number and Thermophoresis parameter respectively. The graphical presentation of the Fig.5(a) shows that near the plate the fluid temperature decreases but after $Y \geq 2.70 (\text{approx.})$ the fluid temperature increases for the increase of Radiation parameter. The graphical picture of the Fig.5(b) shows that the temperature distribution increases with the increase of Prandtl number at near the plate but after $Y \geq 2.70 (\text{approx.})$ it decreases with the increase of Prandtl number. The graphical picture 6(a) and 6(b) shows that the fluid temperature increases with the increase of Brownian motion parameter and Eckert number respectively. In Fig.7(a) shows that the fluid temperature increases with the increase of Thermophoresis parameter. The Concentration profile has been shown in the Fig.7(b) to Fig.8(b) for the different values of Brownian motion parameter, Lewis number and Thermophoresis parameter respectively. The graphical presentation of the Fig.7(b) shows that at near the plate fluid concentration increases but after $Y \geq 2.10 (\text{approx.})$ the fluid concentration decreases with the increase of Brownian motion parameter. The graphical structure of the Fig.8(a) indicates that the concentration distribution of the fluid decreases with the increase of Lewis number. Again the graphical configuration of the Fig.8(b) indicates that the concentration distribution of the fluid decreases near the plate with the increase of Thermophoresis parameter but after $Y \geq 2.50 (\text{approx.})$ the fluid concentration increases with the increase of Thermophoresis parameter.

6. CONCLUSIONS

The finite difference solution of nanofluid flow over a semi-infinite plate in a rotating system with radiation and viscous dissipation is investigated. The results are compared with the work of Khan and Pop [2].The accuracy of our results is qualitatively good in case of all parameters but not quantitively. Some important findings of this study are given below;

1. The primary velocity increases with the increase of Magnetic parameter and found reverse effect with the increase of Rotational parameter.
2. The secondary velocity decreases with the increase of Magnetic parameter and found reverse effect with the increase of Rotational parameter.
3. Temperature distributions increase with the increase of Brownian parameter. Eckert number and Thermophoresis parameter.
4. Concentration distributions decrease with the increase of Lewis number.

REFERENCES

1. S. U. S. Choi, "Enhancing thermal conductivity of fluids with nanoparticles",in:the proceedings of the 1995 ASME International Mechanical Engineering Congress and Exposition, San Fransisco, USA, ASME,FED231/MD66, pp.99-105,1995
2. W. A. Khan, I., Pop, "Boundary- layer flow of a nanofluid past a stretching sheet", International journal of Heat and Mass Transfer,Vol.53, pp.2477-2483,2010,
3. A. Raptis and C. V. Massalas, "Magnetohydrodynamic flow past a plate by the presence of radiation",Heat and Mass Transfer, Vol. 34, pp.107-109, 1998,
4. Gbadeyan J. A., Olanrewaju M. A.,and Olanrewaju P. O., " Boundary Layer of a Nanofluid Past a Stretching Sheet with a Convective Boundary Condition in the Presence of Magnetic Field and Thermal Radiation", Australian Journal of Basic and Applied Sciences,5(9), 1323-1334, 2011.
5. J. Buongiorno, " Convective transport in nanofluids", ASME Journal of Heat Transfer,Vol. 128,pp.240–250,2006
6. M. A. Sattar and M. M. Alam, "Thermal Diffusion as well as transportation effects on MHD free convection and mass transfer flow past an accelerated vertical porous plate", International journal of pure applied Mathematical science, 6:3, 1994.
7. C. Y. Wang, "The three-dimensional flow due to a stretching surface", Physics of Fluids, 27, pp.1915-1917,1984.
8. T. Poornima and N. Bhaskar Readdy, "Radiation effects on MHD free convective boundary layer flow of nanofluids over a nonlinear stretching sheet", Pelagia Research Library,4(2),pp.191-202,2013.

Authors

Author's Name: Tanvir Ahmed

Author's profile. Tanvir Ahmed obtained his M. Sc. (2013) in Applied Mathematics from Khulna University, Khulna, Bangladesh. He is doing research under the supervision of Professor Dr. Md. Mahmud Alam, Mathematics Discipline Khulna University, Khulna, Bangladesh. His major research interest is Computational Fluid Dynamics, Numerical Analysis & Mathematical Modeling. Mr. Tanvir has published two research papers in international Journal and Conferences. Also he has submitted a number of papers in international Journals and Conferences.

Author's Name: Mir Md. Mukitul Hasan

Author's profile. Mir Md. Mukitul Hasan obtained his M. Sc. (1998) degree in Mathematics from National University, Bangladesh. He is doing research under the supervision of Professor Dr. Md. Mahmud Alam, Mathematics Discipline Khulna University, Khulna, Bangladesh. His major research interest is MHD & Fluid Dynamics. Mr. Hasan has published a research paper in an international Journal and submitted a few number of papers in international Conferences. He is an Assistant Professor at the Department of Mathematics, Khulna public college, Khulna, Bangladesh. He has submitted the PhD application form for admission in Khulna University, Khulna, Bangladesh.

Author's Name: Professor Dr. Md. Mahmud Alam

Author's profile. Dr. Md. Mahmud Alam obtained his M. Sc. in Applied Mathematics from Chittagong University, Bangladesh and 1st PhD in Applied Mathematics from University of Dhaka, Dhaka, Bangladesh. He also achieved 2nd PhD and Postdoc in Mechanical Engineering from Okayama University, Okayama, Japan. His major research interest is MHD, Mathematical Fluid Dynamics & Numerical Simulation. Dr. Alam has published more than 120 papers in international Journals and joined many national and international Conferences. He supervised more than 50 students in M.Sc., M. Phil. and PhD level. He is a Professor at Mathematics Discipline, Khulna University, Khulna, Bangladesh.

JOULE HEATING EFFECT WITH DUFOUR AND SORET EFFECT ON UNSTEADY MHD FLOW OF VISCO-ELASTIC FLUID ON A VERTICAL POROUS PLATE

Dilruba Yasmin and Md. Mahmud Alam
Mathematics Discipline, Khulna University, Khulna-9208, Bangladesh
Email: alam_mahmud2000@yahoo.com

ABSTRACT: The effects of Joule heating on unsteady MHD flow of visco-elastic fluid on a vertical porous plate are investigated. The governing equations of the problem contain a system of partial differential equations. Non-dimensional variables have been used to obtain the dimensionless momentum, energy and concentration equations. The explicit finite difference method is used to solve dimensionless coupled nonlinear partial differential equations. The results of this investigation for Shear stress, Nusselt number and Sherwood number are discussed for the different values of the well known parameters, viscoelastic parameter (α), Joule Heating parameter (J_h) and Hartman number (M_{ha}) with different time steps. Finally, the obtained results are compared with the published paper in tabular form.

Keywords: MHD, Visco-elastic, Joule heating, Dufour Effect and Soret Effect.

1. INTRODUCTION

The study of two dimensional MHD boundary layer flow over different surface has many practical applications in different areas, for this reason this tropics is very important. The magneto-hydrodynamics (MHD) of an electrically conducting fluid has important bearings in geophysics, astrophysics, aeronautics, engineering applications and many other areas. Many researchers have studied Viscous fluid (Non-Newtonian and Newtonian). Viscous dissipation changes the temperature distributions by playing a role like an energy source, which leads affected heat transfer rates. The merit of the effect of viscous dissipation depends on whether the plate is being cooled or heated. From the viscous dissipation in MHD flows, the Joules dissipation also acts as a volumetric heat source. Heat transfer analysis over porous surface is of much practical interest due to its abundant applications. Heat-treated materials traveling between a feed roll and wind-up roll or materials manufactured by extrusion, glass-fiber and paper production, cooling of metallic sheets or electronic chips, crystal growing just to name a few. Attention has been made on the effect of transversely applied magnetic field on the flow of electrically conducting fluids with various properties associated with the interplay of magnetic fields and thermal perturbation in porous medium past vertical plate find usual applications in astrophysics, geophysical fluid dynamics and engineering. Many researchers have studied the effects of Joule heating and viscous dissipation. The effects of Joule heating and viscous dissipation are usually characterized by the Eckert number and magnetic parameter. Both have a very important part in geophysical flows and in nuclear engineering by Alim [1]. The problem of viscous dissipation, Joule heating and heat source/sink on non-Darcy MHD natural convection flow over an isoflux permeable sphere in a porous medium has been numerically analyzed by Yih [2]. Rohana Abdul Hamid [3] has studied effects of Radiation, Joule Heating and Viscous Dissipation on MHD free Convection over a flat Surface with Suction and Injection. Md. Mahmud Alam [4] has investigated Viscous Dissipation and Joule Heating effects on Steady MHD combined Heat and Mass Transfer flow through a porous medium in a rotating system. Postelnicu [5] has studied numerically the influence of a magnetic field on heat and mass transfer by natural convection from vertical porous plate in porous media considering Soret and Dufour effects. Sharma [6] has investigated Effect of Joule Heating on Steady MHD Flow of Low Prandtl Fluid on a Porous Stretching Sheet.

2. MATHEMATICAL MODEL

An unsteady MHD visco-elastic heat and mass transfer flow of an incompressible, electrically conducting viscous fluid past an electrically non-conducting isothermal impulsive vertical infinite plate is considered. The positive x coordinate is measured along the plate in the direction of fluid

motion and the positive y coordinate is measured normal to the plate. A uniform magnetic field of magnitude B_0 is applied in the direction of $y-$axis. It is considered that the plate as well as the fluid is at the same temperature $T(=T_\infty)$ and concentration level $C(=C_\infty)$. It is assumed that the temperature of the plate and spices concentration are raised to $T_w(>T_\infty)$ and $C_w(>C_\infty)$ respectively, which are there after maintained constant, where T_w, C_w are temperature and spices concentration at the wall and T_∞, C_∞ are the temperature and concentration of the species outside the boundary layer respectively. The physical configuration of the problem is furnished in Fig. 1.

The following dimensionless variables have been acquainted to attain the solution of non-linear coupled partial differential equations.

$Y=\frac{yU_0}{\upsilon_1}$, $X=\frac{xU_0}{\upsilon_1}$, $U=\frac{u}{U_0}$, $V=\frac{v}{U_0}$, $\tau=\frac{tU_0^2}{\upsilon_1}$, $\theta=\frac{T-T_\infty}{T_w-T_\infty}$ and $\varphi=\frac{C-C_\infty}{C_w-C_\infty}$.

Continuity Equation;

$$\frac{\partial U}{\partial X}+\frac{\partial V}{\partial Y}=0 \tag{1}$$

Momentum equation;

$$\frac{\partial U}{\partial \tau}+U\frac{\partial U}{\partial X}+V\frac{\partial U}{\partial Y}=\frac{\partial^2 U}{\partial Y^2}+G_r\theta+G_m\varphi+\alpha\left[\frac{\partial^2}{\partial Y^2}\left(\frac{\partial U}{\partial \tau}\right)+V\frac{\partial^3 U}{\partial Y^3}\right]-M_{ha}U \tag{2}$$

Energy equation;

$$\frac{\partial \theta}{\partial \tau}+U\frac{\partial \theta}{\partial Y}+V\frac{\partial \theta}{\partial Y}=\frac{1}{P_r}\frac{\partial^2 \theta}{\partial Y^2}+D_u\frac{\partial^2 \varphi}{\partial Y^2}+J_hU^2+E_c\left(\frac{\partial U}{\partial Y}\right)^2 \tag{3}$$

Concentration equation;

$$\frac{\partial \varphi}{\partial \tau}+U\frac{\partial \varphi}{\partial Y}+V\frac{\partial \varphi}{\partial Y}=\frac{1}{S_c}\frac{\partial^2 \varphi}{\partial Y^2}+S_r\frac{\partial^2 \theta}{\partial Y^2} \tag{4}$$

The corresponding boundary conditions for the problem are given below.

$$\begin{aligned} &U=1, \quad \theta=1, \quad \varphi=1 && \text{at } Y=0 \\ &U=0, \quad \theta=0, \quad \varphi=0 && \text{as } Y\to\infty \end{aligned} \tag{5}$$

where, Grashof number for Heat transfer, $G_r=\frac{g\beta(T_w-T_\infty)\upsilon_1}{U_0^3}$,Grashof number for Mass transfer, $G_m=\frac{g\beta^*(C_w-C_\infty)\upsilon_1}{U_0^3}$, Hartmann number, $M_{ha}=\frac{\sigma B_0^2U_0\upsilon_1}{\rho U_0^3}$, Visco-elastic parameter, $\alpha=\frac{\upsilon_2}{\upsilon_1^2}U_0^2$, Prandtl number, $P_r=\frac{\upsilon_1}{\kappa}$, Dufour number, $D_u=\frac{D\kappa_t}{C_sC_p}\frac{(C_w-C_\infty)}{\upsilon_1(T_w-T_\infty)}$, Schmidt number $S_c=\frac{\upsilon_1}{D}$, Eckert number, $E_c=\frac{U_0^2}{c_p(T_w-T_\infty)}$, Joule Heating parameter, $J_h=M_{ha}E_c$,Sorret number, $S_r=\frac{D\kappa_t}{\upsilon_1}\frac{(T_w-T_\infty)}{(C_w-C_\infty)}$, Suction number $S=\frac{v_0}{U_0}$ and g is the local acceleration due to gravity; β is the thermal expansion coefficient; β^* is the concentration expansion coefficient; υ_1,υ_2 are the kinematic viscosities; ρ is the density of the fluid; B_0 is the constant induced magnetic field; σ is the electrical conductivity; κ is the thermal conductivity; c_p is the specific heat at the constant pressure; c_s is the concentration susceptibility; D is the coefficient of mass diffusivity; κ_t is the thermal diffusion ratio and T is the mean fluid temperature at the wall.

3. SHEAR STRESS, NUSSELT NUMBER and SHERWOOD NUMBER

All the quantities of chief physical interest are shear stress, Nusselt number and Sherwood number. The following equations represent the local and average shear stress at the plate, local shear stress, $\tau_L=\mu\left[\frac{\partial u}{\partial y}+\alpha\left\{\frac{\partial}{\partial y}\left(\frac{\partial u}{\partial t}\right)+v\frac{\partial^2 u}{\partial y^2}\right\}\right]_{y=0}$ and average shear stress, $\tau_A=\mu\int\left[\frac{\partial u}{\partial y}+\alpha\left\{\frac{\partial}{\partial y}\left(\frac{\partial u}{\partial t}\right)+v\frac{\partial^2 u}{\partial y^2}\right\}\right]_{y=0}dx$

which are proportional to $\left[\frac{\partial U}{\partial Y}+\alpha\left\{\frac{\partial}{\partial Y}\left(\frac{\partial U}{\partial \tau}\right)+V\frac{\partial^2 U}{\partial Y^2}\right\}\right]_{Y=0}$ and $\int_0^{100}\left[\frac{\partial U}{\partial Y}+\alpha\left\{\frac{\partial}{\partial Y}\left(\frac{\partial U}{\partial \tau}\right)+V\frac{\partial^2 U}{\partial Y^2}\right\}\right]_{Y=0}dX$ respectively. From the temperature field, the effects of various parameters on the local and average heat transfer coefficients. The following equations represent the local and average heat transfer rate that is well known Nusselt number, local Nusselt number, $N_{uL}=\mu\left(-\frac{\partial T}{\partial y}\right)_{y=0}$ and average Nusselt number, $N_{uA}=\mu\int\left(-\frac{\partial T}{\partial y}\right)_{y=0}dx$ which are proportional to $\left(-\frac{\partial \theta}{\partial Y}\right)_{Y=0}$ and $\int_0^{100}\left(-\frac{\partial \theta}{\partial Y}\right)_{Y=0}dX$ respectively. From the concentration field, the effects of various parameters on the local and average mass transfer coefficients. The following equations represent the local and average mass transfer rate that is well known Sherwood number, local Sherwood number, $S_{hL}=\mu\left(-\frac{\partial C}{\partial y}\right)_{y=0}$ and average Nusselt number, $S_{hA}=\mu\int\left(-\frac{\partial C}{\partial y}\right)_{y=0}dx$ which are proportional to $\left(-\frac{\partial \phi}{\partial Y}\right)_{Y=0}$ and $\int_0^{100}\left(-\frac{\partial \phi}{\partial Y}\right)_{Y=0}dX$ respectively.

4. NUMERICAL SOLUTION

The system of non-dimensional, nonlinear, coupled partial differential equations (1)-(4) with boundary condition (5) is solved numerically using explicit finite difference method. To obtain the difference equations, the region of the flow is divided into a grid or mesh of lines parallel to X and Y axes, where X -axis is taken along the plate and Y -axis is normal to the plate. Here the plate of height $X_{\max}(=100)$ is considered i.e. X varies from 0 to 100 and assumed $Y_{\max}(=35)$ as corresponding to $Y\to\infty$ i.e. Y varies from 0 to 35. There are $m(=180)$ and $n(=180)$ grid spacing in the X and Y directions respectively as shown in **Fig. 2**. It is assumed that ΔX , ΔY are content mesh size along X and Y directions respectively and taken as follows, $\Delta X=0.56(0\le X\le 100)$ and $\Delta Y=0.17(0\le Y\le 35)$ with the smaller time-step, $\Delta\tau=0.005$.

Let U',V',θ' and φ' denote the values of U,V,θ and φ are the end of a time-step respectively. Using the explicit finite difference approximation, the following appropriate set of finite difference equations are obtained as;

$$\frac{U'_{i,j}-U'_{i-1,j}}{\Delta X}+\frac{V_{i,j}-V_{i,j-1}}{\Delta Y}=0 \tag{6}$$

$$\frac{U'_{i,j}-U_{i,j}}{\Delta\tau}+U_{i,j}\frac{U_{i,j}-U_{i-1,j}}{\Delta X}+V_{i,j}\frac{U_{i,j+1}-U_{i,j}}{\Delta Y}=G_r\theta_{i,j}+G_m\varphi+\frac{U_{i,j+1}-2U_{i,j}+U_{i,j-1}}{(\Delta Y)^2}-MU_{i,j}$$
$$+\alpha\left\{\left(\frac{U'_{i,j+1}-2U'_{i,j}+U'_{i,j-1}-U_{i,j+1}+2U_{i,j}-U_{i,j-1}}{(\Delta Y)^2\Delta\tau}\right)\right\}+\alpha\left\{V_{i,j}\left(\frac{U_{i,j+2}-U_{i,j+1}+U_{i,j-1}-U_{i,j-2}}{(\Delta Y)^3}\right)\right\} \tag{7}$$

$$\frac{\theta'_{i,j}-\theta_{i,j}}{\Delta\tau}+U_{i,j}\frac{\theta_{i,j}-\theta_{i-1,j}}{\Delta X}+V_{i,j}\frac{\theta_{i,j+1}-\theta_{i,j}}{\Delta Y}=\frac{1}{P_r}\frac{\theta_{i,j+1}-2\theta_{i,j}+\theta_{i,j-1}}{(\Delta Y)^2}+D_u\frac{\varphi_{i,j+1}-2\varphi_{i,j}+\varphi_{i,j-1}}{(\Delta Y)^2}$$
$$+J_h\left(U_{i,j}\right)^2+E_C\left(\frac{U_{i,j+1}-U_{i,j}}{\Delta Y}\right)^2 \tag{8}$$

$$\frac{\varphi'_{i,j}-\varphi_{i-1,j}}{\Delta\tau}+U_{i,j}\frac{\varphi_{i,j}-\varphi_{i-1,j}}{\Delta X}+V_{i,j}\frac{\varphi_{i,j+1}-\varphi_{i,j}}{\Delta Y}=\frac{1}{S_c}\frac{\varphi_{i,j+1}-2\varphi_{i,j}+\varphi_{i,j-1}}{(\Delta Y)^2}+S_r\frac{\theta_{i,j+1}-2\theta_{i,j}+\theta_{i,j-1}}{(\Delta Y)^2} \tag{9}$$

with the boundary condition;

$U^n_{i,0}=1, V^n_{i,0}=0, \theta^n_{i,0}=1, \varphi^n_{i,0}=1$

$U^n_{i,L}=0, V^n_{i,L}=0, \theta^n_{i,L}=0, \varphi^n_{i,L}=0$ where $L\to\infty$

(10)

The subscript i and j designates the grid points with X and Y coordinates respectively and the superscript n represents a value of time, $\tau = n\Delta\tau$ where $n = 0,1,2,\ldots\ldots$. The velocity (U), temperature (θ) and concentration (φ) distributions at all interior nodal points have been computed by successive applications of the above finite difference equations. The numerical values of the local shear stresses, local Nusselt number and local Sherwood number are evaluated by **Five-point** approximate formula for the derivatives and then the average shear stress, Nusselt number and Sherwood number are calculated by the use of the **Simpson's** 1/3 integration formula. The stability conditions and the convergence criteria are not shown for brevity.

5. RESULTS and DISCUSSION

To investigate the physical situation of the problem, the numerical values and graphs of velocity (U), temperature (θ) and concentration (φ) distributions within the boundary layer have been computed for different values of Dufour number (D_u), Visco-elastic Parameter (α), Magnetic parameter (M_{ha}), Prandtl number (P_r), Schimidt number (S_c), Soret number (S_r), Visco-elastic parameter α and Joule heating parameter (J_h) with the help of a computer programming language Compaq Visual Fortran 6.6a and Tecplot 7. These computed numerical results have been shown graphically. To obtain the steady-state solutions, the computation has been carried out up to $\tau = 80.05$. It is observed that the numerical values of U, θ and φ however, show little changes after $\tau = 45$ and at $\tau = 45$ for all variables are steady-state solutions. To observe the physical situation of the problem, the solutions have been illustrated in Figs. 3-16. Local and Average Shear stress, Nusselt Number and Sherwood number have been displayed for various values of, α, J_h and M_{ha}. In Fig. 3, Local Shear stress is decreased with the increase of viscoelastic parameter (α), in Fig. 4, Local Shear stress is decreased with the increase of Joule Heating parameter (J_h).

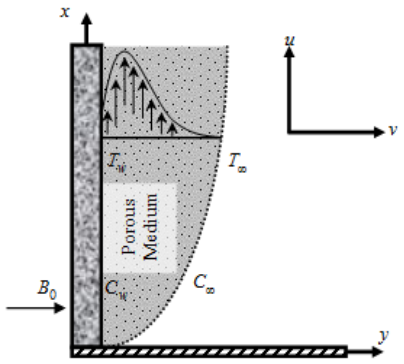

Fig.1: Physical configuration and coordinate system.

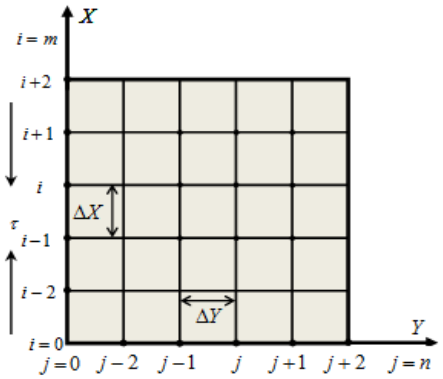

Fig.2: Explicit finite difference system grid.

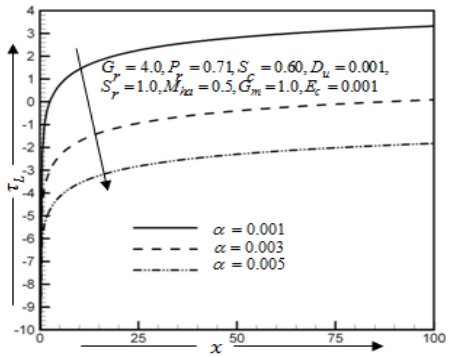

Fig.3: Local Shear stress τ_L for different values of Viscoelastic parameter, α

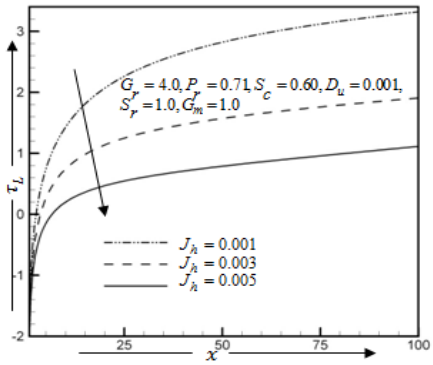

Fig.4: Local Shear stress τ_L for different values of Joule heating parameter, J_h .

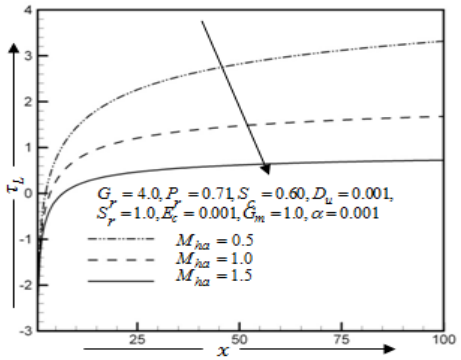

Fig.5: Local Shear stress τ_L for different values of Hartman number, M_{ha} .

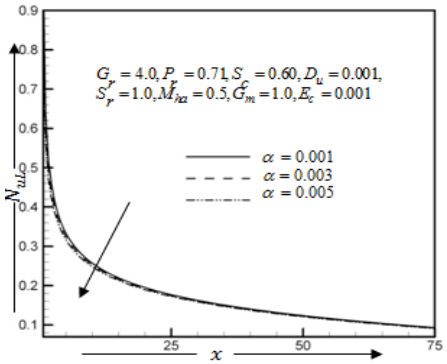

Fig.6: Local Nusselt number N_{uL} for different values of Viscoelastic parameter, α

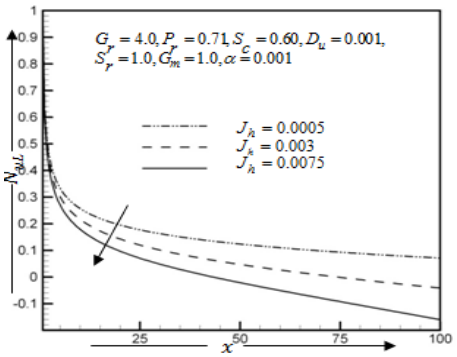

Fig.7: Local Nusselt number N_{uL} for different values of Joule heating parameter, J_h

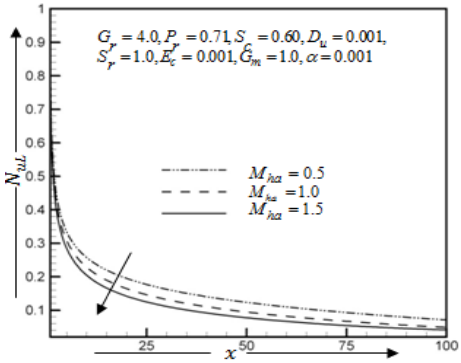

Fig.8: Local Nusselt number N_{uL} for different values of Hartman number, M_{ha}

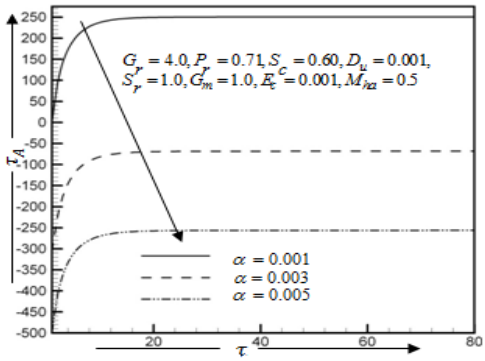

Fig.9: Average Shear Stress τ_A for different values of Viscoelastic parameter, α

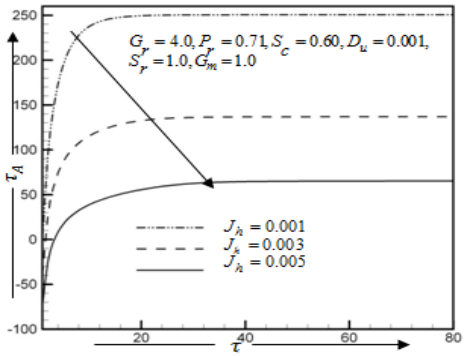

Fig.10: Average Shear stress τ_A for different values of Joule Heating parameter, J_h

In Fig. 5, Local Shear stress is decreased with the increase of Hartman number (M_{ha}) and in Fig. 6, Local Nusselt is decreased with the increase values of Viscoelastic parameter (α) respectively. In Fig. 7, Local Nusselt number is decreased with the increase values of Joule Heating parameter (J_h) and Local Nusselt number is decreased with the increase values of Hartman number (M_{ha}) in Fig. 8 respectively. In Fig. 9, average Shear stress is decreased with the increase values of Viscoelastic parameter (α), and average Shear stress is decreased with the increase values of Joule Heating parameter (J_h) in Fig. 10 respectively.

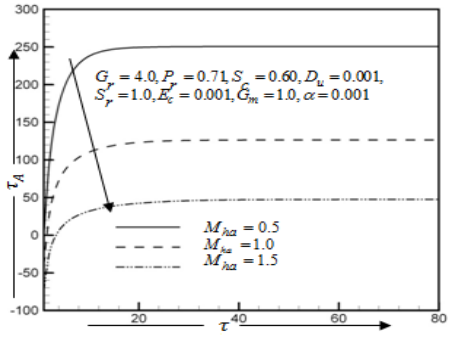

Fig.11: Average Shear stress τ_A for different values of Hartman number, M_{ha}

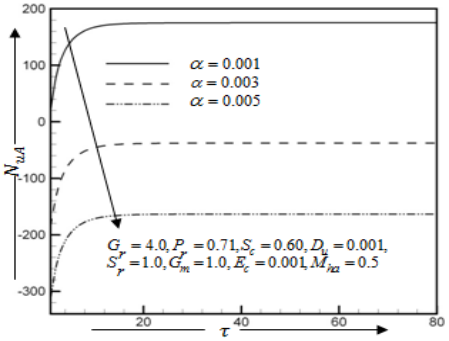

Fig.12: Average Nusselt number N_{uA} for different values of Viscoelastic parameter, α

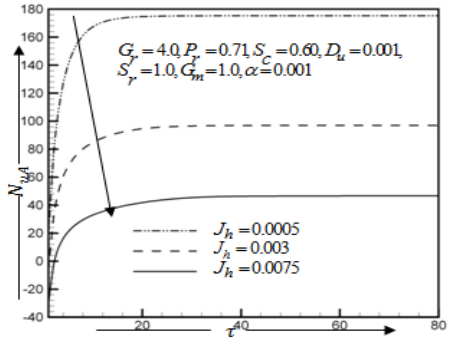

Fig.13: Average Nusselt number N_{uA} for different values of joule heating parameter, J_h

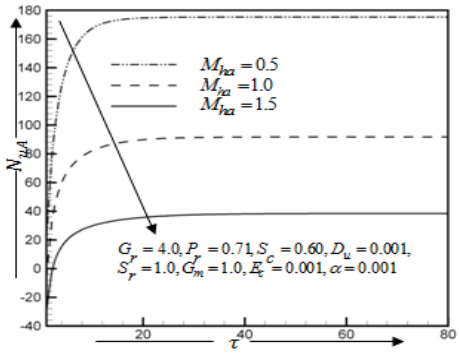

Fig.14: Average Nusselt number N_{uA} for different values of Hartman number, M_{ha}

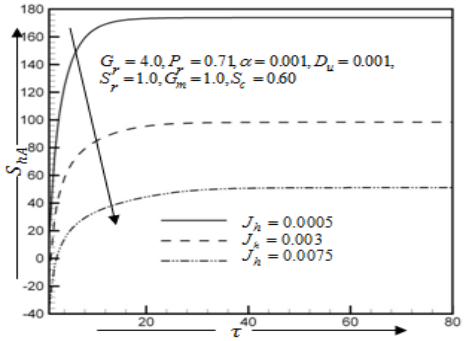

Fig.15: Average Sherwood number S_{hA} for different values of Joule heating parameter, J_h

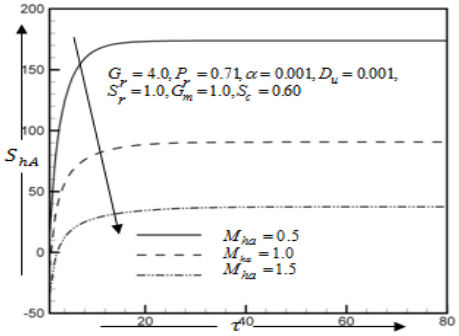

Fig.16: Average Sherwood number S_{hA} for different values of Hartman number, M_{ha}

In Fig. 11, average Shear stress is decreased with the increase of Hartman number (M_{ha}) and in Fig. 12, average Nusselt number is decreased with the increase of Viscoelastic parameter (α) respectively. In Fig. 13, Average Nusselt number is decreased with the increase of Joule Heating parameter (J_h) and Average Nusselt number is decreased with the increase of Hartman number (M_{ha}) in Fig. 14 respectively. In Fig. 15, Average Sherwood number is decreased with the increase of Joule Heating parameter (J_h) and Average Sherwood number is decreased with the increase of Hartman number (M_{ha}) in Fig. 16 respectively.

Table 1: Qualitative comparison of the present results with the previous results

Increased Parameter	The results of Rohana Abdul Hamid, Norihan Md Arifin, Roslinda Nazar, (2013)		Present results				
	u	θ	τ_L	N_{uL}	τ_A	N_{uA}	S_{hA}
α			Dec.	Dec.	Dec.	Dec.	
J_h			Dec.	Dec.	Dec.	Dec.	Dec.
M_{ha}	Dec.	Inc.	Dec.	Dec.	Dec.	Dec.	Dec.

6. CONCLUSION

From comparison table 1, velocity profiles decrease with the increase values of Magnetic parameter, and temperature profiles increase with the increase values of Magnetic parameter. Local Shear stress is decreased with the increase of α, J_h and M_{ha} respectively in Figs. 3-5. Local Nusselt number is decreased with the increase of α, J_h and M_{ha} respectively in Figs. 6-8. Average Shear stress is decreased with the increase of α, J_h and M_{ha} respectively in Figs. 9-11. Average Nusselt number is decreased with the increase of α, J_h and M_{ha} respectively in Figs. 12-14. Average Sherwood number is decreased with the increase of J_h and M_{ha} respectively in Figs. 15-16.

REERENCES

[1] Alim, M.A., M.D. Alam and A. Mamun, (2007), "Joule heating effect on the coupling of conduction with magnetohydrodynamic free convection flow from a vertical flat plate", Nonlinear Analysis: Modelling and Control, vol. 12(3), pp. 307-316.
[2] K. A. Yih, (2000), "Viscous and Joule heating effects on Non-Darcy MHD natural convection flow over a permeable sphere in porous media with internal heat generation", Int. Commun. Heat Mass, vol. 27(4), pp. 591–600.
[3] Rohana Abdul Hamid, Norihan Md Arifin, Roslinda Nazar, (2013), "Effects of Radiation, Joule Heating and Viscous Dissipation on MHD Marangoni Convection over a Flat Surface with Suction and Injection", World Applied Sciences Journal, vol. 21(6), pp. 933-938.
[4] M. M. Alam, M. D. Hossain and M. A. Hossain,(2011), "Viscous Dissipation and Joule Heating effects on Steady MHD combined Heat and Mass Transfer flow through a porous medium in a rotating system", Journal of Naval Architecture and Marine Engineering, vol. 2, pp.105-120.
[5] Postelnicu, A. (2004), "Influence of a magnetic field on heat and mass transfer by natural convection from vertical surfaces in porous media considering Soret and Dufour effects", Internatonal Journal of Heat and Mass Transfer, vol. 47, no.6-7, pp.1467-1472.
[6] P. R. Sharma, K. Dadheech, (2012), Effect of Joule Heating on Steady MHD Flow of Low Prandtl Fluid on a Porous Stretching Sheet, International Journal of Engineering Research & Technology (IJERT),Vol. 1 Issue 3.

THE EFFECTS OF PRESSURE DRIVEN FLOW THROUGH A ROTATING CURVED MICRO-CHANNEL

Md. Saidul Islam [1], **Md. Zohurul Islam** [2], **Rabindra Nath Mondal** [3]

[1)] Department of Mathematics; Faculty of Science, Engineering and Technology, Hamdard University Bangladesh, Narayangong, Bangladesh.

[2)] Mathematics Discipline, Science, Engineering & Technology School, Khulna University, Khulna-9208.

[3)] Department of Mathematics, Jagannath University, Dhaka.
Email: saeedmathku@yahoo.com

ABSTRACT: To obtain this study, a comprehensive numerical study is presented for the unsteady flow characteristics through a rotating curved micro channel with rectangular cross section. Numerical calculations are carried out over a wide range of the Taylor number $-500 \le Tr \le 1000$ for two cases *Case I*: Positive rotation; and *Case II*: Negative rotation. To solve the system of non-linear differential equations we used spectral method. The rotation of the channel about the center of curvature is imposed for both the positive and negative rotation, and the effects of rotation (Carioles force) on the flow characteristics are investigated. As a result, multiple solutions of steady, periodic and chaotic solutions with symmetric and asymmetric multi-vortex solutions are obtained.

Keywords: Rotating curved duct, secondary flow, unsteady solution, Dean number, Flow pattern.

1. INTRODUCTION

Flow and heat transfer in a curved micro channel have attracted considerable attention because of their ample applications in fluids engineering. Due to engineering applications and their intricacy, the flow in a rotating curved micro channel has become one of the most challenging research fields of fluid mechanics. Since rotating machines were introduced into engineering applications, such as rotating systems, gas turbines, electric generators, heat exchangers, cooling system and some separation processes, scientists have paid considerable attention to study rotating curved duct flows. The readers are referred to Nandakumar and Masliyah (1986) and Yanase *et al.* (2002) for some outstanding reviews on curved duct flows.

The fluid flowing in a rotating curved micro channel is subjected to two forces: the *Coriolis force* due to rotation and the *centrifugal force* due to curvature. For isothermal flows of a constant property fluid, the Coriolis force tends to produce vortices while centrifugal force is purely hydrostatic. When a temperature induced variation of fluid density occurs in non-isothermal flows, both Coriolis and centrifugal type buoyancy forces can contribute to the generation of vortices. These two effects of rotation either enhance or counteract each other in a non-linear manner depending on the direction of wall heat flux and the flow domain. Therefore, the effect of systematic rotation is more subtle and complicated and yields new; richer features of flow and heat transfer in general, bifurcation and stability in particular, for non-isothermal flows. Selmi and Nandakumer (1999) and Yamamoto *et al.* (1999) performed studies on the flow in a rotating curved rectangular duct. Recently, Mondal *et al.* (2007) performed numerical prediction of the non-isothermal flow through a rotating curved square duct. Very recently, Mondal *et al.* (2012) performed numerical investigation of the non-isothermal flows through a rotating curved square duct and obtained substantial results. However, there is no known study on rotating curved rectangular micro channel flows with buoyancy effect. The present paper is, therefore, an attempt to fill up this gap. Studying the effects of rotation on the flow characteristics, caused by the buoyancy forces, is an important objective of the present study.

2. MATHEMATICAL FORMULATIONS

Consider a hydro-dynamically and thermally fully developed two-dimensional flow of viscous incompressible fluid through a rotating curved duct with rectangular cross section, whose height and widths are $2h$ and $2l$, respectively. The coordinate system with the relevant notation is shown in

Fig. 1, where x' and y' axes are taken to be in the horizontal and vertical directions respectively, and z' is the axial direction. The system rotates at a constant angular velocity Ω_T around the y' axis. It is assumed that the outer wall of the duct is heated while the inner wall cooled. u, v and w be the velocity components in the x', y' and z' directions respectively. All the variables are non-dimensionalized.

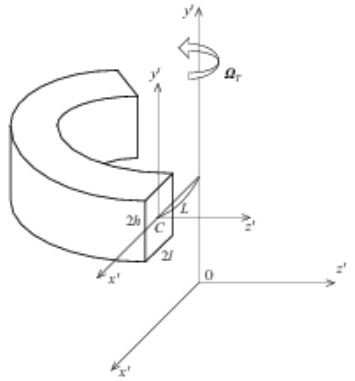

Fig. 1: Coordinate system of the rotating curved duct

The sectional stream function ψ is introduced as

$$u = \frac{1}{1+\delta x}\frac{\partial \psi}{\partial \bar{y}}, \quad v = -\frac{1}{1+\delta x}\frac{\partial \psi}{\partial x} \tag{1}$$

Then, the basic equations for the axial velocity w, the stream function ψ and temperature T are expressed in terms of non-dimensional variables as:

$$(1+\delta x)\frac{\partial w}{\partial t} + \frac{\partial(w,\psi)}{\partial(x,y)} - Dn + \frac{\delta^2 w}{1+\delta x} = (1+\delta x)\Delta_2 w - \frac{\partial}{1+\delta x}\frac{\partial \psi}{\partial y}w + \delta\frac{\partial w}{\partial x} - \delta Tr\frac{\partial \psi}{\partial y} \tag{2}$$

$$\left(\Delta_2 - \frac{\delta}{1+\delta x}\frac{\partial}{\partial x}\right)\frac{\partial \psi}{\partial t} = -\frac{1}{(1+\delta x)}\frac{\partial(\Delta_2\psi,\psi)}{\partial(x,y)} + \frac{\delta}{(1+\delta x)^2}\left[\frac{\partial \psi}{\partial y}\left(2\Delta_2\psi - \frac{3\delta}{1+\delta x}\frac{\partial \psi}{\partial x} + \frac{\partial^2\psi}{\partial x^2}\right) - \frac{\partial \psi}{\partial x}\frac{\partial^2\psi}{\partial x \partial y}\right]$$

$$+\frac{\delta}{(1+\delta x)^2}\times\left[3\delta\frac{\partial^2\psi}{\partial x^2} - \frac{3\delta^2}{1+\delta x}\frac{\partial \psi}{\partial x}\right] - \frac{2\delta}{1+\delta x}\frac{\partial}{\partial x}\Delta_2\psi + w\frac{\partial}{\partial y} + \Delta_2{}^2\psi - G_r(1+\delta x)\frac{\partial T}{\partial x} + \frac{1}{2}Tr\frac{\partial w}{\partial y}, \tag{3}$$

$$\frac{\partial T}{\partial t} + \frac{1}{(1+\delta x)}\frac{\partial(T,\psi)}{\partial(x,y)} = \frac{1}{\Pr}\left(\Delta_2 T + \frac{\delta}{1+\delta x}\frac{\partial T}{\partial x}\right) \tag{4}$$

The non-dimensional parameters Dn, the Dean number, Gr, the Grashof number, Tr, the Taylor number and $\Pr$, the Prandtl number, which appear in equation (2) to (4) are defined as:

$$Dn = \frac{Gl^3}{\mu\upsilon}\sqrt{\frac{2l}{L}}, \quad Gr = \frac{\beta g \Delta T l^3}{\upsilon^2}, \quad Tr = \frac{2\sqrt{2\delta}\,\Omega_T l^3}{\upsilon\delta}, \Pr = \frac{\upsilon}{\kappa} \tag{5}$$

where the parameters denote their usual meaning. The rigid boundary conditions for w and ψ are used as

$$w(\pm 1, y) = w(x, \pm 1) = \psi(\pm 1, y) = \psi(x, \pm 1) = \frac{\partial \psi}{\partial x}(\pm 1, y) = \frac{\partial \psi}{\partial y}(x, \pm 1) = 0 \tag{6}$$

and the temperature T is assumed to be constant on the walls as:

$$T(1, y) = 1, \; T(-1, y) = -1, T(x, \pm 1) = x \tag{7}$$

3. NUMERICAL METHODS

In order to solve the Equations (2) to (4) numerically, the spectral method is used. By this method the expansion functions $\phi_n(x)$ and $\psi_n(x)$ are expressed as

$$\left.\begin{aligned}\phi_n(x) &= (1-x^2)\,C_n(x),\\ \psi_n(x) &= (1-x^2)^2 C_n(x)\end{aligned}\right\} \tag{8}$$

Where $C_n(x) = \cos(n\cos^{-1}(x))$ is the n^{th} order Chebyshev polynomial. $w(x,y,t)$, $\psi(x,y,t)$ and $T(x,y,t)$ are expanded in terms of the expansion functions $\phi_n(x)$ and $\psi_n(x)$ as

$$\left.\begin{aligned}w(x,y,t) &= \sum_{m=0}^{M}\sum_{n=0}^{N} w_{mn}(t)\varphi_m(x)\varphi_n(y)\\ \psi(x,y,t) &= \sum_{m=0}^{M}\sum_{n=0}^{N} \psi_{mn}(t)\psi_m(x)\psi_n(y).\\ T(x,,y,t) &= \sum_{m=0}^{M}\sum_{n=0}^{N} T_{mn}\varphi_m(x)\varphi_n(y)+x\end{aligned}\right\} \tag{9}$$

where M and N are the truncation numbers in the x and y directions respectively. In order to calculate the unsteady solutions, the Crank-Nicolson and Adams-Bashforth methods together with the function expansion (9) and the collocation methods are applied to Eqs. (2) to (4).

4. RESISTANCE COEFFICIENT

We use the resistance coefficient λ as one of the representative quantities of the flow state. It is also called the *hydraulic resistance coefficient*, and is generally used in fluids engineering, defined as

$$\frac{P_1^* - P_2^*}{\Delta z^*} = \frac{\lambda}{dh^*}\frac{1}{2}\rho\left\langle w^*\right\rangle^2, \tag{10}$$

where quantities with an asterisk denote the dimensional ones, $\langle\,\rangle$ stands for the mean over the cross section of the rectangular duct, and $d_h^* = 4(2d\times 4d)/(4d\times 8d)$. Since $\left(P_1^* - P_2^*\right)/\Delta z^* = G$, λ is related to the mean non-dimensional axial velocity $\langle w\rangle$ as

$$\lambda = \frac{16\sqrt{2\delta}\,Dn}{3\langle w\rangle^2}, \tag{11}$$

where $\langle w\rangle = \sqrt{2\delta}\,d/\nu\left\langle w^*\right\rangle$.

5. RESULT AND DISCUSSION

In this study, we have investigated time evolution of the resistance coefficient λ for the flows through a curved rectangular duct of constant curvature $\delta = 0.1$. We studied the unsteady solutions of the flows at Dean Numbers (Dn) 1000 and 2000 and with changing Tailor Numbers (Tr). We investigated the flow characteristics for both the positive and negative rotation of the of the duct for the Tailor Numbers $-500 \le Tr \le 1000$ for three cases: Case *I*: positive rotation for aspect ratio $a = 1$ and Case *II*: negative rotation for aspect ratio $a = 2$ and $a = 3$.

5.1. Positive rotation

5.1.1. Aspect ratio 1, *Dn=1000*

Time Evolution of the unsteady solutions for, *Tr=100*

In order to study the non-linear behavior of the unsteady solution, we first investigate the time evolution of λ for aspect ratio $a = 1$. We studied the time evolution of the resistance coefficient λ for $Dn = 1000$ and $Tr = 100$ as shown in the Fig.2(a). We found that the flow is periodic for $Tr = 100$. Contours of secondary flow of one period of oscillation at time $26.10 \leq t \leq 27.10$ are shown in Fig.2(b). From this figure we find that secondary flow is two-, three-, and four-vortex solution. The axial flows shifted to the outer wall the Dean vortex are generated.

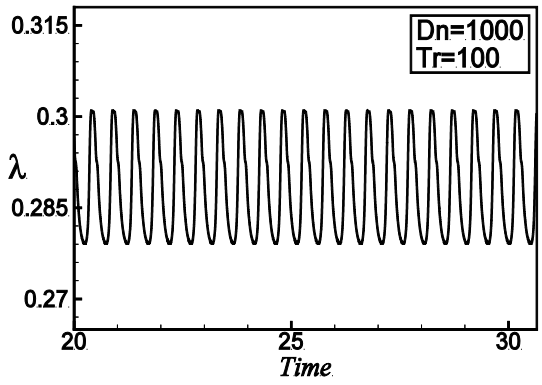

(a)

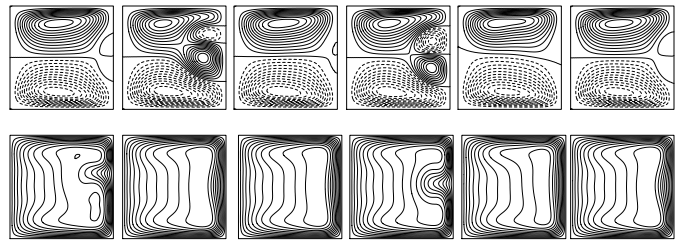

(b)

Fig. 2(a): Time evolution of λ for the unsteady solutions at time $20 \leq t \leq 30.5$ for $Dn = 1000$ and $Tr = 100$ for the aspect ratio $a = 1$. (b) Contours of secondary flow (top) and axial flow distribution (bottom) at $26.10 \leq t \leq 27.10$

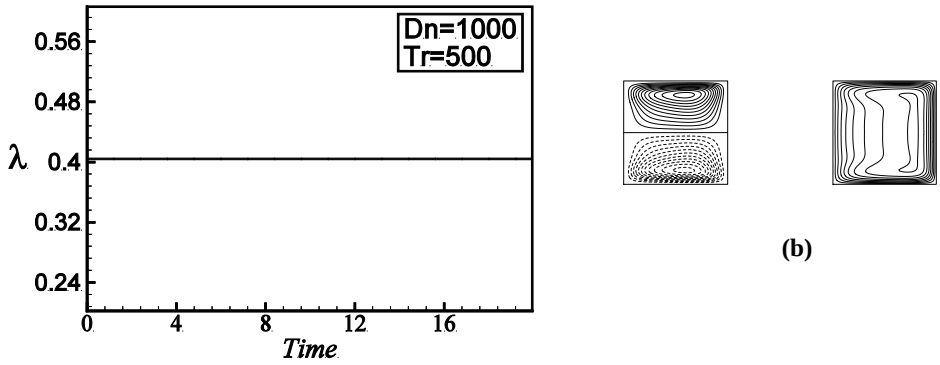

(b)

(a)

Fig.3(a): Time evolution of λ for the unsteady solutions at time $0 \leq t \leq 20$ for $Dn = 1000$ and $Tr = 500$ for the aspect ratio $a = 1$. **(b)** Contours of secondary flow and axial flow distribution at $t = 15.00$

Time Evolution of the unsteady solutions for $Tr = 500$

We studied the time evolution of the resistance coefficient λ for $Dn = 1000$ and $Tr = 500$ as shown in the Fig.3(a). As seen in Fig.3 the flow is steady state solution for $Tr = 500$. Since the flow is steady-state, we show a single contour of secondary flow pattern and axial flow distribution in Fig.3(b). As seen Fig.3(b) the secondary flow is two vortex solution.

5.1.2 Aspect ratio $a = 2$, $Dn = 1000$

Time Evolution of the unsteady solutions for $Tr = 100$

In order to study the non-linear behavior of the unsteady solution, then we investigated the time evolution of λ for aspect ratio $a = 2$. We studied the time evolution of the resistance coefficient λ for $Dn = 1000$ and $Tr = 100$ as shown in the Fig.8. We found that the flow oscillates irregularly that is the flow is chaotic for $Tr = 100$. The axial flow is shifted to the outer wall and the flow is consistent with the secondary flow as in Fig.8.Typical contours of secondary flow and axial flow distribution for $Dn = 1000$ and $Tr = 100$ is shown in the Fig.8 for $26.00 \leq t \leq 28.00$. As seen in Fig.8, the secondary flow is a four-, and six-vortex solution.

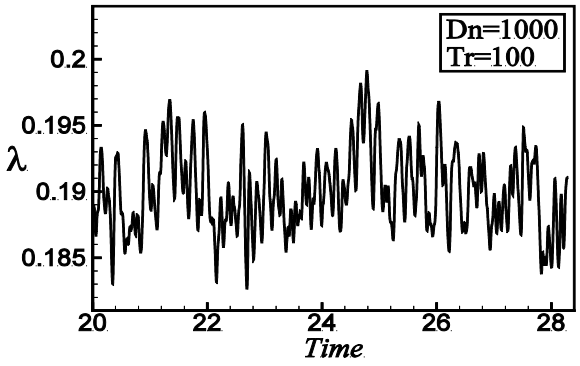

(a)

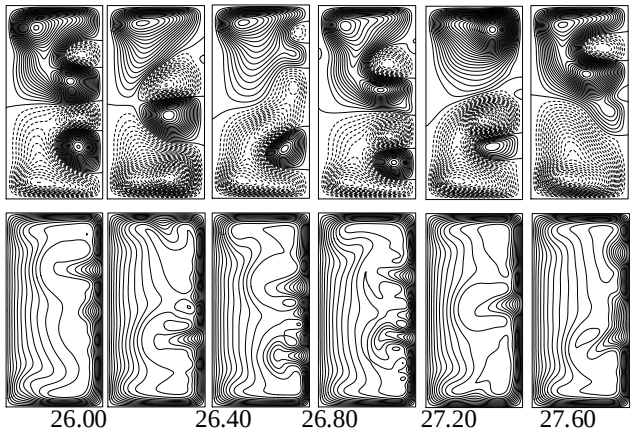

(b)

Fig.4(a): Time evolution of λ for the unsteady solutions at time $20.0 \leq t \leq 28.4$ for $Dn = 1000$ and $Tr = 100$ for the aspect ratio $a = 2$. **(b)** Contours of secondary flow (top) and axial flow distribution (bottom) at $26.00 \leq t \leq 28.00$

6. CONCLUSION

In order to study the non-linear behavior of the unsteady solution, we first investigate the time evolution of λ for aspect ratio $a - 1$. We studied the time evolution of the resistance coefficient λ for $Dn = 1000$ and $Tr = 100$. After a comprehensive survey over the parametric ranges, for the positive rotation of the square channel flow, we found that the flow is periodic with asymmetric two- and four-vortex solutions for $Tr = 100$. if Tr is increased the periodic flow turns into steady-state. Then we investigated the time evolution of λ for aspect ratio $a = 2$. For the rectangular channel flow the unsteady flow is chaotic. If we increased the Tailor Number into wide range the unsteady flow is also chaotic. In order to study the non-linear behavior of the unsteady solution, we first investigate the time evolution of λ for aspect ratio $a = 1$ and $Dn = 1000$. After a comprehensive survey over the parametric ranges, it is found that, for the negative rotation of the square duct flow, we found that the flow is periodic for $Tr = -100$. If Tr is decreased the periodic flow turns into steady-state. Again we investigated the time evolution of λ for aspect ratio $a = 1$. The flow steady-state for $Tr = -100$ and $Dn = 2000$. Then we decreased Tr, we found that the flow is multi-periodic with four-, and six-vortex solution for $Tr = -300$. Again we decreased Tr, the flow is chaotic with is a four-, six-, and eight-vortex solution for $Tr = -500$.

REFERENCES

[1] Berger, S.A., Talbot, L., Yao, L. S. (1983). Flow in Curved Pipes, *Annual. Rev. Fluid. Mech*., Vol. **35**, pp. 461-512.
[2] Barua, S. N. (1954). Secondary flow in a rotating straight pipe. *Proc. R. Soc. Lond. A* Vol. **227**, pp. 133-139.
[3] Belaidi, A., Jahnson, M. W. and Humphrey, J.A.C. (1992). Flow instability in a curved duct of rectangular cross section, *ASME Trans., Journal of Fluids Engineering* Vol. **114**, pp.585-591
[4] Dean, W. R. (1927). Note on the motion of fluid in a curved pipe. *Phil. Mag .Vol.* **4** (20) pp. 208- 223.
[5] Dean .W. R. (1928). The streamline motion of fluid in a curved pipe, *Phil. Mag.* Vol. **5** (30), pp. 673-695.
[6] Daskopoulos, P. & Lenhoff , A. M. (1990). Flow in curved ducts. Part 2. Rotating ducts, *Journal of Fluid Mechanics*, Vol. **217**, pp. 575-593.

MACROSCOPIC TWO-PHASE FLOW MODELING OF A DENSE SUSPENSION

Shimul Hazra
Department of Mechanical Engineering
BUET ,Dhaka-1000, Bangladesh.

ABSTRACT: A finite element based macroscopic two-phase flow model has been presented. The flow of a dense suspension consisting of light, solid particle in a liquid placed between two concentric cylinders was simulated. The dynamics of a suspension is modeled by a momentum transport equation for the mixture, a continuity equation, and a transport equation for the solid phase volume fraction. Next the simulation results are compared with two dimensional NMR images of solid fraction profiles in the same suspension undergoing flow between rotating concentric cylinders with two different initial conditions to verify the numerical results. Here shear induced particle migration is significant. Under these conditions, it has been found that simulating the correct initial condition is critical to matching with the experimental results. When this is done, the model results compare well with the experiments. Liquid-solid mixtures are important in a variety of industrial fields, such as oil and gas refinement, paper manufacturing, food processing, slurry transport, and wastewater treatment.

Keywords: macroscopic modeling, transport equations, momentum transport equation, Couette flow, shear-induced particle migration.

1. INTRODUCTION

Liquid-solid mixtures (suspensions) are important in a variety of industrial fields, such as oil and gas refinement, paper manufacturing, food processing and wastewater treatment. These include such application as batch sedimentation, hydraulic fracturing technology and slurry transport. Particle separation due to density differences occurs in many non-colloidal mixtures of particles and liquids, and many processing activities can benefit from knowledge of the physics of systems undergoing sedimentation or rotation. For this reason, researchers are trying to develop a modeling capability that allows to predict the flow and particle transport properties of arbitrary buoyant suspensions in complex geometries.

It is now well known that flowing suspensions of particles in a liquid have been known to exhibit particle migration even in creeping flow and in the absence of significant nonhydrodynamic or gravitational effects [1–3]. In particular, Leighton and Acrivos [2] proposed scaling arguments that identified three causes of particle migration, namely, gradients in shear rate, concentration, and relative viscosity. These arguments are the basis of a constitutive model for the evolution of particle concentration in a flowing suspension proposed by Phillips et al. [4] and referred to as the diffusive flux model. This constitutive description couples a generalized Newtonian momentum equation where the local viscosity of the suspension is dependent on the local volume fraction of solids with an evolution equation to describe the shear-induced migration of the suspended particles. Subia et al. [5] extended the diffusive flux model from viscometric to multidimensional flows using a scalar shear rate invariant to describe the shear induced migration and solved the resulting equations with the finite element method.

The term viscous resuspension was first used by Leighton and Acrivos [6] to describe the resuspension of sedimented particles due to shear flow. Complex flow and particles profiles can arise resulting from a balance of gravitational flux on the particles, which tends to lead to segregation, with shear-induced migration, which can cause remixing. A number of experimental studies have been carried out to look at the effects of viscous resuspension in pipe, channel and Couette geometries [7–11]. However, little work has been done on computational modeling of viscous resuspension. Most of the existing modeling work has been at the particle-level, which though elucidating, can be computationally intensive and difficult to apply to arbitrary geometries [12–14]. Continuum approaches have a greater chance of being useful for modeling a variety of flow fields and suspensions. However, much of the continuum modeling work has used simplified equations that

are either analytically tractable or solved with rudimentary numerical methods [15]. For instance, Shauly et al. [16] modeled viscous resuspension in a polydisperse system and looked at a variety of geometries, but simplified the equations to examine one-dimensional flows only. Miskin [17; 18] model viscous resuspension in channel flows, but simplify the equations to two-dimensions and use a specialized finite difference method.

One exception is the pivotal work of Zhang and Acrivos [19] who formulated a general numerical approach to modeling multidimensional viscous resuspension with few simplifying assumptions. They used a continuum approach and extended the work of Leighton and Acrivos [2] to non-neutrally buoyant suspensions with the inclusion of a hindered settling function in the particle evolution equation and a buoyancy term in the momentum equation. They discretized the theoretical model with the finite element method and examined fully developed flow profiles in a pipe flow and obtained good agreement with experiment.

R. Rao, L. Mondy [20] examined the applicability of a continuum model of viscous resuspension and base much of their work on that of Zhang and Acrivos [19] and Phillips [4], with some significant modifications.They simulated the behavior of concentrated suspensions of large, monodisperse spheres with a Galerkin, finite element, Navier–Stokes solver into which is incorporated a continuum constitutive relationship based on the diffusive flux model but modified to allow gravity effects. Results of the model are then compared with experiment. The experiments involve using nuclear magnetic resonance (NMR) imaging to determine noninvasively the evolution of the solids-concentration profiles of suspensions as they separate when subjected to a variety of slow flows in which gravity has a substantial effect. The model was first tested on batch sedimentation to insure the correct form of the hindered settling function. Once the model was validated for settling without flow, a more complex problem was simulated that included shear as well as buoyancy effects.

This study is a CFD modeling simulating the flow of a dense suspension consisting of light, solid particles in a liquid placed between two concentric cylinders. The inner cylinder rotates while the outer is fixed. Results of the model are then compared with experimental results[20].

2. PHYSICAL MODEL

The radii of the two cylinders are 0.64 cm and 2.54 cm, respectively. The inner cylinder rotates at a steady rate of 55 rpm. With the cylinder centered at (0,0), the fluid and particle motion is small along the direction of the cylinder axes. Therefore to use a 2-dimensional model is enough. Fig. 1(a) shows the corresponding geometry.

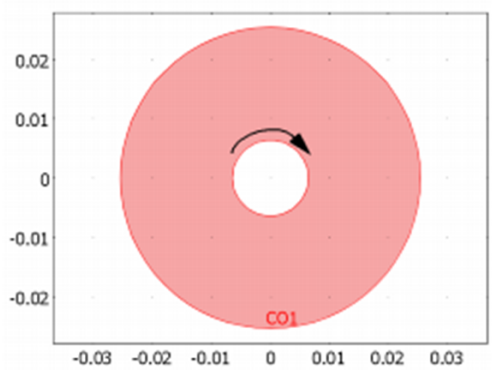

Fig. 1(a): Geometry of the Couette device. The inner cylinder rotates, the outer one is fixed.

3. MATHEMATICAL MODEL

(i) Governing equations

The dynamics of a suspension is modeled by a momentum transport equation for the mixture, a continuity equation, and a transport equation for the solid phase volume fraction. The Mixture Model application mode automatically sets up these equations. It uses the following equation to model the momentum transport:

$$\rho\frac{\partial \mathbf{u}}{\partial t} + \rho(\mathbf{u}.\nabla)\mathbf{u} = -\nabla p - \nabla.\left(\rho c_s(1-c_s)\mathbf{u}_{slip}\mathbf{u}_{slip}\right) + \nabla.[\eta(\nabla\mathbf{u} + \nabla\mathbf{u}^T)] + \rho\mathbf{g} \quad (1)$$

where $\mathbf{u}$ is the mass averaged mixture velocity (m/s), p denotes the pressure (Pa), $\mathbf{g}$ refers to the gravity vector m/s^2. c_s is the dimensionless particle mass fraction, and $\mathbf{u}_{slip}$ gives the relative velocity between the solid and the liquid phases (m/s). Further, $\rho = (1-\phi_s)\rho_f + \phi_s\rho_s$ is the mixture density, where ρ_f and ρ_s are the pure-phase densities (kg/m^3) of liquid and solids, respectively, and ϕ_s is the solid-phase volume fraction (m^3/m^3). Finally, η represents the mixture viscosity (Ns/m^2) according to the Krieger-type expression

$$\eta = \eta_f\left(1-\frac{\phi_s}{\phi_{max}}\right)^{-2.5\phi_{max}} \quad (2)$$

where η_f is the dynamic viscosity of the pure fluid and ϕ_{max} is the maximum packing concentration. The mixture model uses the following form of the continuity equation

$$(\rho_f - \rho_s)\left[\nabla.(\phi_s(1-c_s)\mathbf{u}_{slip})\right] + \rho_f(\nabla.\mathbf{u}) = 0 \quad (3)$$

The transport equation for the solid-phase volume fraction is

$$\frac{\partial \phi_s}{\partial t} + \nabla.(\phi_s\mathbf{u}_s) = 0 \quad (4)$$

The solid-phase velocity, $\mathbf{u}_s$, is given by $\mathbf{u}_s = \mathbf{u} + (1-c_s)\mathbf{u}_{slip}$. Consequently, Equation (4) is equivalent to

$$\frac{\partial \phi_s}{\partial t} + \nabla.(\phi_s\mathbf{u} + \phi_s(1-c_s)\mathbf{u}_{slip}) = 0 \quad (5)$$

Rao and others [20] formulate the continuity equation and the particle transport in a slightly different way. Instead of the slip velocity, $\mathbf{u}_{slip}$, they define a particle flux, $\mathbf{J}_s$ (kg /(m^{2}s)), and write the continuity equation as

$$\nabla.\mathbf{u} = \frac{\rho_s-\rho_f}{\rho_s\rho_f}(\nabla.\mathbf{J}_s) \quad (6)$$

and the solid phase transport according to

$$\frac{\partial \phi_s}{\partial t} + \nabla.(\phi_s\mathbf{u}) = -\frac{(\nabla.\mathbf{J}_s)}{\rho_s} \quad (7)$$

By comparing Equation (6) and Equation (7) with Equation (3) and Equation (5), it is clear that they are equivalent if

$$\mathbf{u}_{slip} = \frac{\mathbf{J}_s}{\phi_s\rho_s(1-c_s)} \quad (8)$$

In this model particle flux, $\mathbf{J}_s$ is used as suggested by Subia and others [5] and Rao and others [20], but the open and editable format of COMSOL Multiphysics makes it possible to specify the expression arbitrarily. Following Rao and others, the particle flux is

$$\frac{\mathbf{J}_s}{\rho_s} = \left[\phi D_\phi\nabla(\dot{\gamma}\phi) + \phi^2\dot{\gamma}D_\mu\nabla(\ln\mu)\right] + f_h\,\mathbf{u}_{st}\,\phi \quad (9)$$

Here, $\mathbf{u}_{st}$ is the settling velocity (m/s) of a single particle surrounded by fluid and D_ϕ and D_μ are empirically fitted parameters (m^2) given by

$$D_\phi = .41a^2,\ D_\mu = .62a^2$$

where a is the particle radius (m). The shear rate tensor, $\underline{\dot{\gamma}}$ (1/s), is given by

$$\underline{\dot{\gamma}} = \nabla \mathbf{u} + (\nabla \mathbf{u})^T \quad (10)$$

and its magnitude by

$$\dot{\gamma} = \sqrt{\frac{1}{2}\left(\underline{\dot{\gamma}} : \underline{\dot{\gamma}}\right)} \quad (11)$$

which for a 2-dimensional problem is

$$\dot{\gamma} = \sqrt{\frac{1}{2}\left(4u_x^2 + 2\left(u_y + v_x\right)^2 + 4v_y^2\right)} \quad (12)$$

The settling velocity, $\mathbf{u}_{st}$, for a single spherical particle surrounded by pure fluid is given by

$$\mathbf{u}_{st} = \frac{2a^2}{9}\frac{(\rho_s - \rho_f)}{\eta_s}\mathbf{g} \quad (13)$$

For several particles in a fluid, the settling velocity is lower. To account for the surrounding particles, the settling velocity for a single particle is multiplied by the hindering function, f_h, defined as

$$f_h = \frac{\eta_f(1-\phi_{av})}{\eta} \quad (14)$$

where ϕ_{av} is the average solid phase volume fraction in the suspension, η_f is the dynamic viscosity of the pure fluid (Ns/m^2), and η is the mixture viscosity.

(ii) Boundary conditions

The boundary conditions of the present study are described as follows.

1. There is no particle flux through the boundaries.
2. The suspension velocity satisfies no-slip conditions at all walls.
3. The fluid and particle motion is small along the direction of the cylinder axes

(iii) Initial conditions:

The Initial conditions of the present study are described as follows

1. the particles are evenly distributed within the device
2. the particles are initially gathered at the top of the device.

4. GRID SENSITIVITY TEST

A commercial finite element package COMSOL Multiphysics 3.4 was used to obtain the solution. Triangular quadratic Lagrange elements were employed to discretize the computational domain. As the accurateness of the numerical results depends stalwartly on the mesh sensitivity, approximately 2848 elements with minimum element quality 0.8143,1496 mesh point and element area ratio 0.114 were decided to obtain the result. Relatively fine meshes were used near the inner cylinder boundary.

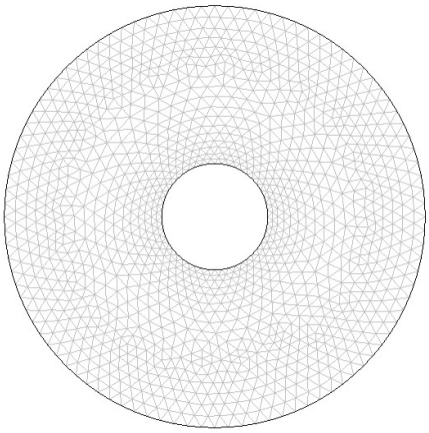

Fig. 1(b): Surface Mesh Setup

5. RESULTS

Couette flow: *well mixed initial conditions*

A comparison of experimental and finite element results for the well-mixed initial condition experiment are presented in Fig.2. Fig.2(a) depicts the NMR images of concentration profiles taken at 0, 34.90, 104.72, and 456 seconds. Even though the sample loading time has been minimized, the experimental image taken at rest reveals inhomogeneous distribution of particles prior to turning of the inner cylinder. A small, pure fluid zone at the bottom of the device has developed while zones containing as much as 50 per cent volume fraction of particles are scattered near the inner cylinder. Interestingly, the clear zone at the bottom is carried around along the streamlines towards the top of the outer cylinder and persisted even past 100 turns before viscous resuspension remixes the suspended particles in that region.

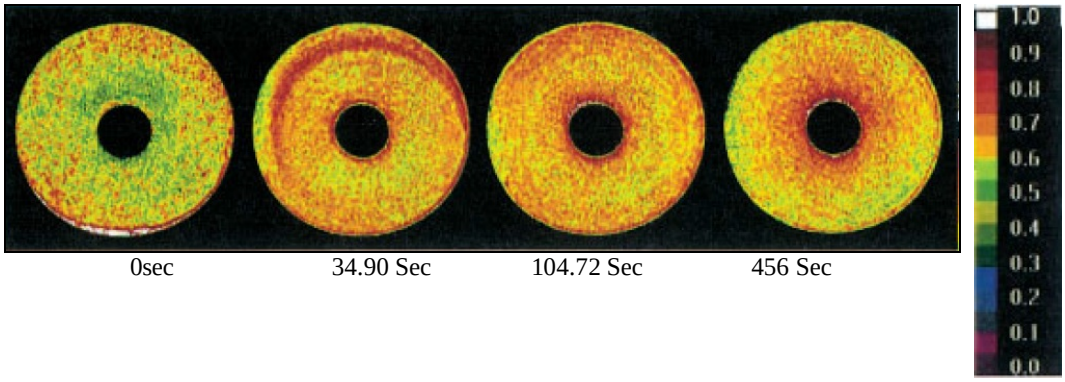

0sec 34.90 Sec 104.72 Sec 456 Sec

(a)

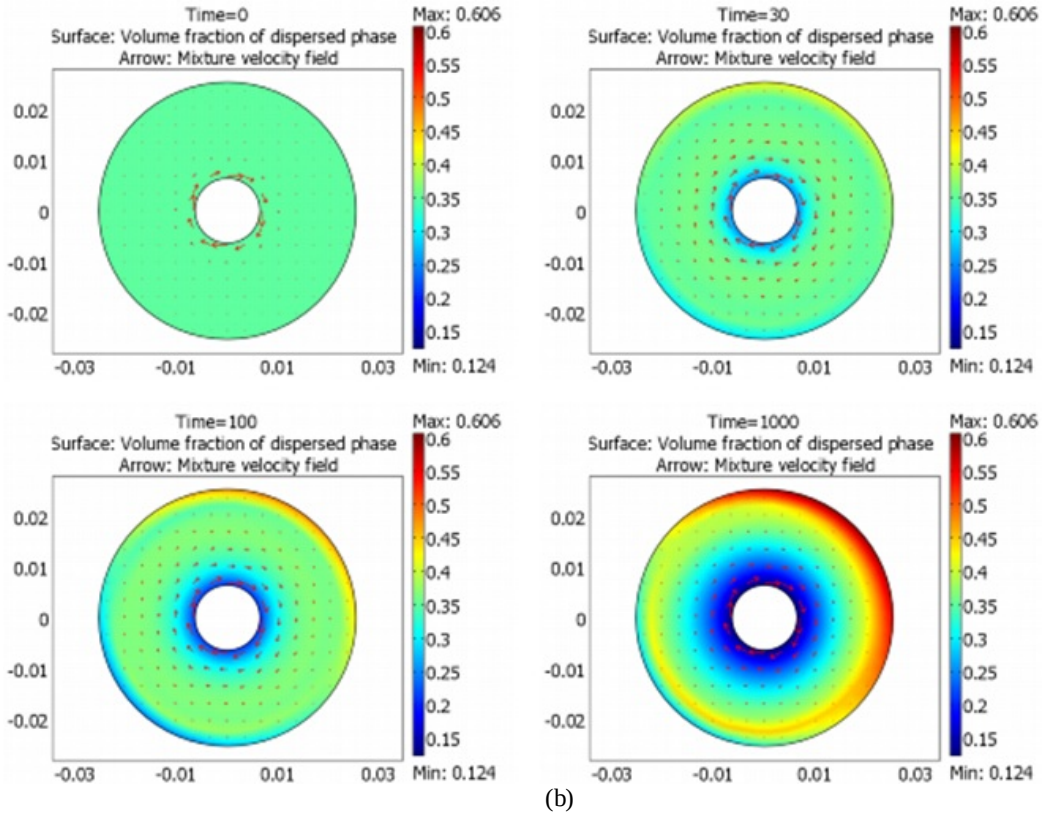

(b)

Fig.2: Couette flow concentration profiles as a function of time for initially well-mixedsuspension. (a) NMR images[20]; (b) simulation results.

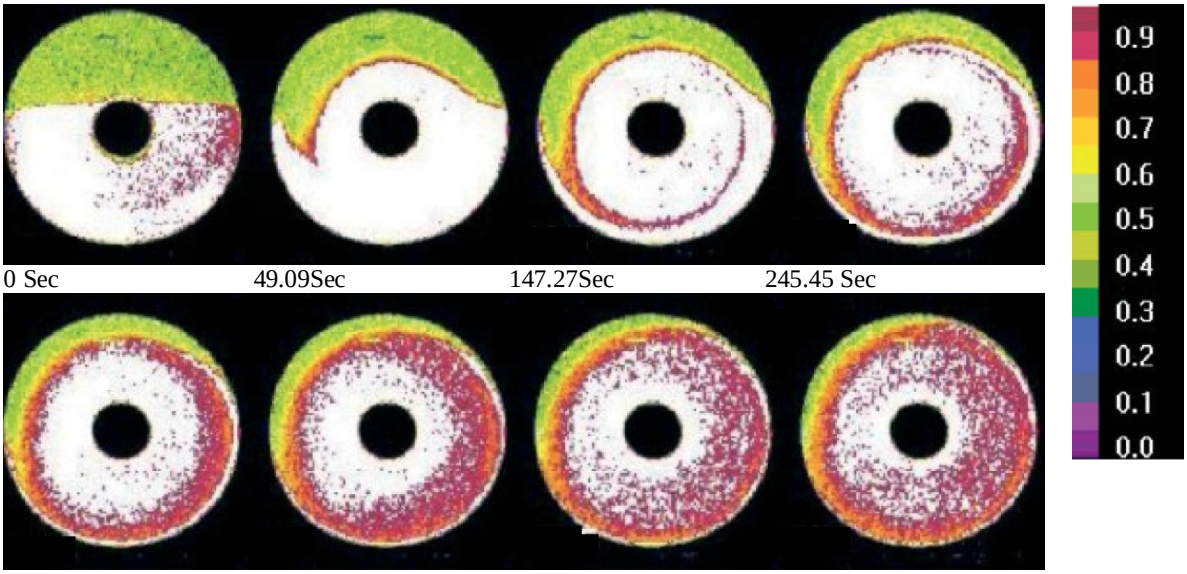

(a)

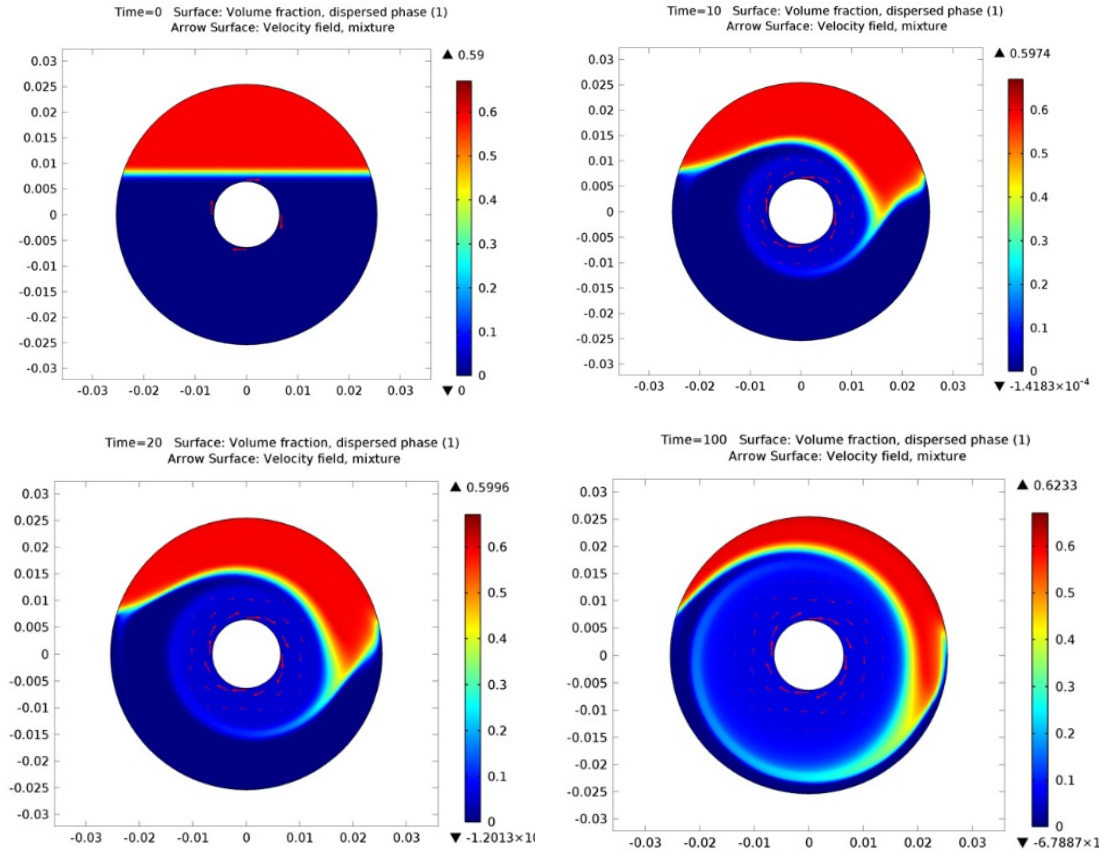

(b)

Fig 3: Couette flow concentration profiles at different times. (a) NMR images, 59 per cent top, 0 per cent bottom initially[20]; (b) simulation results

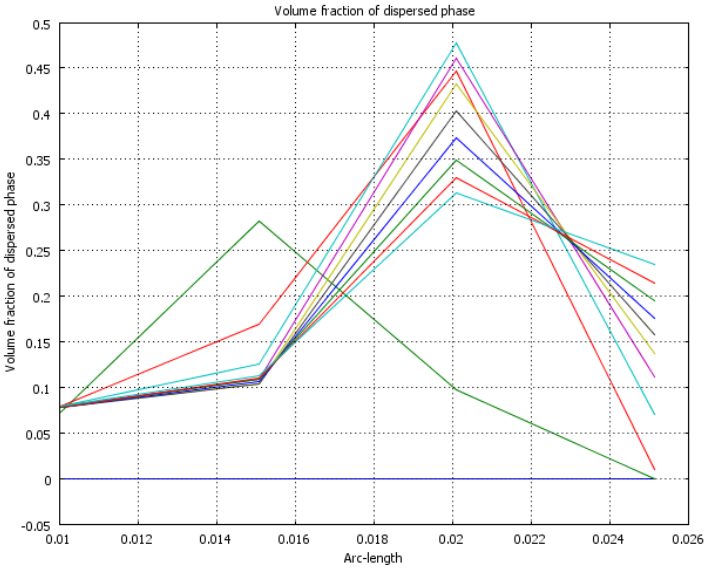

Fig 4:Simulation result of Volume fraction of dispersed phase versus Arc-length

The image taken at 34.90 seconds also reveal a small packed zone to the left of the low concentration band. This is probably due to accumulation of particles displaced by the low concentration band. The concentration profile at 456 seconds no longer shows signs of the initial inhomogeneity, instead it shows pronounced radial gradient particle concentration due to shear-induced migration.Snapshots of simulated particle concentration at similar time points are shown in Fig 2(b).Based on what was observed experimentally, the assumption of initially 'uniform' solution is not applied to this problem. Instead, the simulation allowed the particles to float quiescently until a clear zone with the size comparable to that observed in the experiment has developed; this consisted of about 5 min flotation without turning of the inner cylinder in both the experiment and simulation. Interestingly, when the simulations were carried out without matching the initial conditions the results matched the experiments qualitatively, but did not capture the transient correct behavior.

In the first snapshot, the model-generated profile shows different regions of low and high particle concentrations. Particles have packed near the bottom of the inner cylinder as well as along the top wall of the outer cylinder. Other than the clear zone created at the bottom, there is also a small band of low concentration particles at the top of the inner cylinder. After 30 seconds, the regions of high and low concentrations along the outer cylinder still remain, while the inhomogeneity along the inner cylinder remixes quickly as shear-induced migration becomes dominant in that region. Although the packed zone at the top of the device is not observed in the experiment, the comparison of the dynamic profiles show good qualitative agreement between the model and the experiment. At 100 seconds, the high concentration band along the outer cylinder thins out as more particles remix into the bulk. Eventually the band disappears around 175 srconds, well before the formation of another high concentration region at the top of the outer cylinder, clearly visible in that last snapshot at 1000 seconds. Such a concentrated region is not evident in the experiment, but can be viewed as a region where the suspended particles are held in place as its flotation rate cancels out the convective/diffusive flux.

Couette flow: *sedimented initial condition*
Fig 3 shows a comparison of the NMR and finite element results for the initially sedimented suspension. In Fig 3 (a), the NMR images for the second experiment indicate that the particles have packed to the top of the Couette gap before the motor is turned on. The concentration of the packed zone is 59 per cent, or 1 per cent over its theoretical maximum packing value. This is conceivable since particles of one size may exhibit some degree of polydispersity. Contrary to the first experiment, though, this packed zone thins out at a slower rate. This may be attributed to the inertial effect as it dominates the dynamics initially. Any mixing at higher turns occurs close to the outer

cylinder wall while the region around the inner cylinder wall remains devoid of particles due to shear-induced migration.

The simulated concentration profiles in Fig 3(b) agree qualitatively with the NMR imaging results. An initial two-phase mixture moves in almost solid body rotation of the maximum packing zone. In fact, simulations that were run without particle diffusion show almost identical early-time results. However, the early mixing in the simulation occurs more quickly than in the experiment. By 246.54 second the effects of shear-induced migration can be seen in Fig 3(a). This migration retards the mixing of the outer layers and the simulation actually begins to lag the experimental results. However, qualitative features, such as the asymmetry created by buoyancy effects interacting with the turn direction, are preserved. There are a number of reasons that may have caused the discrepancies. To simulate solidlike behavior of the maximum packing zone, we set the viscosity to ramp to a very large value (to approximate infinity) as the concentration reaches maximum packing. However, the material in this zone cannot support stresses as a true solid would. Also, the resuspension mechanism, where individual particles peal off the packed zone, cannot be mimicked by a continuum equation. Potentially at two-phase model could be more successful at capturing the resuspension behavior. More accurate dynamics may also be achieved with a finer mesh and a better numerical scheme that can handle time-variant concentration discontinuities. The numerical method used has trouble capturing behavior when concentrations vary from maximum packing to pure fluid over an element. The kinematic shock and discontinuous concentration lead to numerical instabilities and oscillations in the solution.

6. CONCLUSION

In this study there is a good qualitative agreement between the simulations and the experiments. However, discrepancies exist between the shape of the concentration profiles for the quiescent sedimentation data and the numerical model. Numerical difficulties also occur in situations where large changes in concentration and thus viscosity occur over short distances. For this reason, the model of the shear flow in the well-mixed wide-gap Couette was better behaved than the quiescent settling and the Couette with the sedimented initial condition. Many improvements to the model are being investigated to improve the agreement between the numerical results and the experimental data.

REFERENCES

[1] Karnis A, Goldsmith HL, Mason SG. The kinetics of flowing dispersions I. Concentrated suspensions of rigid particles. *Journal of Colloid Interface Science* 1966; 22:531–533.
[2] Leighton D, Acrivos A. The shear-induced migration of particles in concentrated suspensions. *Journal of Fluid Mechanics* 1987; 181:415–439.
[3] Abbott JR, Tetlow N, Graham AL, Altobelli SA, Fukushima E, Mondy LA, Stephens TS. Experimental observations of particle migration in concentrated suspensions: Couette flows. *Journal of Rheology* 1991; 35:773–795.
[4] Phillips RJ, Armstrong RC, Brown RA, Graham AL, Abott JR. A constitutive equation for concentrated suspensions that accounts for shear-induced particle migration. *Physics of Fluids* A 1992; 4:30–40.
[5] Subia SR, Ingber MS, Mondy LA, Altobelli SA, Graham AL. Modelling of concentrated suspensions using a continuum constitutive equation. *Journal of Fluid Mechanics* 1998; 373:193–219.
[6] Leighton D, Acrivos A. Viscous resuspension. *Chemical Engineering Science* 1986; 6:1377–1384.
[7] Chapman BK, Leighton DT, Jr. Dynamics viscous resuspension. *International Journal of Multiphase Flow* 1991; 17:469–483.
[8] Acrivos A, Mauri R, Fan X. Shear-induced resuspension in a Couette device. *International Journal of Multiphase Flow* 1993; 19:797–802.
[9] Krishnan GP, Leighton DT. Dynamic viscous resuspension of bidisperse suspensions—I. Effective diffusivity.*International Journal of Multiphase Flow* 1995; 21:721.
[10] Hallworth MA, Huppert HE. Abrupt transitions in high-concentration, particle-driven gravity currents. *Physics of Fluids* 1998; 10:1083.

[11] Breedveld V, Van Den Ende D, Tripathi A, Acrivos A. The measurement of the shear-induced particle and fluid tracer diffusivities in concentrated suspensions by a novel method. *Journal of Fluid Mechanics* 1998;375:297–318.
[12] Andrews MJ, O'Rourke PJ. The multiphase particle-in-cell (MP-PIC) method for dense particulate flows. *International Journal of Multiphase Flow* 1996; 22:379–402.
[13] Hu HH. Direct simulation of flows of solid–liquid mixtures. International Journal of Multiphase Flow 1996;22:335.
[14] Morris JF, Brady JF. Pressure-driven flow of a suspension: buoyancy effects. *International Journal of Multiphase Flow* 1998; 24:105–130.
[15] Schainger U, Acrivos A, Zhang K. Viscous resuspension of a sediment within a laminar and strati..*International Journal of Multiphase Flow* 1990; 16:567–578.
[16] Shauly A, Wachs A, Nir A. Shear-induced particle resuspension in settling polydisperse concentrated suspension.*International Journal of Multiphase Flow* 2000; 26:1–15.
[17] Miskin I, Elliot E, Ingham DB, Hammond PS. Steady suspension flows into two-dimensional horizontal and inclined channels. *International Journal of Multiphase Flow* 1996; 22:1223.
[18] Miskin I, Elliot E, Ingham DB, Hammond PS. The viscous resuspension of particles in an inclined rectangular fracture. *International Journal of Multiphase Flow* 1996; 22:403.
[19] Zhang K, Acrivos A. Viscous resuspension in fully developed laminar pipe flows. *International Journal of Multiphase Flow* 1994; 20:579–591.
[20] R. Rao, L. Mondy, A. Sun, and S. Altobelli, "A numerical and experimental study of batch sedimentation and viscous resuspension," *Int. J. Num. Methods in Fluids*, vol. 39, pp. 465–483, 2002.

ON APPLICABILITY OF AN OPEN SOURCE COMPUTATIONAL FLUID DYNAMICS TECHNIQUE FOR QUALITY SHIP DESIGNS IN BANGLADESH

S. Shabnam[1],M. M. Rahaman[1], N. M. G. Zakaria[1],M.T.Ali[1]and Md. R. H. Khondoker[1]
[1]Department of Naval Architecture & Marine Engineering, Bangladesh University of Engineering and Technology, Dhaka-1000, Bangladesh
Corresponding Author: shabnam@name.buet.ac.bd

ABSTRACT: Shipbuilding industry has grown to be one of the major foreign exchange earners in Bangladesh. But due to lack of physical testing facilities in Bangladesh, it is very difficult for designers to develop a new hull form. Nowadays, evaluation of new hull form based on Computation Fluid Dynamics (CFD) technique is used extensively by the naval architects all over the world. Present study investigates the possibility of an open source based CFD method named OpenFOAM. It is seen from present analysis that OpenFOAM can be an effective and efficient tool for the shipdesigners in Bangladesh in terms of costs and infrastructure when compared with other commercial based CFD methods.

Keyword: Ship design, Bangladesh, CFD, Open Source, OpenFOAM

1. INTRODUCTION:

Computational Fluid Dynamics (CFD) is a powerful numerical technique to obtain the solution of the governing equations of fluid flows. The advancement of algorithm for solving non-linear problems and rapid increase of computational infrastructure has made it possible to explore numerical solutions for the complex fluid flow problems.

For naval architects, it is necessary to get a suitable design in the preliminary stage. A suitable design ensures that the three principal components of a ship; hull, propeller and rudder are working together efficiently. Also, shipbuilding industry and market requires a hull form that can run at a higher speed with less fuel consumption. Therefore, the hull form should be designed to have a minimal resistance. Again the propulsion system should be designed so that it can operate in an optimum wake field without cavitation. The designer also needs to choose the parameters of the rudder which will be the best for this optimized hull and propulsion system for safe and proper maneuvering. Nowadays, the most commonly used experimentalmethod for testing hull and propeller is towing tank/cavitation tunnel testing. However, due to high cost and time required for model testing, the hull and propeller are usually checked in the final design stage. Computational Fluid Dynamics (CFD) offers a great opportunity in this regard. Based on this numerical technique, detailed evaluation of several design alternatives can be done in the early design stage without having to rely solely on the physical tests. Using CFD simulations, the behavior of hull surface in calm water and in waves can easily be understood. The results from different simulations provide a useful insight for improving the design.

Bangladesh has a long history in shipbuilding. This is mainly because of favorable geographic location and cheap labor costs. Although there are a handful number of medium and large sized shipyards Bangladesh, but most of the hull forms and basic drawings of the exported ships are purchased from foreign design firms. One of the main obstacles for developing a new hull form is the absence of model testing facility in Bangladesh. On the other hand, improving a hull form design based entirely on physical tests is a time consuming and expensive procedure. Due to the considerable improvement in CFD techniques, most hull form designers in Modern ship yards all over the world are using CFD tools for the development of new hull forms. The practical reason behind choosing CFD as a design tool is its ability to evaluate more options with less time and cost for a particular hull form design.

As Bangladesh has no model testing facility at present, CFD tools are the best feasible solution to Bangladeshi ship designers for the purpose of designing a new hull form, or refining the existing design of a ship to improve the ship's performance at sea. Shipyards in Bangladesh can meet the growing

demand to reduce hydrodynamic resistance and gain maximum speed of vessels in a seaway by implementing and adopting CFD techniques in their design offices. If Bangladesh acquires the ability to design efficient ships on its own, then there will be no need to purchase the designs from elsewhere which will reduce the cost of shipbuilding in a great deal. It will also help our shipbuilders to sustain the global competition and get more orders from clients abroad.

A large number of CFD (commercial/open source) tools are now readily available to use for design purposes. The commercial CFD tools require an excessively high purchasing cost or annual license fees. In a developing country like Bangladesh, a good replacement of commercial CFD tools will be open source CFD codes. This paper explores the potential application of an open source CFD code named Open FOAM [1]to our shipbuilding industry in the design stage in order to build an efficienthull form.

2. SHIPBUILDING SECTOR IN BANGLADESH

2.1 SHIPBUILDING HISTORY ANDTHE GROWTH OF LOCAL SHIPYARDS

Bangladesh is a maritime nation with 166,000 square km of sea area and more than 200 rivers with a total length of 22,155 km[2]. Shipbuilding is one of the earliest industries developed in Bangladesh beginning from wooden-bodied passenger vessel and gradually improving to steel-body construction of merchant ships. With a long maritime history and convenient geographical position, Bangladesh enjoys several advantages when it comes to shipbuilding. According to a study carried out by the Danish embassy in Bangladesh, shipbuilding in Bangladesh is 15 percent cheaper than anywhere else in the world[3]. This is due to fact that Bangladesh has comparatively a lower cost of skilled workforce than any shipbuilding nation of the world and can offer the best combination of cost, quality and productivity with its fast growing young workforce. Along with the presence of nearly 250 thousand skilled and semi-skilled workers and the industry related educational and training institutes, Bangladesh has a friendly environment and relaxed government regulatory requirements.

A significant milestone in the history of our shipbuilding was marked when Ananda Shipyard and Slipways Ltd. (ASSL), one of the leading local shipbuilders, signed a joint deal with two German Companies to build eight container ships worth 125 million dollars which was the single biggest export order since our nation's birth[4]. Since then, ASSL have manufactured and exported ferries, cargo vessels, container ships, tugboats, passenger vessels and ocean-going multi-purpose ships with ranges from 2900 to 7250 DWT. Another pioneer shipbuilding industry of our country, Western Marine Shipyard Ltd. (WMSL) has also produced ships up to 100m in length and exported quite a large number of vessels to European countries [5]. Khulna Shipyard has started the construction of a total of five warships on March, 2011. Two of the warships, each one armed with two 37 millimeter cannons and two 20 millimeter anti-aircraft gunshad already been handed over to the Bangladesh Navy[6].

Shipyards inour country have built vessels for countries including Denmark, Germany, Finland, Holland, Mozambique, Singapore etc.which are worth more than $500m (£320m)[7]. According to the data of the Export Promotion Bureau, Bangladesh[8] has earned about Tk. 288 cr. as foreign exchange in the financial year of 2010-11 and about Tk. 364 cr. in the financial year of 2011-12 in the shipbuilding sector. To facilitate shipbuilding, Germanischer Lloyd (GL), a renowned international classification society has declared Bangladesh as a shipbuilding nation of international standards in September 2008, inspiring more foreign investment in this sector[9].

At present, Bangladesh has more than hundred small and medium sized shipbuilding yards, with most of them serving the domestic market. These shipyards are primarily engaged in new building and repairing of inland and coastal vessels of upto 3500DWT[10]. Among these shipyards, at least ten are capable of constructing international standard and export quiality ships. According to a report published in the national daily newspaper of Bangladesh named "Daily Prothom Alo", shipbuilders of Bangladesh are expecting about $2-5 billion of export orders from several countries of European Union and Africa in the coming year[11].

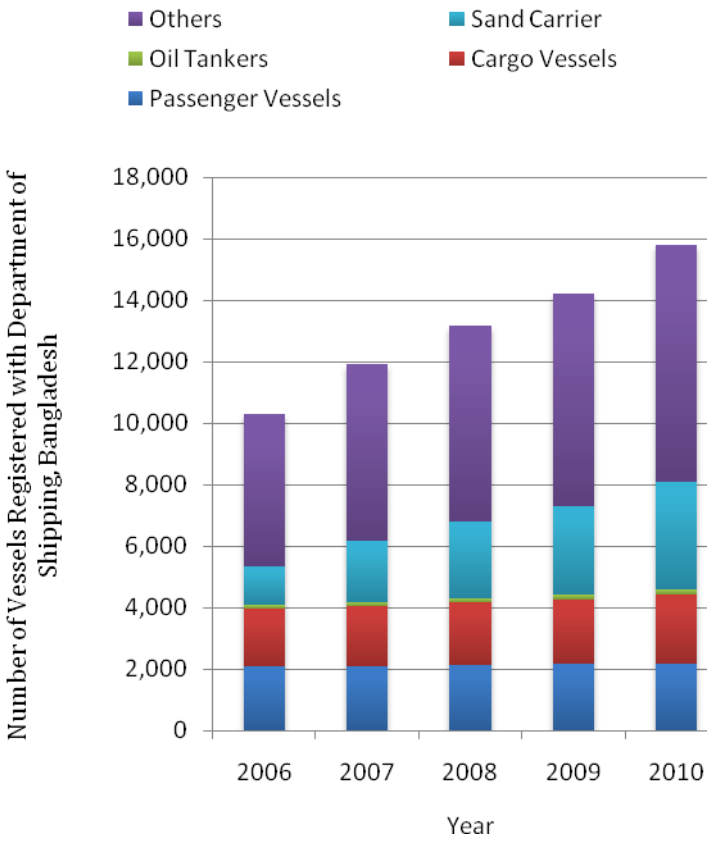

Fig. 1: Annual growth of registered vessels in Bangladesh (2006-2010)[12].

The trade and commerce of our country also depends on our shipbuilding industry. Nearly 70% of the country's cargo and 90% of total oil products are transported by small sized ships, cargo vessels and multi-purpose ships through its coastal and inland waterways[13]. As this is a riverine country, hundreds of thousands of people use small and medium sized passenger vessels, ferries, catamarans to travel from one part of Bangladesh to another, and most of these vessels are built in this country.

2.2 CURRENT SITUATION OF SHIP DESIGN IN BANGLADESH

Although Bangladeshi shipyards have successfully captured a market of small and medium sized ocean going vessels, but most of the basic drawings of the constructed ships are either outsourced or purchased from foreign design firms. It takes about 5~7% of the production cost to purchase a complete set of basic and production drawings for a ship from foreign design firms. Again, the nearest towing tank facility where Bangladeshi ship designers undertook model testing, is in Indian Institute of Technology (IIT) Kharagpur, India. To estimate the bare hull resistance of a ship involved an expenditure of about Tk. 8~10 lakhs which constitutes a large portion of the production cost.

A number of reasons lie behind the reluctance of our shipbuilders in designing the ships themselves:

- Lack of expertise of our local ship designers
- Inexperience of our naval architects in creating basic design of ships
- Unavailability of sufficient number of design houses
- Absence of model testing facility in our country
- Involvement of huge expenditure for performing experiments of ship hull in towing tank facilities abroad
- Pressure to meet the deadline of delivering the vessels to the owners

- Insufficient computational capabilities of office computers
- Expensiveness of commercial CFD software

2.3 NAVAL ARCHITECTS OF BANGLADESH

At present, Bangladesh University of Engineering & Technology (BUET) offers Undergraduate and Post-Graduate degrees in the field of Naval Architecture & Marine Engineering. The department currently has an intake of 59 students and since its establishment about 500 naval architects has been graduated from this department. Military Institute of Science & Technology (MIST) also opened a Department of Naval Architecture & Marine Engineering since 2012 with an intake of 30 students.

A significant portion of Graduate Naval Architects of Bangladesh goes abroad for either higher study or employment in international shipyards as the small number of design firms in Bangladesh employs only a handful of naval architects. Most of the design jobs include repetitive tasks and involves no further research to obtain an improved design. Major shipyards in Bangladesh are also reluctant to employ naval architects as they sub-contract the basic design to other local/international design offices. So the naval architects of Bangladesh hardly get the opportunity to apply their academic knowledge to develop of new hull forms or modify the existing designs.

3. SHIP HULL FORM DESIGN PROCEDURE

3.1 CONVENTIONAL DESIGN PROCEDURE

Traditionally the design of a ship was done in either of the two ways:

a. Designing a ship based on the parameters of an experimental series or previously constructed basis ships.
b. Creating an entirely new hull form where the design procedure would incorporate a good number of model tests. The process involves design, test, redesign, test etc. sometimes involving more than 10 models each with slight variations.

In order to find the combination of design variables that generates a new hull form with optimal hydrodynamic performance (e.g. drag and seakeeping) under given constraints, a tremendous number of performance evaluations are required.Ship designers need reasonably accurate estimates of the factors affecting the flow pattern around the hull to obtain the suitable hull form based on mission requirements.

The basic idea of a model testing is to experiment with a scale-model and then the results are transformed to full-scale ship which gives us an understanding of the behavior of the hull. A sequence of different model tests are performed to assess the efficiency of propeller and to have a deeper insight into the performance of the designed hull.

3.2 CFD BASED PROCEDURE

Computational fluid dynamics (CFD) is now widely adopted as a performance prediction tool for hull design. Thanks to the great advancement of computer performance recently, computational analysis of ship resistance, propeller-ship hull interaction, propulsion performance, sea-keeping and maneuveringare conductedon regular basis and the results are being applied to actual design of ships.
CFD analysis technique is based on the method of numerically solving the Navier-Stokes equations using a computational grid and domain generated around the ship hull. With the help of post processing, CFD simulation provides a detailed three-dimensional description of pressure fields and flow conditions, presenting a significant insight into the physical phenomena that takes place around the hull.
Also, to reduce hull resistance, CFD simulation for pressure distribution is conducted so that the hull form parameters affecting the hull resistance are selected and thoroughly changed to create an efficient hull. Propulsion efficiency is evaluated by calculating the flow distribution around a ship in self-propelled condition with the help of CFD techniques. This CFD based design process enables the naval

architect to create a suitable hull form that has minimal resistance and high propulsion efficiency thus requiring less horsepower. Since this method is sufficiently accurate and reliable, it is used for designing hull forms even in the conceptual design stage.

3.3 COMPARISON BETWEEN CONVENTIONAL AND CFD METHOD

As the competition grows in the shipbuilding industry, ship designers strive to deliver the most effective and efficient hull form possible within the constraints of time, budget, and performance requirements. Although the design procedure of a new hull based entirely on predictions of hydrodynamic performance of full-scale ships from model tests are well accepted for their accurate results, this is no longer feasible due to time-to-market requirements from ship-owners.

Due to several reasons CFD has become an indispensable part of the design process. For instance, CFD modeling is almost always faster than physical modeling. In many cases, design results from a CFD model are available several weeks before similar results from a scale model. And the more complicated or repetitive the model geometry is, the more advantage the CFD model has. This has to do with three factors: 1) the CFD mesh can usually be built faster than a scale model can be fabricated, 2) once a CFD model is built, it can be run simultaneously on separate computers 3) modification of the CFD mesh is comparatively less time consuming and easier than having to build a new model. Thus, a large number of designs can be evaluated at the same time, while only a few physical models can be tested to evaluate the final design selection.

Combining CAD (computer-aided design) to generate new hull shapes in concert with CFD to analyze these hull shapes allows for rapid design explorations prior to final model testing. CFD allows the preselection of the most promising design among various alternatives. Then often only one or two models are actually tested to validate the intended performance features in the design. The initial design process and selection of a new hull form based on traditional model testing and CFD simulation is described in the flow charts of Fig. 2 and Fig. 3.

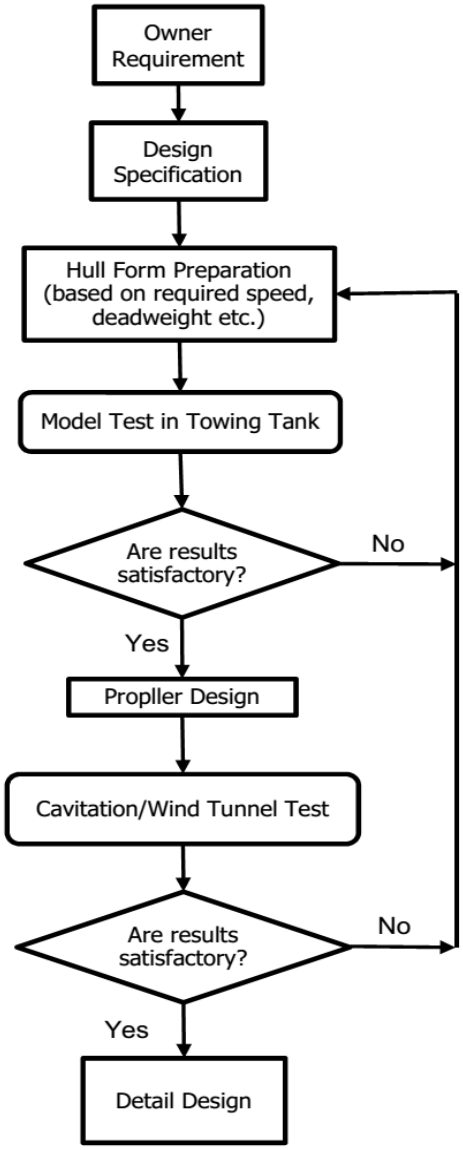

Fig. 2: Design process based on traditional model tests.

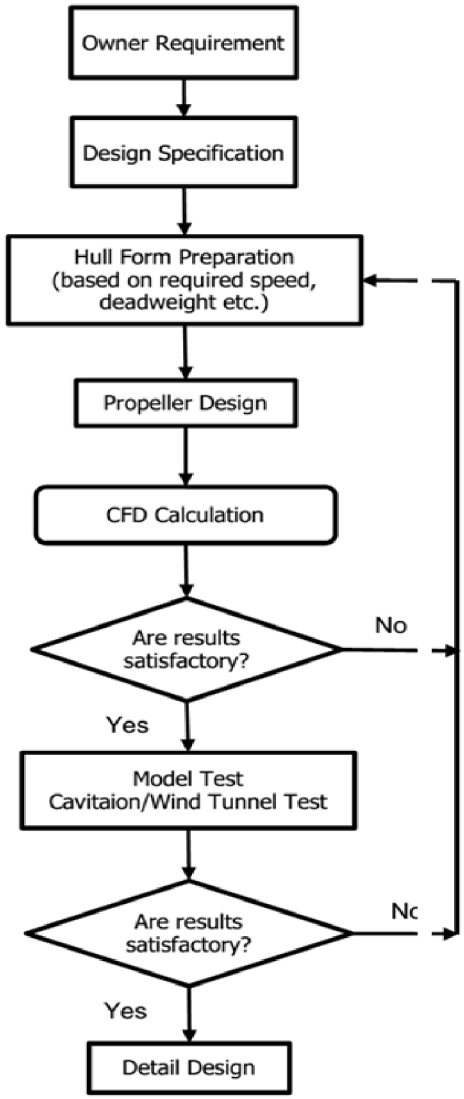

Fig. 3: Design process based on CFD simulation

4. OPEN SOURCE CFD TOOL OpenFOAM

OpenFOAM (Open Field Operation and Manipulation) CFD toolbox is an open source CFD software package written in C++ programming language for the Linux operatingsystem. Anyone can use the code without paying license fees and is allowed to manipulate the source code which is also distributed. The only obligation that comes along with this license is that once a part of code has been used for another project, the resulting code has to be distributed for free under the GNU General Public license as well. OpenFOAM is produced by OpenCFD Ltd. which is sponsored by the ESI Group (the owner of the trademark OpenFOAM) and released under the GNU General Public License version 3.
Pre-processor: OpenFOAM has an in-built blockMesh utility for generating simple meshes of blocks of hexahedral cells andsnappyHexMesh utility for generating complex meshes of hexahedral and split-

hexahedral cells automatically from triangulated surface geometries. The user can generate meshes using other packages and convert them into the format that Open FOAM uses.

Solver: Open FOAM includes over 80 solver applications that simulate specific problems in engineering mechanics. Users can customize the boundary conditions, solver setup or turbulence models according to their need that will work with existing solvers without havingto modify or recompile the existing source code. OpenFOAM has an impressive capability to solve anything from complex fluid flows of naval hydrodynamics or other engineering branches involving chemical reactions, turbulence and heat transfer, to solid dynamics and electromagnetics.

OpenFOAM solvers include[14]:

- Basic CFD solvers
- Incompressible flow with RANS and LES capabilities
- Compressible flow solvers with RANS and LES capabilities
- Buoyancy-driven flow solvers
- DNS and LES
- Multiphase flow solvers
- Particle-tracking solvers
- Solvers for combustion problems
- Solvers for conjugate heat transfer
- Molecular dynamics solvers
- Direct Simulation Monte Carlo solvers
- Electromagnetics solvers
- Solid dynamics solvers

Another distinguishing feature of OpenFOAM is its syntax for tensor operations and partial differential equations that closely resembles the fluid flow governing equations being solved.

The governing equations are so easily expressed in OpenFOAM through the use of object oriented programming and operator overloading, that the users experience flexibility in handling of arbitrary equation sets and can create custom solvers with relative ease.

Post-processor: Paraview is the most common application to post-process OpenFOAM results. It is an open-source, multi-platform data analysis and visualization application with an open, flexible, and intuitive user interface. Other methods of post-processing using third party products are offered, including EnSight, Fieldview and the post-processor supplied with Fluent.

OpenFOAM has a Special Interest Group (SIG) for Ship Hydrodynamics whose objectives are to identify developers and users who are interested in ship hydrodynamics and OpenFOAM, They are working together to develop OpenFOAM exclusively for ship hydrodynamics applications, including pre-processing, solution methods, and post-processing and use OpenFOAM to develop Best Practice Guidelines in ship hydrodynamics.

5. Open FOAM RESULTS OBTAINED BY OTHER RESEARCHERS

OpenFOAM has been found to be capable of solving realistic models of ship flow taking viscous effects into account. Moctaret.al. [15]computed ship resistance and ship motions using OpenFOAM based on the solutions of Reynolds-averaged Navier-Stokes Equations (RaNSE) with finite-volume approach. The calculations were carried out for three benchmark ship types: KRISO Container Ship (KCS), KRISO Very Large Crude Carrier 2 (KVLCC2) and a Naval Destroyer (DTMB 5415). Open source grid generator SnappyHexMesh was used to create numerical grids around the hull. The solvers used in the numerical simulations, known as the “interFoam” solvers, solve the incompressible Navier-Stokes equations using the PISO scheme. They solve for both the water and the air in a domain using a “Volume of Fluid” (VoF) approach to define the interface between the phases. A wide variety of turbulence

models, discretization schemes and other parameters can also be specified.In general the computed resistance and ship motions agree well with the experimental results. Some of the results predicted by Moctaret. al. [16] for KCS at various wave length-ship length ratios, wave amplitude-ship length ratios at various Froude's no. are illustrated in Fig.4 ~ Fig.12. It is seen from Fig.4 ~ Fig.12 that the results predicted by OpenFOAM agree well with experiments.

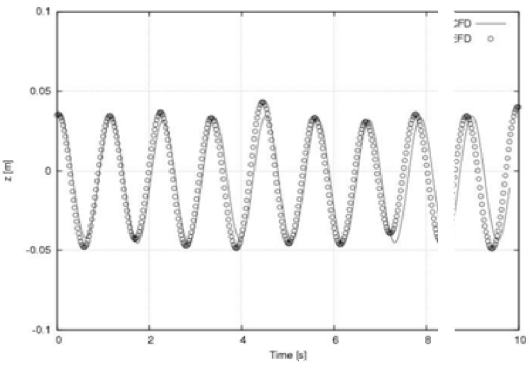

Fig.4: Comparison of time history of heave motion for KCS at F_n=0.26, λ/L=1.15 and ζ/L= 0.01 using numerical method, OpenFOAM by Moctar et. al. [15]

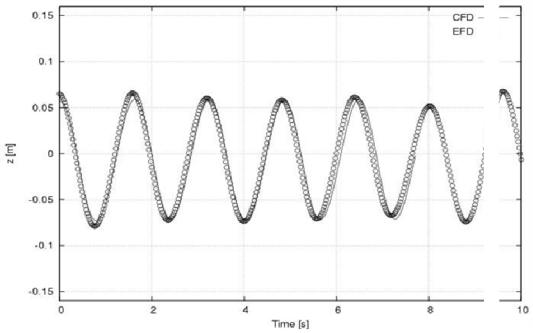

Fig.5: Comparison of time history of heave motion for KCS at F_n=0.26, λ/L=2.00 and ζ/L= 0.0167 using numerical method, OpenFOAM by Moctar et. al. [15]

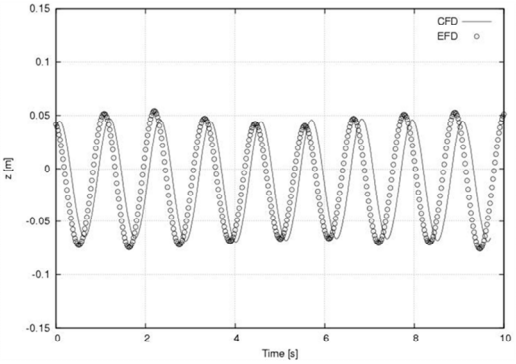

Fig.6: Comparison of time history of heave motion for KCS at F_n=0.33, λ/L=1.33 and ζ/L= 0.0112 using numerical method, OpenFOAM by Moctar et. al. [15]

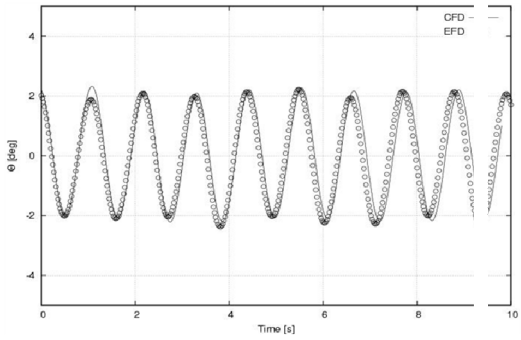

Fig.7: Comparison of time history of pitch motion for KCS at F_n=0.26, λ/L=1.15 and ζ/L= 0.01 using numerical method, OpenFOAM by Moctar et. al. [15]

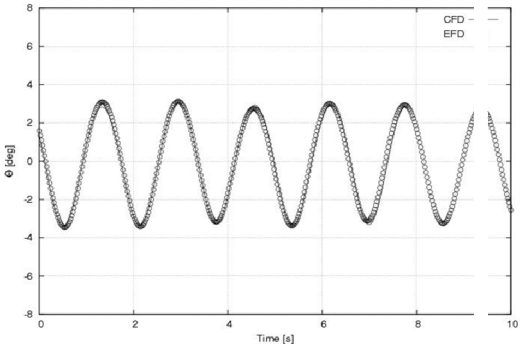

Fig.8: Comparison of time history of pitch motion for KCS at F_n=0.26, λ/L=2.00 and ζ/L= 0.0167 using numerical method, OpenFOAM by Moctar et. al. [15]

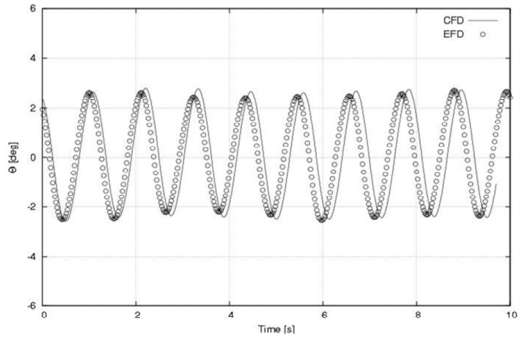

Fig.9: Comparison of time history of pitch motion for KCS at F_n=0.33, λ/L=1.33 and ζ/L= 0.0112 using numerical method, OpenFOAM by Moctar et. al. [15]

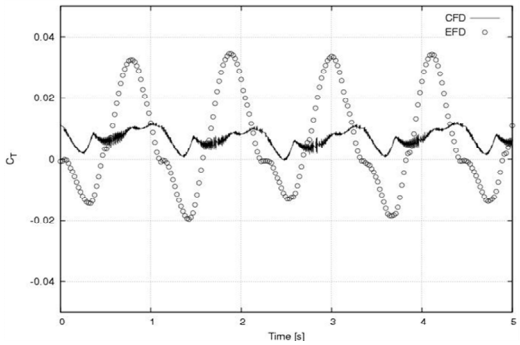

Fig.10:Comparison of time history of total drag for KCS at F_n=0.26, λ/L=1.15 and ζ/L= 0.01 using numerical method, OpenFOAM by Moctar et. al. [15]

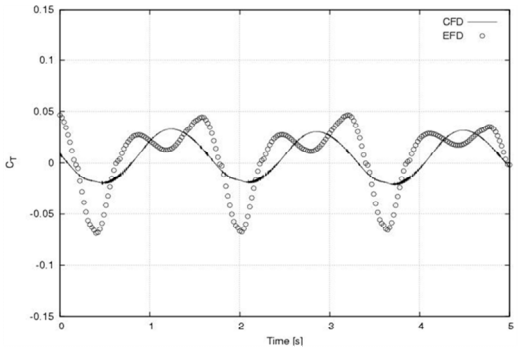

Fig.11:Comparison of time history of total drag for KCS at F_n=0.26, λ/L=2.00 and ζ/L= 0.0167 using numerical method, OpenFOAM by Moctar et. al. [15]

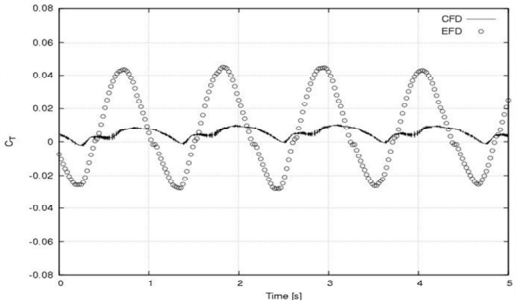

Fig.12:Comparison of time history of total drag for KCS at F_n=0.33, λ/L=1.33 and ζ/L= 0.0112 using numerical method, OpenFOAM by Moctar et. al. [15]

Mordhorst, C. J., [16] carried out an investigation in close collaboration with the Friedrich Lürssen shipyard in Bremen, Germany to find the strength and weaknesses of OpenFOAM in the ship building industry. The yard has specialized in the construction of luxury yachts over 60m and naval vessels over 30m. Different OpenFOAMtutorials for theyard were created mainly to solve aerodynamic and hydrodynamic flow situations around mega yachts. OpenFOAM resultswere also compared to the results of commercial software StarCCM+.It was seen from the investigation that 'interFoam' solver produces good output from a ship hydrodynamic point of view compared to other CFD programs. The wave pattern is very alike compared to StarCCM+although OpenFOAM predicts a little higher wave heights than the commercial solver. When the exhaust flow from the underwater outlet was analyzed, it was seen that interFoamprovides moderate output. The absolute pressure was calculated as expected andit was very similar with both solvers.

STX France S.A.[17] has adopted OpenFOAM software package to compute free surface viscous flows in house for the purpose of developing its hull forms. This solver was used to develop two very close hull forms with the same global ship dimensions and displacement, which were optimized in order to minimize their resistance at 16 and 21 knots respectively.The mesh has been built inSnappyHexMesh. Using the combination of Rhino and Grasshopper, variations of different features of an initial hull forms were generated. Models of both hull forms were built and tested for resistance as well as for self-propulsion with a pair of pods.

The difference between model tests and the resistance computed based on OpenFOAM for both hull form at three different ship speeds was very small at the lower speeds (about 1%) and increased (to about 2%) at the higher speed. This level of accuracy indicates that OpenFOAM may be used for optimization purposes for this type of vessel. Further advantages expected from the use of such a code are the

possibility to optimize the position and shape of appendages such as fins, bilge keels, struts and rudders, thrusters' openings etc.

6. COMPARISON TO A COMMERCIAL SOLVER

There are a large number of commercial CFD packages in the market nowadays including tools for geometry modeling, mesh generation, solving and data visualization. Fig. 13 shows the mostly used commercial and open source Pre-processor, solver and post-processor for ship hydrodynamic analysis. Commercial CFD tools are further compared to open source CFD package OpenFOAM using a concise list of features shown in Table 1.

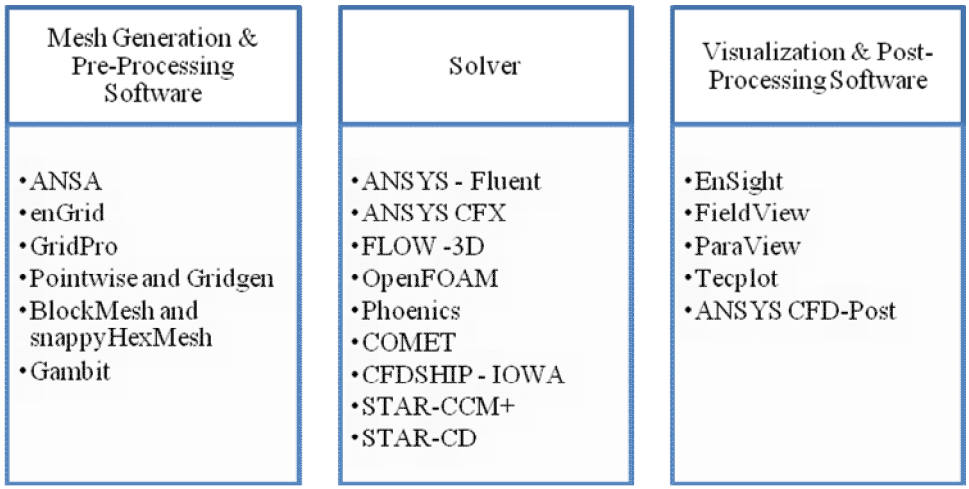

Fig. 13: Commercial and open source CFD softwares (Pre-processor, solver and post-processor).

Table 1: Comparison of OpenFOAM and other Commercial CFD Softwares.

Aspect	**OpenFOAM**	**Commercial Softwares**
Cost	-Free of cost -Source Code available	-Too Expensive -Around £2600-5000 for first year license
Operating System	-Linux	-Windows -Linux
No. of License	-Unlimited	-Additional cost for more than one license
Handling	-Not GUI based. -Requires programming knowledge	-GUI (Graphical User Interface) based
Speed	-Parallel meshing and running	-Parallel running includes additional cost
User Friendliness	-Not much user friendly -Has a steep learning curve	-Excellent -Manuals and tutorials available

Numerical Schemes	-A large number of schemes available to choose from	-Only a few schemes
Customization	-Source code available for users to customize according to their need	-Not possible
Extra Features	-Many but difficult to understand	-Limited functions
Support	-Voluntary support	-Dedicated customer support

7. DISCUSSION

OpenFOAM is rapidly gaining acceptance to a large portion of engineering communities as a free and viable alternative to expensive commercial CFD tools available in the market. Many renowned universities, R & D of renowned shipyards involved in new hull form design are already switching to OpenFOAM due to its accuracy and reliability. As a Computational Fluid Dynamics package it also has a great number of advantages over other CFD softwares making it attractive to the academia as well as the industries.

The increased capacity of ordinary desktop computers provides the opportunity for ship designers in Bangladesh to perform CFD calculations themselves. Compared to the huge expenditure and a great deal of time involved in building and rebuilding several models to obtain the most suitable design, CFD analysis only requires a reliable computing infrastructure and technological know-how, both of which is already available in Bangladesh. Again, costs for a completely open-source system are very low compared to purchasing a dedicated commercial CFD package, with high annual license fees.

Although OpenFOAM requires a very complex process of adjusting and validating starts, before producing some useful results, but if a complete set-up can be established for a specific design problem (such as wave pattern around the hull, full scale resistance calculation) a second similar computation can be run again in couple of hours. There CFD calculations can be conducted in both the earlier phase of the design stage to determine the feasibility of the project and in the final stage to select the hull form with minimal fuel consumption. In regard to the limitations of technological know-how and financial means, OpenFOAM offers a great chance to revolutionize the design processin a developing country like Bangladesh and offers the possibility for innovative out-of-the box concepts for future ships to meet the challenges of the 21st century.

8. CONCLUSION

This paper was aimed at investigating the possibility of the use of open source computational fluid dynamics package in the field of ship design and construction in context of Bangladesh. The maritime industry in Bangladesh is rapidly growing but most of the ship building yards sub-contract the basic drawings to specialized design firms abroad. But in the competitive economy where reducing cost of manufacturing is the only way our yards can get orders from international companies, they may have to reconsider the possibility of producing the designs of ships themselves. Open source CFD tools are a feasible solution in this regard as they offer a great chance to analyze and evaluate ship designs, amongst others to compare hull form variants, or to optimize part of the hull, like the design of the bulbous bow without any additional cost involvement. However, to get useful results from a sophisticated and powerful program like OpenFOAM, a good deal of time and effort is needed from the designers.

REFERENCES

[1] Official Website of OpenFOAM, www.openfoam.com
[2] Alam, Com.M.K., 2004, Bangladesh Maritime Challenges in the 21st Century, PathakShamabesh Publication, Dhaka, pp. 21.

[3] Shipbuilding in Bangladesh, Ministry of Foreign Affairs of Denmark, http://www.bangladoot.se/information%20folder/Shipbuildingpresentation.pdf
[4] Official Webpage of Ananda Shipyard and Slipways Ltd.,http://www.anandashipyard.com
[5] Official Webpage of Western Marine Shipyard Limited (WMShL),http://www.wms.com.bd.
[6] Official Webpage of Khulna Shipyard, http://w3.khulnashipyard.com/
[7] AnbarasanEthirajan,Bangladesh Shipbuilding Goes For Export Growth, http://www.bbc.co.uk/news/business-19315841
[8] Official Webpage of Export Promotion Bureau, Bangladesh, http://www.epb.gov.bd/
[9] http://www.globalsecurity.org/military/world/bangladesh/shipbuilding.htm
[10] N. M. G. Zakaria, K. A. Hossain, M. S. Islam,SWOT Analysis Of Shipbuilding Industries in Bangladesh and Its Challenges to Become Potential Ship-Exporting Nation", Journal of Ship Technology, Vol. 6, No. 2, July 2010, pp 45-57.
[11] http://www.prothom-alo.com/economy/article/51001/
[12] General Shipping Statistics of Bangladesh (2011), No. 21, Department of Shipping Bangladesh, Ministry of Shipping.
[13] http://archive.thedailystar.net/newDesign/news-details.php?nid=229980
[14] Wikipedia Article for OpenFOAM, http://en.wikipedia.org/wiki/OpenFOAM
[15] Moctar, B.; Kaufmann, J.; Oberhagemann, J.; Shigunov, V.; Zorn, T., Prediction of Ship Resistance and Ship Motion Using RANSE, Proceedings of A Workshop on Numerical Ship Hydrodynamics, Vol. 2, pp. 495-505.
[16] Mordhorst, C. J., (2011) Investigation of Open Source CFD Software on Shipyards, Master of Science Thesis, Department of Shipping and Marine Technology, Division of Sustainable Ship Propulsion, Chalmers University of Technology, Göteborg, Sweden.
[17] Cordier, S.; Morand, L.; Roux, J-M, Application of OpenFOAM® To Hull Form Optimisation At STX France s.l. :RINA.

MAGNETOHYDRODYNAMICS MICROPOLAR FLUID FLOW THROUGH A VERTICAL PLATE WITH HALL CURRENT

Nisat Nowroz Anika and Md. Mahmud Alam
Mathematics Discipline, Khulna University, Khulna-9208, Bangladesh.
E-mail: alam_mahmud2000@yahoo.com

ABSTRACT*:* Micropolar fluid flow with heat and mass transfer over a vertical plate under the action of transverse magnetic field has been expedited numerically for the case of usual magnetic field. To obtain the non-similar non-dimensional momentum, energy and concentration equations, the usual non-dimensional transformations have been used. The obtained equations have been solved numerically by explicit finite deference method. The effects of various parameters, entered into the problem, on primary and secondary velocities, angular velocity, temperature and concentration as well as local and average shear Stresses, Couple stress, Nusselt number and Sherwood number are shown in graphically. Finally, a qualitative comparison with previous work has been tabulated.

Keywords: Hall Current, Micropolar Fluid, Heat and Mass Transfer, Finite Difference Method.

1. INTRODUCTION

Micropolar fluids are fluids with microstructure belonging to a class of fluids with nonsymmetrical stress tensor referred to as polar fluids. Physically, they represent fluids consisting of randomly oriented particles suspended in a viscous medium, and they are important to engineers and scientists working with hydrodynamic-fluid problems. Moreover, ionized plasma is partially described by a single-fluid particle approach, where the ion-neutral collision effect has been expressed by Cowling [1] conductivity in the induction equation. In the course of this decade, efforts have been made to extend the Magnetomicropolar phenomena subject to an external magnetic field. The magnetohydrodynamic flow between two parallel plates, known as Hartmann flow, is a classical problem that has many applications in MHD power generators, MHD pumps, accelerators, aerodynamic heating, electrostatic precipitation, polymer technology, petroleum industry, purification of crude oil and fluid droplets and sprays. Under these conditions, the Hall current and Ion-slip are important and they have a mentionable effect on the magnitude and direction of the current density and consequently on the magnetic force term. Free convection flows are studied because of their wide applications and hence it has attracted the attention of numerous investigators. Sattar and Alam [2] presented unsteady free convection and mass transfer flow of a viscous, incompressible and electrically conducting fluid past a moving infinite vertical porous plate with thermal diffusion effect.

The effects of Hall and Ion-slip currents on free convective heat generating flow in a rotating fluid have been studied by Ram [3]**.** The effects of Hall and Ion-slip currents on free convective heat transfer flow past a vertical plate have been investigated by Ferdows et al. [4]. The effects of chemical reaction, Hall and ion-slip currents on the MHD flow of a micropolar fluid through a porous medium have been analyzed by Motsa and Shatey [5] using the successive linearization method.

In this work, our aim is to study the micropolar fluid flow behavior on unsteady viscous incompressible MHD free convection and mass transfer flow past a semi-infinite vertical plate in the presence of Hall currents. The mathematical model has been non-dimensionalized by usual transformation technique and the obtained coupled non similar non linear partial differential equations have been solved by finite difference method. For more accuracy, the stability and convergence test has been taken into account. The results of this investigation are discussed for the different values of the well-known parameters. Afterward, the effects of various parameters on local and average shear Stresses, Couple stress, Nusselt number and Sherwood number are shown graphically. But all figures are not shown for brevity. Finally, the obtained results have been compared with the previous published work.

2. MATHEMATICAL FORMULATION

Consider an unsteady MHD electrically conducting incompressible viscous micropolar fluid flow past over a vertical electrically nonconducting isothermal plate in the presence of traverse magnetic field B_0 in vector form $\mathbf{B} = (0, B_0, 0)$. The fluid flow is also assumed to be in the x -direction which is taken along the plate in the upward direction and y -axis is normal to it. Initially the fluid as well as the plate is at rest and it is considered that the plate as well as the fluid is at the same temperature $T(= T_\infty)$ and concentration level $C(= C_\infty)$. Also it is assumed that the temperature of the plate and spices concentration are raised to $T_w(> T_\infty)$ and $C_w(> C_\infty)$ respectively, which are there after maintained constant, where T_w, C_w are temperature and spices concentration at the wall and T_∞, C_∞ are the temperature and concentration of the species outside the plate respectively. The physical configuration of the problem is furnished in **Fig. 1.**

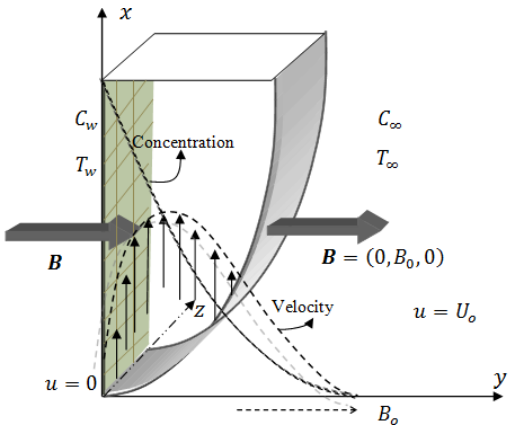

Fig.1: Physical configuration and coordinate system

The magnetic Reynolds number of the flow is taken to be small enough field and the magnetic field is negligible in comparison with applied magnetic field and the magnetic lines are fixed relative to the fluid. Using the relation $\nabla \cdot \mathbf{J} = 0$ for the current density $\mathbf{J} = (J_x, J_y, J_z)$ where $J_y = \text{constant}$. Since the plate is non-conducting, $J_y = 0$ at the plate and hence zero everywhere. The generalized Ohm's law in the absence of electric field to the case of short circuit problem (**Meyer [6] and Cowling [1]**);

$$\mathbf{J} = s\left(\mathbf{q} \times \mathbf{B} + \frac{1}{ne} grad\, p_e \right) - \frac{b_e}{H_0}(\mathbf{J} \times \mathbf{B}) + \frac{b_i b_e}{H_0}(\mathbf{J} \times \mathbf{B}) \times \mathbf{B}$$

where $\sigma, \mu_e, n, e, p_e, \beta_e$ and β_i are the electric conductivity, the magnetic permeability, the number of density of electron, the electric charge, the electron pressure, Hall parameter, and Ion-slip parameter, respectively. If we neglect the electron pressure, we have

$$J_x = \frac{\sigma B_0}{\alpha_e^2 + \beta_e^2}(u\beta_e - w\alpha_e), \quad J_z = \frac{s B_0}{a_e^2 + b_e^2}(wb_e + ua_e)$$

where $a_e = 1 + b_i b_e$

To obtain the governing equations and the boundary condition in dimension less form, the following no-dimensional quantities are introduced as;

$X = \frac{xU_0}{\upsilon}$, $Y = \frac{yU_0}{\upsilon}$, $U = \frac{u}{U_0}$, $V = \frac{v}{U_0}$, $W = \frac{w}{U_0}$, $t = \frac{tU_\infty^2}{u}$, $\Omega = \frac{N\upsilon}{U_0^2}$, $\theta = \frac{T - T_\infty}{T_w - T_\infty}$, $t = \frac{tU_\infty^2}{u}$, and $\Phi = \frac{C - C_\infty}{C_w - C_\infty}$

Using the non-dimensional variables and corresponding boundary conditions the following equations are obtained as:

$$\frac{\partial U}{\partial X} + \frac{\partial U}{\partial Y} = 0 \quad (1)$$

$$\frac{\partial U}{\partial T} + U\frac{\partial U}{\partial X} + V\frac{\partial U}{\partial Y} = (1+\Delta)\left(\frac{\partial^2 U}{\partial Y^2}\right) + D\frac{\partial \Gamma}{\partial Y} + G_r q + G_r^* \Phi - \frac{M}{(\alpha_e^2 + \beta_e^2)}(\alpha_e U + \beta_e W) \quad (2)$$

$$\frac{\partial W}{\partial T} + U\frac{\partial W}{\partial X} + V\frac{\partial W}{\partial Y} = (1+\Delta)\left(\frac{\partial^2 W}{\partial Y^2}\right) + \frac{M}{(\alpha_e^2 + \beta_e^2)}(\beta_e U - \alpha_e W) \quad (3)$$

$$\frac{\partial \Omega}{\partial T} + U\frac{\partial \Omega}{\partial X} + V\frac{\partial \Omega}{\partial Y} = \Lambda\left(\frac{\partial^2 \Omega}{\partial Y^2}\right) - \lambda\left(2\Gamma + \frac{\partial U}{\partial Y}\right) \quad (4)$$

$$\frac{\partial \theta}{\partial T} + U\frac{\partial \theta}{\partial X} + V\frac{\partial \theta}{\partial Y} = \frac{1}{P_r}\left(\frac{\partial^2 \theta}{\partial Y^2}\right) + E_c(1+\Delta)\left(\frac{\partial U}{\partial Y}\right)^2 + \left(\frac{\partial W}{\partial Y}\right)^2 + M\frac{E_c}{(a_e^2 + b_e^2)}(U^2 + W^2) \quad (5)$$

$$\frac{\partial \Phi}{\partial T} + U\frac{\partial \Phi}{\partial X} + V\frac{\partial \Phi}{\partial Y} = \frac{1}{S_c}\left(\frac{\partial^2 \Phi}{\partial Y^2}\right) \quad (6)$$

boundary conditions are;

$$U = 0, V = 0, W = 0, \Omega = -S\frac{\partial U}{\partial Y}, \theta = 1, \Phi = 1 \text{ at } Y = 0 \quad (7)$$

$$U = 0, W = 0, \Omega = 0, \theta \to 0, \Phi \to 1 \text{ as } Y \to \infty$$

where τ represents the dimensionless time, U and V is the dimensionless velocity component in X and Z direction, θ is the dimensionless temperature, Φ is the dimensionless concentration, $\Delta = \frac{\chi}{\rho\upsilon}$ (Microrotation parameter), $G_r = \frac{g\beta(T_w - T_\infty)\upsilon}{U_0^3}$ (Grashof Number), $G_r^* = \frac{g\beta^*(C_w - C_\infty)\upsilon}{U_0^3}$ (Modified Grashof Number), $M = \frac{B_0^2\sigma_e\upsilon}{\rho U_0^2}$ (Magnetic Parameter), $\Lambda = \frac{\gamma}{\rho j\upsilon}$ (Spin Gradient Viscosity), $\lambda = \frac{\chi\upsilon}{\rho j U_0^2}$ (Vortex Viscosity), $P_r = \frac{\rho c_p \upsilon}{\kappa}$ (Prandlt Number), $E_c = \frac{U_o^2}{c_p(T_w - T_\infty)}$ (Eckert Number), $S_c = \frac{u}{D}$ (Schmidt number).

where D is the coefficient of mass diffusivity, β_T is the co-efficient of volumetric expansion for heat transfer, β_C is the co-efficient of volumetric expansion for mass transfer, respectively. And s be an arbitrary constant. When $s = 0$, it has been found that $N = 0$, which represents no-spin condition i.e., the microelements in a concentrated particle flow close to the wall are not able to rotate. The case $s = 1/2$ represents vanishing of the anti-symmetric part of the stress tensor and represents weak concentration. In a fine particle suspension of the particle spin is equal to the fluid velocity at the wall. The case $s=1$ represents turbulent boundary layer flow.

3. SHEAR STRESSES, COUPLE STRESS, NUSSELT NUMBER AND SHERWOOD NUMBER

All The quantities of chief physical interest are shear stress, Nusselt number and Sherwood number. The following equations represent the local and average shear stress at the plate local stress in x-direction,

$t_{xL} = m_0 (\partial u/\partial y)_{y=0}$ and average shear stress in x -direction, $t_{xA} = m_0 \int (\partial u/\partial y)_{y=0} dx$ which are proportional to $(\partial U/\partial Y)_{Y=0}$ and $\int_0^{100} (\partial U/\partial Y)_{Y=0} dX$ respectively. The local Shear stress in z -direction, $t_{zL} = m_0 (\partial w/\partial y)_{y=0}$ and average shear stress in z -direction, $t_{zA} = m_0 \int (\partial w/\partial y)_{y=0} dx$ which are proportional to $(\partial W/\partial Y)_{Y=0}$ and $\int_0^{100} (\partial W/\partial Y)_{Y=0} dX$ respectively. From the Microrotation field, it has been investigated that the effects of various parameters on the local and average couple stress. The following equations represent the local and average couple stress at the wall, local couple stress $M_L = (\upsilon j\rho/g)(\partial N/\partial y)_{y=0}$ and average couple stress $M_A = (\upsilon j\rho/g) \int (\partial N/\partial y)_{y=0} dx$ which are proportional to $((\partial W/\partial Y))_{Y=0}$ and $\int_0^{100} ((\partial W/\partial Y))_{Y=0} dX$ respectively. From the temperature field, it has been investigated the effects of various parameters on the local and average heat transfer coefficients. The following equations represent the local and average heat transfer rate that is well known Nusselt number, local Nusselt number, $N_{uL} = (\partial T/\partial y)_{y=0}$ and average Nusselt number, $N_{uA} = \int (\partial T/\partial y)_{y=0} dx$ which are proportional to $(\partial q/\partial Y)_{Y=0}$ and $\int_0^{100} (\partial q/\partial Y)_{Y=0} dX$ respectively. And from the concentration field, the following equations represent the local and average mass transfer rate that is well known Sherwood number, local Sherwood number, $S_{hL} = (\partial C/\partial y)_{y=0}$ and average Nusselt number, $S_{hA} = \int (\partial C/\partial y)_{y=0} dx$ which are proportional to $(\partial j/\partial Y)_{Y=0}$ and $\int_0^{100} (\partial j/\partial Y)_{Y=0} dX$ respectively.

4. NUMERICAL TECHNIQUE

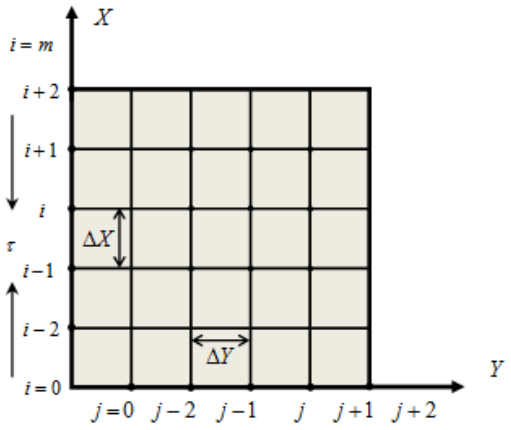

Fig. 2. Explicit finite difference system grid.

In this paper, the governing coupled non similar non-linear partial differential equations with the associated initial and boundary conditions have been solved. From the concept of the above discussion, for simplicity the explicit finite difference method has been used to solve equations (8)-(13) subject to the conditions given by (14). To obtain the difference equations the region of the flow is divided into a grid

or mesh of lines parallel to X and Y axes where X -axis is taken along the plate and Y -axis is normal to the plate. There are $m(=100)$ and $n(=100)$ grid spacing in the X and Y directions respectively as shown in **Fig. 2**. It is assumed that ΔX , ΔY are contant mesh size along X and Y directions respectively and taken as follows, $\Delta X = 1.00(0 \le X \le 100)$ and $\Delta Y = 0.25(0 \le Y \le 25)$ with the smaller time-step, $\Delta\tau = 0.005$.

Let $U', V', W', \Omega', \theta'$ and Φ' denote the values of U, V, W, Ω, θ and ϕ at the end of a time-step respectively. Using the explicit finite difference approximation we have an appropriate set of finite difference equations,

$$\frac{U_{i,j} - U_{i-1,j}}{\Delta X} + \frac{V_{i,j} - V_{i,j-1}}{\Delta Y} = 0 \tag{8}$$

$$\frac{U'_{i,j} - U_{i,j}}{\Delta\tau} + U_{i,j}\frac{U_{i,j} - U_{i-1,j}}{\Delta X} + V_{i,j}\frac{U_{i,j+1} - U_{i,j}}{\Delta Y} = (1+\Delta)\frac{U_{i,j+1} - 2U_{i,j} + U_{i,j-1}}{(\Delta Y)^2} + G_r\theta_{i,j} + \frac{\Gamma_{i,j+1} - \Gamma_{i,j}}{\Delta Y} - \frac{M}{1+m^2}(U_{i,j} + mW_{i,j}) \tag{9}$$

$$\frac{W'_{i,j} - W_{i,j}}{\Delta\tau} + U_{i,j}\frac{W_{i,j} - W_{i-1,j}}{\Delta X} + V_{i,j}\frac{W_{i,j+1} - W_{i,j}}{\Delta Y} = (1+\Delta)\frac{W_{i,j+1} - 2W_{i,j} + W_{i,j-1}}{(\Delta Y)^2} + \frac{M}{1+m^2}(mU_{i,j} - W_{i,j}) \tag{10}$$

$$\frac{\Omega'_{i,j} - \Omega_{i,j}}{\Delta\tau} + U_{i,j}\frac{\Omega_{i,j} - \Omega_{i-1,j}}{\Delta X} + V_{i,j}\frac{\Omega_{i,j+1} - \Omega_{i,j}}{\Delta Y} = \Delta\frac{\Omega_{i,j+1} - 2\Omega_{i,j} + \Omega_{i,j-1}}{(\Delta Y)^2} - \lambda\left(2\Omega_{i,j} + \frac{U_{i,j+1} - U_{i,j}}{\Delta Y}\right) \tag{11}$$

$$\frac{\theta'_{i,j} - \theta_{i,j}}{\Delta\tau} + U_{i,j}\frac{\theta_{i,j} - \theta_{i-1,j}}{\Delta X} + V_{i,j}\frac{\theta_{i,j+1} - \theta_{i,j}}{\Delta Y} = \frac{1}{P_r}\frac{\theta_{i,j+1} - 2\theta_{i,j} + \theta_{i,j-1}}{(\Delta Y)^2} + (1+\Delta)E_c\left(\frac{U_{i,j+1} - U_{i,j}}{\Delta Y}\right)^2 + M\frac{E_c}{\left(a_e^2 + b_e^2\right)}\left(U_{i,j}^2 + W_{i,j}^2\right) \tag{12}$$

$$\frac{\Phi'_{i,j} - \Phi_{i,j}}{\Delta\tau} + U_{i,j}\frac{\Phi_{i,j} - \Phi_{i-1,j}}{\Delta X} + V_{i,j}\frac{\Phi_{i,j+1} - \Phi_{i,j}}{\Delta Y} = \frac{1}{S_c}\frac{\Phi_{i,j+1} - 2\Phi_{i,j} + \Phi_{i,j-1}}{(\Delta Y)^2} \tag{13}$$

with the boundary conditions;

$$U^n_{i,0} = 0, W^n_{i,0} = 0, \Omega^n_{i,0} = -s\frac{U^n_{i,1} - U^n_{i,0}}{\Delta Y}, \theta^n_{i,0} = 1, \Phi^n_{i,0} = 1 \tag{14}$$

$U^n_{i,L} = 0, W^n_{i,L} = 0, \Omega^n_{i,L} = 0, \theta^n_{i,L} = 0, \Phi^n_{i,L} = 1$ where, $L \to \infty$

Here the subscript i and j designates the grid points with X and Y coordinates respectively and the superscript n represents a value of time, $\tau = n\Delta\tau$ where $n = 0, 1, 2, \ldots\ldots$. The primary velocity (U) , secondary velocity (W) , Microrotation (Ω) , temperature (θ) and concentration (Φ) distributions at all interior nodal points may be computed by successive applications of the above finite difference equations. The numerical values of the local shear stresses, local couple stress, local Nusselt number and local Sherwood number are evaluated by **Five-point** approximate formula for the derivatives and then the average Shear Stress, Couple stress, Nusselt number and Sherwood number are calculated by the use of the **Simpson's** 1/3 integration formula. The stability conditions and the convergence criteria are not shown for brevity.

5. RESULT AND DISCUSSION

In order to get the Physical significance of the model, the approximate solutions are obtained for various parameters with moderate values of Eckert number E_c. With the above mentioned parameters, the Local and average shear stress for x-direction and z-direction, respectively, Couple Stress, Nusselt number and

Sherwood number have been discussed. To get the steady state solutions, the computations have been carried out up to dimensionless time $\tau = 80$. Fig. 3 shows the effects of Magnetic parameter M on the local Shear stress in the x-direction. This figure depicts that an increase in the magnetic parameter leads to a decrease in the profiles. The effects of M on the Local Shear stress in z-direction has been shown in Fig. 4. It is observed from the figure, t_{zL} has exactly opposite characteristic as compared to t_{xL} with the increase of magnetic parameter. t_{zL} , on the other hand, shows the increasing effect with the increase of Hall parameter b_e has been illustrated in Fig. 5. In Fig. 6; situation arises for different values vortex viscosity λ. Only the local couple stress has presented the significant change where the other profile remains unchanged. Local couple stress has decreases with the increasing values of λ as shown in Fig. 6. Fig. 7 illustrated that the different pattern with the different values of spin gradient viscosity L . In Fig. 7, couple stress showed the increasing effects with the increase of L where the others have no visible changes. Side by side, Figs. 8-9 each shows the average effect on shear stresses, which is analogous with the change of local stresses for different values of magnetic parameter M. These graphs depict that the main flow decreased with the magnetic parameter M . As noted that the boundary layer flow attains minimum velocity values for large Hartmann number. The application of a transverse magnetic field to an electrically conducting fluid flow gives rise to a resistive type of force called Lorenz force.

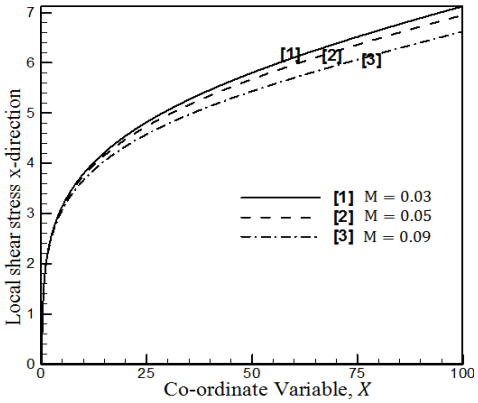

Fig. 3: Local Shear stress τ_{xL} for different values of Magnetic parameter M .

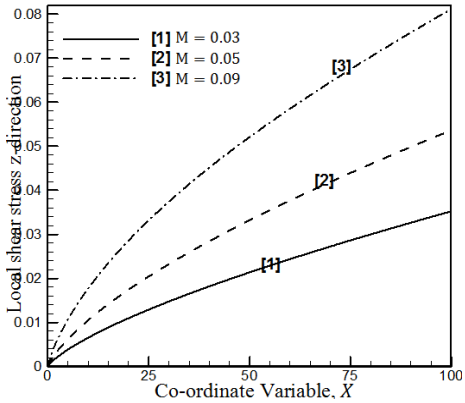

Fig. 4: Local Shear stress τ_{zL} for different values of Magnetic parameter M .

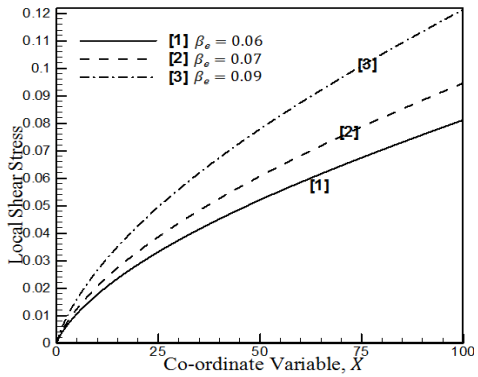

Fig. 5: Local Shear Stress τ_{zL} for different values of dimensionless Hall parameter b_e .

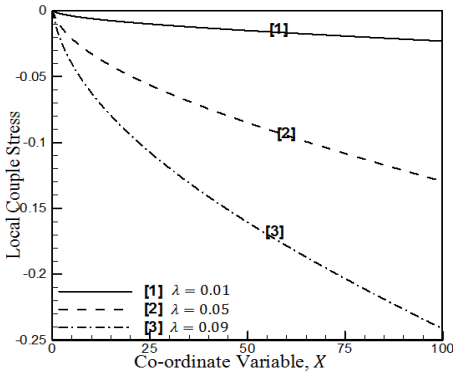

Fig. 6: Local Couple Stress for different values of dimensionless Vortex Viscosity λ

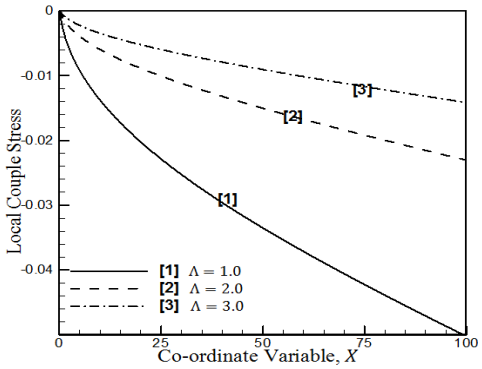

Fig. 7: Local Shear Stress in x-direction for dimensionless Spin gradient viscosity Λ.

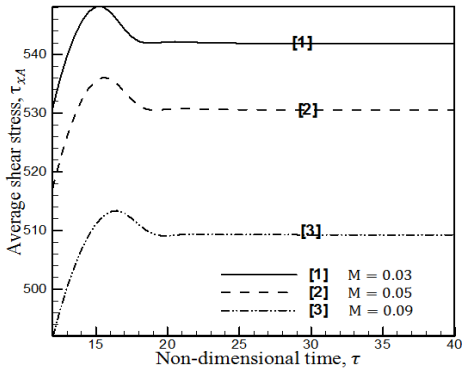

Fig.8: Average Shear stress τ_{xA} for different values of dimensionless Magnetic parameter M

This type of force has a tendency to slow down the motion of the stream velocity of the boundary layer. In Fig.9 the physical insight of the influence of magnetic field M on the average shear stress in z-direction has been expedited. Fig. 10 shows the increasing effects on average shear stress t_{zA} with respect to dimensionless time τ for increasing parameter values b_e. In the Fig.11, the average couple stress M_A has a decreasing effect which is more prominent with the increase of vortex viscosity l . From Fig.12, it has also evident that, average couple stress M_A increases with the increase of Spin gradient viscosity L .

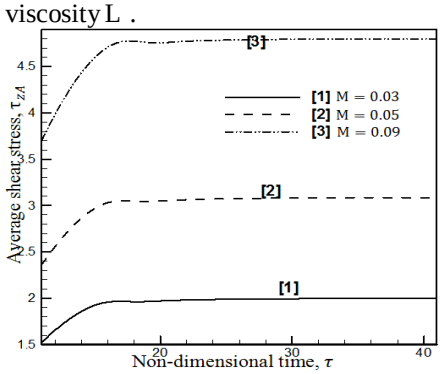

Fig. 9: Average Shear stress τ_{zA} for different values of dimensionless Magnetic parameter M

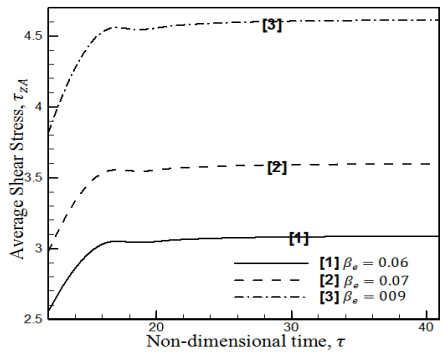

Fig.10: Average Shear Stress τ_{zA} for different values of dimensionless Hall parameter b_e .

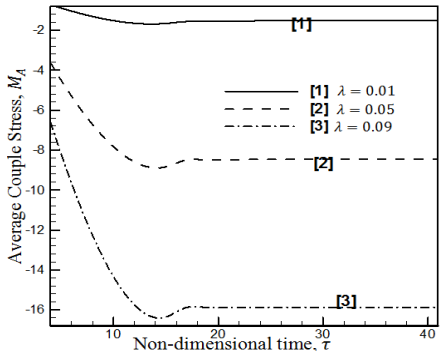

Fig.11: Average Couple Stress for different values of dimensionless Vortex Viscosity l .

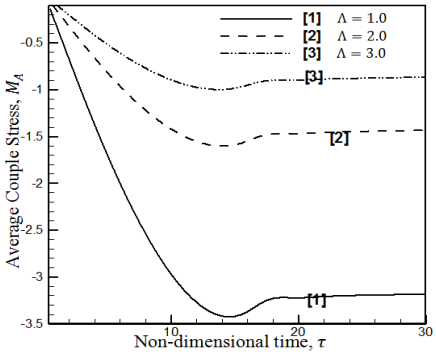

Fig.12. Average Couple Stress for dimensionless Spin gradient viscosity L .

6. CONCLUSION AND COMPARISON

The results are discussed for different values of important parameters as Magnetic parameter, Vortex viscosity, Spin gradient Viscosity and Hall current. Our aim is to study the effects of Hall and Ion-slip current with mass and heat flux which has been of interest to the engineering community and to the investigation dealing with the problem in many industrial applications. The important findings of this model are very effective for any kind of change of parameters. The allover investigations considered graphically are listed as, local and average shear stresses decreases with the increase of M .

On the contrary, shear stresses in z-direction increases with same values of and couple stresses increases with the increase of b_e . Local and average couple stresses decreases as vortex viscosity increases. Spin gradient viscosity, on the other hand, causes increasing effects for the decreasing vaules of vortex viscosity. The physical properties have been discussed graphically for various values of corresponding parameters and compared the present framework results with **S. S. Mosta, and S. Shateyi** [5]. The accuracy of present work is qualitatively good in case of all the flow parameters.

REFERENCES

[1] T. G. Cowling, Magnetohydrodynamics, Interscience Publications, New York **(1957).**
[2] M. A. Sattar, and M. M. Alam,Thermal Diffusion as well as transpiration effects on MHD free convection and mass transfer flow past an accelerated vertical porous plate, Indian Journal of pure applied Mathematics **(1994)**, Vol. 25(6), pp. 679-688.
[3]P. A. M. Ram, The Effec Hall and Ion-Slip Current on Free Convection Heat Generating Flow in a Rotating Fluid, International journal of Energy Research **(1995)**, Vol. 19(5), pp. 371-376.
[4]M. Ferdows, Esrat Jahan , M. A. A. Hamad, and Masahiro OTA, Effects of Hall and ion-slip currents on free convective heat transfer flow past a vertical plate considering slip conditions, Canadian Journal of Science and Engineering Mathematics **(2011)**, Vol. 2(2), pp. 70-76.
[5]S. S. Mosta, and S. Shateyi, The effects of chemical Reaction, Hall and Ion-slip currents on MHD Micropolar Fluid Flow with Thermal Diffusivity using a Novel Numerical Technique, Journal of Applied Mathematics **(2011)**, ID 689015, pp. 30.
[6] R. C. Meyer, Effects of Hall current and rotation, J. Aerospace Sci. **(1958)**, Vol. 25**,** pp. 561.

DESIGN AND NUMERICAL ANALYSIS OF A VERTICAL AXIS WIND TURBINE FOR LOW WIND VELOCITY

[1]Md. RashedulHasan, [2]G.M HasanShahariar, [*3]Md. Ashraful Islam
shihabkuet09@gmail.com, rashedulhasan47@hotmail.com, ashraf.bitr@gmail.com
[1, 2,3]Departmentof Mechanical Engineering, Khulna University of Engineering & Technology, Khulna-9203, Bangladesh

ABSTRACT: A model for the aerodynamic evaluation of a vertical-axis wind turbine (VAWT) to improve its torque characteristics has been analyzed. The three-bladed vertical axis wind turbine is more promising especially in areas with frequent light winds. This paper presents a numerical analysis of the aerodynamics performance on the Darreius blade (egg-beater type) fixed pitch vertical axis wind turbine based on the NACA 0012 airfoil. The solid modeling software SolidWorks is adopted for the modeling of the rotor blade. Another CFD software ANSYS FLUENT is used for the investigation of 2D Computational Fluid Dynamics (CFD) for the calculation of rotor performance. ANSYS software is used to create 2D model of the turbine and the mesh. The model and mesh generated into Fluent for numerical iterate solution. The Reynolds averaged Navier-Stokes solver is used for the investigation of general effects on the performance of several geometry characteristics of two-dimensional airfoils. The RNG k-ε model is adopted for the turbulence closure. Flow field characteristics are also investigated for a constant free stream velocity for 9 m/s. This study shows the results of the power co-efficient (C_P) for different angle of attack.

Keywords: Vertical axis wind turbine, Aerodynamics, CFD, Airfoil, Darrieus rotor

1. INTRODUCTION

Sustainable energy is a promising source of energy for the future generation, because the earth's natural source of energy is getting lower & lower day by day due to the high usage of energy. Wind is one of the main source of sustainable energy. Wind turbine uses natural wind to produce sustainable energy, where mechanical energy is converted to electrical energy by means of generator. This can contribute to minimize the power problem of Bangladesh. This research focuses on the study of vertical axis wind turbine (Darrieus type).

There are two types of modern wind turbines, namely Horizontal Axis Wind Turbines (HAWTs) and Vertical Axis Wind Turbines (VAWTs). Horizontal axis wind turbine is popular for large scale power generation, while verticalaxis wind turbine is utilized for small scale power generation [1, 2]. The principal advantages of the vertical axis forms are their ability to accept wind from any direction without yawing. The absence of yaw system simplifies the design of the turbine. Blades of VAWT are uniform section and untwisted, which makes them relatively easy to fabricate. Furthermore, almost all of the components requiring maintenance are located at ground level facilitating the maintenance work appreciably. But, its high torque fluctuations with each revolution, no self-starting capability are the drawbacks [3,4]

Many factors play a role in the design of a wind turbine rotor, including aerodynamics, generator characteristics, blade strength and rigidity, noise levels. But for a small wind energy conversion system's success is largely dependent on maximizing its energy extraction , rotor aerodynamics play a critical role in the minimization of the cost of energy [5 paper3].We have used NACA 0012 airfoil for the blade design. A largely used system to improve the aerodynamics of wind turbines is the utilization of computational fluid dynamics (CFD), which is less expensive than experimental tests and saves a lot of time and work. Also it permits the knowledge of the entire flow field. The VAWT has an inherent unsteady aerodynamic behavior due to the variation of the angle of attack with the azimuthal position, of the relative velocity and of Reynolds number. The phenomenon of dynamic stall is then an intrinsic effect of the operation of this kind of turbine, having a significant impact in loads and power. The complexity of the unsteady aerodynamics of a VAWT requires an accurate selection of the appropriate turbulence model. Here we have used RNG k-ε method for our 2D computations.

2. PHYSICAL MODEL

The main objective of this work is the numerical simulation of the aerodynamic behavior of a three-bladed Darrieusvertical axis wind turbine characterized by the use of the NACA 0012 airfoil. Table I displays the geometrical and kinematic features of the tested rotor.

Table 1. Main geometrical features of the analyzed rotor

Blade profile	NACA 0012
No. of blade, N	3
Rotor height, H	1200mm
Rotor diameter, D	1500mm
Chord length, c	85.5mm
Solidity, σ	0.342
Aspect ratio(H/D)	1.25

A complete CAD procedure to model a Darrieus type vertical-axis wind turbine was presented, in order to generatean easily meshable geometry to be adopted for CFD. Figure 1(a) represents a physical model for vertical axis wind turbine and figure 1(b) represents the blade section.[5]

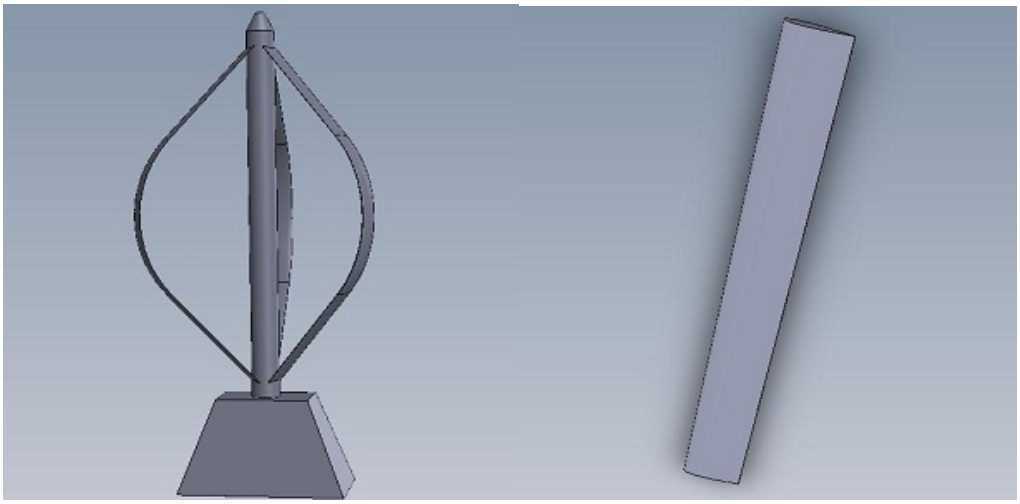

(a) (b)

Fig 1: Geometrical figure of Darrieus type VAWT

3. AERODYNAMICS OF VERTICAL AXIS WIND TURBINE

A vertical axis wind turbine is called a Darrieus turbine when it is driven by aerodynamic lift. From the perspective of the blade, the rotational movement of the blade generates a head wind that combines with the actual wind to form the apparent wind. If the angle of attack of this apparent wind on the blade is larger than zero, the lift force has a forward component that propels the turbine. However, The Darrieus type vawt is not self-starting[6].

As can be seen from the Figure 4 the relative velocity, w can be obtained from the cordial velocity component and normal velocity component:

$$w = \sqrt{(usin\theta)^2 + (ucos\theta + \omega r)^2}$$

Where, u is the induced velocity through the rotor, ω is the rotational velocity, R is the radius of the turbine, and □ is the azimuth angle. The angle of attack express as:

$$\alpha = tan^{-1} \left(\frac{usin\theta}{ucos\theta + \omega r}\right)$$

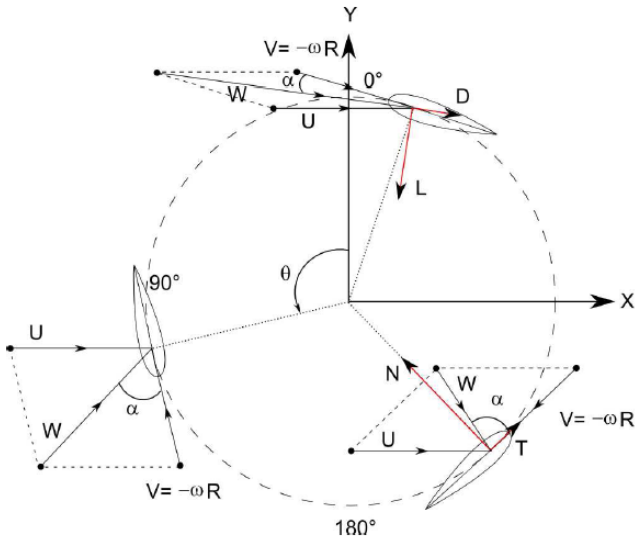

Fig 2: Forces on rotor blade

The normal and tangential force coefficients can be expressed as:

$$C_n = C_L cos\alpha + C_D sin\alpha$$
$$C_t = C_L cos\alpha - C_D sin\alpha$$

Where,*CL* is the lift coefficient and *CD* is the drag coefficient for angle of attack α. Then the normal and tangential forces for single blade at a single azimuthal location are:

$$F_N = \left(\frac{1}{2}\right) \rho\omega^2 (hc) C_N$$
$$F_T = \left(\frac{1}{2}\right) \rho\omega^2 (hc) C_t$$

Where,'h' is the blade height and 'c' is the blade chord length. The force of the wind on the turbine experienced byone blade element in the direction of the airflow is:

$$T_i = F_T cos\theta - F_N sin\theta$$

The power co-efficient (C_P) is expressed as:

$$C_P = \left(\frac{1}{2}\right) \rho A U^3$$

The Reynolds number(Re) and tip speed ratio(λ) are expressed as:

$$Re = \left(\frac{\rho U c}{\mu}\right)$$
$$\lambda = \left(\frac{\omega R}{U}\right)$$

4. DESCRIPTION OF NUMERICAL FLOW FIELD

For the numerical analysis of vawt, ANSYS Fluent software is used to create 2D model of the turbine and the mesh. In Ansysmesh were generated a total of 27584 nodes and 53807 elements. The RANS equation were solved and RNG k-ε method was adopted for the turbulence closure. The proposed numerical simulations aim to represent a turbine operating in open field conditions. Inlet has been set as a velocity inlet, with a constant wind velocity profile of 9 m/s, while outlet has been set as a pressure outlet. Two symmetry boundary conditions have been used for the two side walls. To ensure the continuity of the flow field, the circumference around the circular opening, centered on the turbine rotational axis, was set as an interface[6].

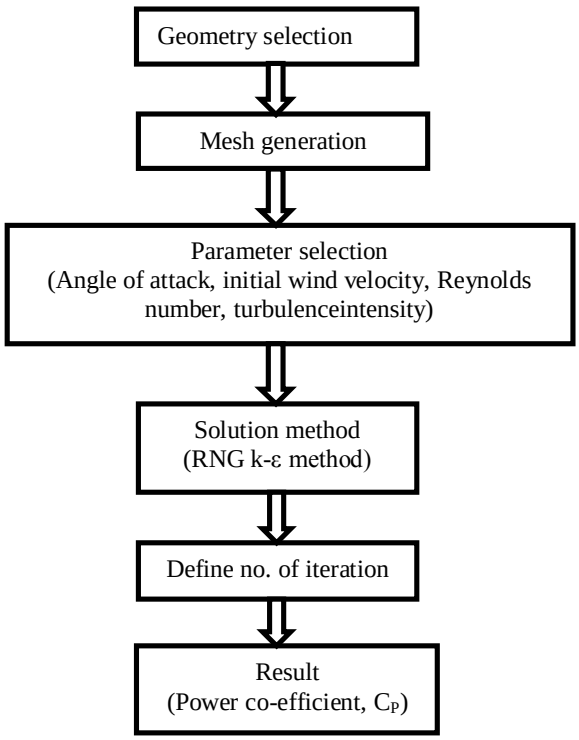

Fig 3: Flow chart of iterative procedure

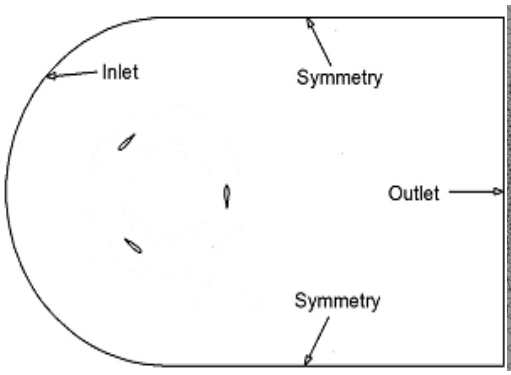

Fig 4: Boundary conditions

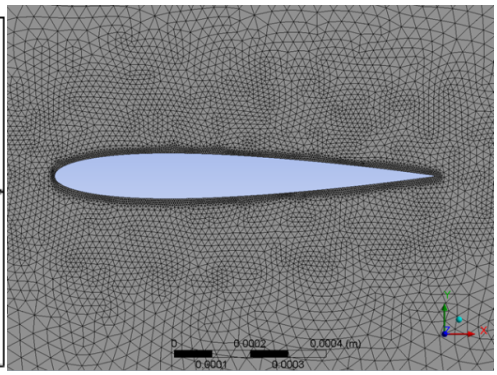

Fig 5: Close up of the grid around the NACA 0021 airfoil

5. Result:

The power co-efficient(C_P) has been computed using CFD analysis. The angle of attack was set for 10^0, backflow turbulent intensity was 1 percent and backflow turbulent viscosity ratio 10 percent for velocity inlet. Fluid material has been chosen for air and blade material for aluminium. The blade pressures are computed from the solution of RANS equations through the integration of the pressure and shear stress over the blade surfaces. CFD can capture flow features such as vortex/blade interaction and vortex shedding into the wake. For this criteria, the following result is given below.

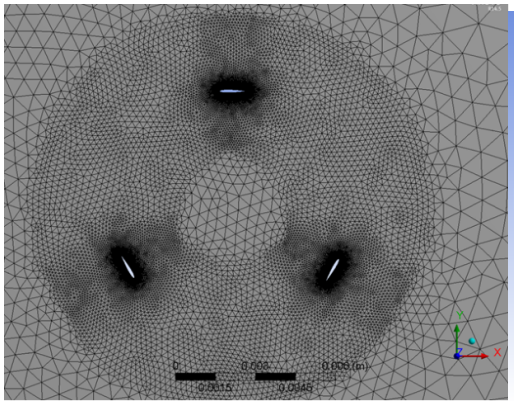

Fig 6: Sub-grid mesh for a three-bladed VAWT

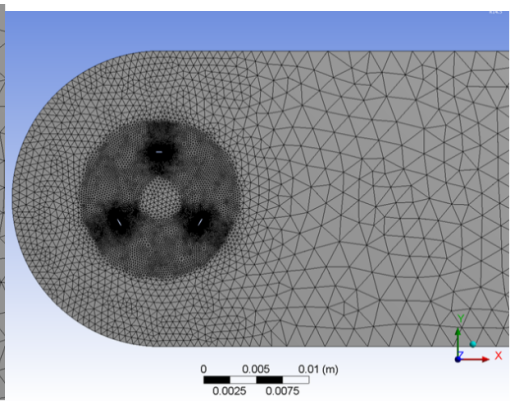

Fig 7: Mesh of the 2D model

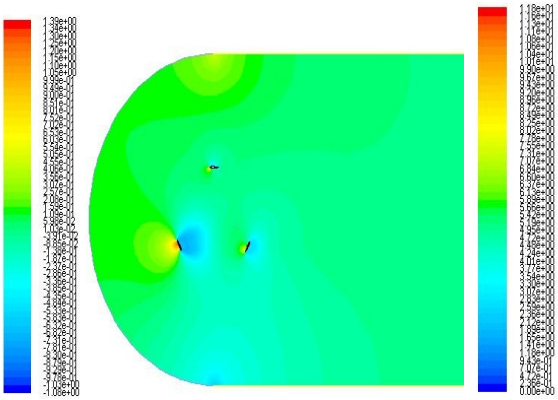

Fig 8: Contours of power co-efficient

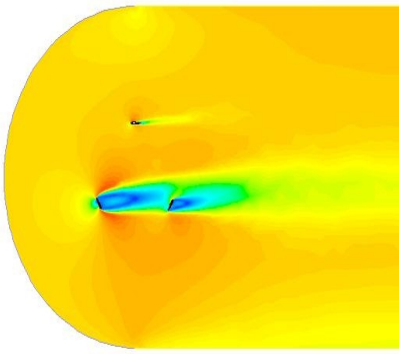

Fig 9: Contours for velocity magnitude

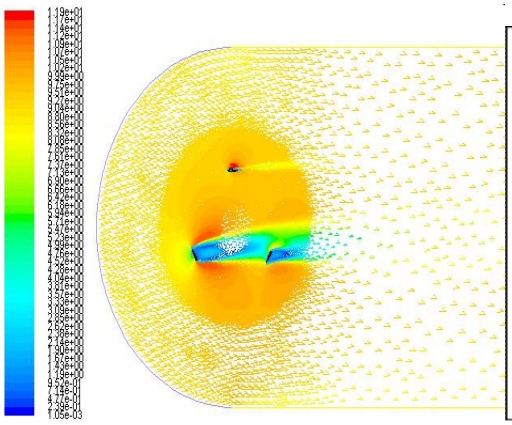

Fig 10: Contours of velocity vector

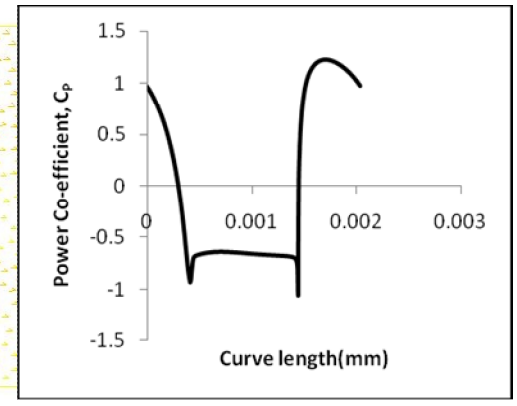

Fig 11: Pressure co-efficient at $\alpha=10^0$

6. CONCLUSION

In this paper, numerical investigation of 2D Darrieus type vertical axis turbine for NACA 0012 airfoil has been analyzed. The power co-efficient has been calculated by using CFD analysis.

i. There have some negative value in the power co-efficient vs curve length for angle of attack 10^0.
ii. For the future work, it has to be analyzed power co-efficient(C_P) for different angle of attack at different azimuthal position to obtain a better result.

iii. The co-efficient of torque(C_T) at different tip speed ratio has to be determined to make the vawt at better performance.

7. NOMENCLATURE

c=Chord, m
$C_{L=}$Lift coefficient
C_D=Drag coefficient
C_n=Normal force coefficient
C_t=Tangential force coefficient
C_p=Power coefficient
F_n=Normal force, N
F_t=Tangential force, N
H=Height of rotor, m
N=Number of blades
R=Rotor radius, m
U=Wind velocity on the blade, m/s
A= Angle of attack (AOA), rad
θ =Azimuthal angle, rad
λ= Tip-speed ratio (TSR)
ρ=Air density (293.6 K), 1.225 kg/m3
μ= Air viscosity (293.6 K), 1.81*10^(−5)Pa s
ω= Rotor angular speed, rad/s

REFERENCES

[1] S. Li, Y. Li, Numerical study on the performance effects of solidity on the straight-bladed vertical axes wind turbine, Power and energy Engineering Conference, 2010.
[2] I.Paraschivoiu, "Wind turbine design with emphasis on Darrieus concept", Polytechnic International Press, Canada,2002.
[3] Sathyajith, M. "Wind Energy Fundamentals,Resource Analysis and Economics", Springer-VerlagBerlin Heidelberg, Netherlands, 2006.
[4] Claessens, M.C."The Design and Testing of Airfoils for Application in Small Vertical Axis Wind Turbines", Delft University, November 2009.
[5] Marco RacitiCastelli, Stefano De Betta and Ernesto Benini," Three-Dimensional Modeling of a Twisted-Blade Darrieus Vertical-Axis Wind Turbine", World Academy of Science, Engineering and Technology 78 2013
[6] AsressMulugetaBiadgo, AleksandarSimonovic, DraganKomarov, Slobodan Stupar, "Numerical and Analytical Investigation of Vertical Axis Wind Turbine", Faculty of Mechanical Engineering, Belgrade, December 2012

FORCED CONVECTION THROUGH NANOFLUID-BASED DIRECT ABSORPTION SOLAR COLLECTOR

Salma Parvin*, Rehena Nasrin and M.A. Alim
Department of Mathematics, Bangladesh University of Engineering and Technology, Dhaka-1000, Bangladesh
*E-mail- salpar@math.buet.ac.bd

ABSTRACT: A numerical investigation is done for the heat transfer performance and entropy generation of forced convection through a direct absorption solar collector. The working fluid is Cu-water nanofluid. The simulations focus specifically on the effect of forced convective parameter Reynolds number on the mean Nusselt number, total entropy generation, Bejan number and collector efficiency. Also Isotherms, heat function and entropy generation are presented for various Reynolds number. The governing partial differential equations are solved using penalty finite element method with Galerkins weighted residual technique. The results show that both the mean Nusselt number and the total entropy generation increase as the inertia force of nanofluid. Overall, the results presented in this study provide a useful source of reference for enhancing the force convection heat transfer performance while simultaneously reducing the entropy generation.

Keywords: Forced convection, direct absorption solar collector, finite element method, nanofluid, entropy generation

1. INTRODUCTION

The conversion of solar energy into heat is done with the help of solar collectors. Most commonly used collectors are simple in construction and are flat plate type collectors. New classes of collectors which are used to increase the efficiency of the collectors are direct absorption solar collector (DASC) [1]. The DASC's were firstly proposed in the mid 1970's but the major problem faced by these collectors was the poor absorption properties of conventional fluids used in these collectors. By the development of new class of fluids known as nanofluids [3] which show improved properties over the conventional fluids, these type of collectors can gain importance. In conventional type of flat plate solar collectors they are encountered with three resistances whereas in case of direct absorption type solar collector (DASC), these three resistances are reduced to one. The major problem associated with conventional collectors using micro or millimeter sized particles is their rapid settling. These problems were least observed with the nanofluids. Based on DASC, the attempt had been made to investigate the variation in collector efficiency using nanofluids [3-5]. Heat transfer enhancement in solar devices is one of the key issues of energy saving and compact designs. The problem of heat loss, collector efficiency in various solar collectors [6-9] filled with traditional fluid as well as different nanofluids have attracted significant attention in recent years.

All thermofluidic processes involve irreversibilities and therefore incur an efficiency loss. In practice, the extent of these irreversibilities can be measured by the entropy generation rate. In designing practical systems, it is desirable to minimize the rate of entropy generation so as to maximize the available energy [10-11]. Overall, the results have shown that the rate of entropy generation increases as the irreversibility distribution ratio increase. Moreover, for given values of the irreversibility distribution ratio, the entropy generation rate is determined by the heat transfer irreversibility and / or fluid friction irreversibility. Specifically, Cho et al. [12] investigated the natural convection heat transfer performance and entropy generation rate in a water-based nanofluid-filled cavity bounded by a left wavy-wall with a constant heat flux, a right wavy-wall with a constant low temperature, and flat upper and lower walls with adiabatic conditions. The results showed that the mean Nusselt number increased and the entropy generation rate decreased as the volume fraction of nanoparticles increased. In addition, the heat transfer effect and entropy generation rate were shown to depend on the type of nanoparticles used. Heat recovery from hot fluids in material processing industries is important for environmental and thermal management. The ‘heatline’ method of visualizing the true path of convection heat transfer was studied in refs. [13-14]. It

was developed as the convection counterpart (or the generalization) of the technique of heat flux lines used routinely in heat conduction.

In the light of above discussions, it is seen that there has been a good number of works in the field of heat loss system through a direct-absorption solar collector. In spite of that there is some scope to work with fluid flow, heat loss, entropy generation and enhancement of collector efficiency using nanofluid. The effects of the Reynolds number on the isotherm distribution, heatlines, mean Nusselt number, rate of entropy generation, collector efficiency and Bejan number are shown graphically in the present study.

2. PROBLEM FORMULATION

2.1 DIMENSIONS OF DIRECT ABSORPTION SOLAR COLLECTOR

The Dimensions of the collector are chosen to increase the absorption of solar energy with the minimum requirement of the nanofluids. The effective area of the absorber plate is 240×240 mm and the total area of the collector including wooden box is 300×300 mm. The absorber plate was painted black in order to increase it's absorption properties. In order to minimize the losses glass wool and thermocol insulation are provided at the side's walls and at the bottom. Outer casing of the collector is made of wood. The glazing is used as low reflectance glass with transmittance percentage of about 90%. The absorber plate is black painted copper plate and the size of collector is kept small in order to reduce the use of nanofluids.

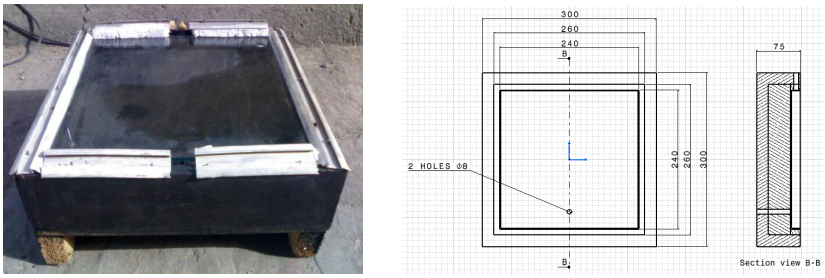

(a) (b)

Fig. 1: (a) Actual view and (b) Dimensions of Direct Absorption Solar Collector

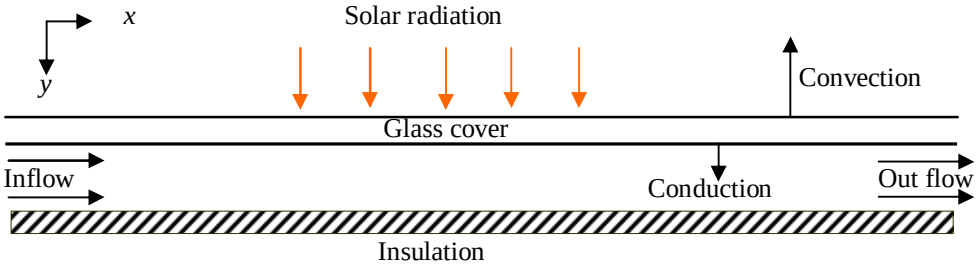

Fig. 2: Schematic diagram of the DASC

Figs. 1 shows the actual view and cross section of a DASC. The schematic of the nanofluid-based direct absorption solar collector is shown in Fig. 2. The fluid is contained within the enclosed space of the DASC. A two-dimensional heat transfer analysis is developed in which direct sunlight is incident on a thin flowing film of nanofluid into a DASC with surface area, length and height of A, L and H respectively. The fluid through the collector is water-based nanofluid containing Cu nanoparticles enters with temperature T_i from left inlet and exits from right port. The thermo-physical properties of the nanoparticle are taken from ogut [15]. The bottom wall is considered to be adiabatic, i.e., no heat flux is allowed to pass through it. The fluid is enclosed at the top by a glass surface, which allows most of the incident solar flux to pass through. This top surface is assumed to be exposed to the ambient atmosphere and thus loses heat by convection.

2.2 MATHEMATICAL MODELING

The incident radiation is considered to be the incoming solar radiation. For the study of the principal behavior of the nanofluid based DASC, atmospheric absorption was neglected in these calculations. Hence, the incident solar intensity is calculated using the blackbody relation given by Eq. (1), where the value of T_{solar} is taken as 5800 K:

$$I_{b\lambda}\left(\lambda, T_{solar}\right) = \frac{2hc_0^2}{\lambda^5\left[\exp\left(\frac{hc_0}{\lambda k_B T_{solar}}\right) - 1\right]} \tag{1}$$

In this equation h is Planck's constant, k_B is the Boltzmann constant, c_o is the speed of light in vacuum, and λ is the wavelength. Using this relation the spectral intensity incident on the solar collector is evaluated. The radiation intensity within the fluid is assumed to vary only in one dimension (along the *y*-direction). Equation (2) is the radiative transport equation, which is used in this model. The right side of the equation determines the attenuation in the intensity as the radiation travels through the fluid

$$\frac{\partial I_\lambda}{\partial y} = -\left(K_{a\lambda} + K_{s\lambda}\right)\tau I_\lambda = -K_{e\lambda}\tau I_\lambda \tag{2}$$

where τ is emissivity of glass cover, $K_{a\lambda}$ is the spectral absorption coefficient, and $K_{s\lambda}$ the spectral scattering coefficient. Taken together they can also be represented as $K_{e\lambda}$, the spectral extinction coefficient. Also, in order to keep the model simple, the effect of in-scattering has not been considered. As will be described later in Eqs. (7)–(7b), the scattering efficiency varies as the fourth power of particle size, and the absorption efficiency varies almost linearly with the particle size, therefore, this simplification is justified for calculations involving nanoscale particles. For pure fluids, scattering can be neglected and only the attenuation caused by absorption may be considered. For that case, the spectral absorption coefficient can be calculated using Eq. (3)

$$K_{a\lambda} = \frac{4\pi\kappa}{\lambda} \tag{3}$$

where κ is the index of absorption. However, for nanofluids, where the presence of small particles influences the nature of absorption, as well as scattering, some complex relationships need to be used. Since in the present problem the particles have a mean diameter of about 5 nm, the approximation of Rayleigh scattering [16] can be applied. This approximation is valid when $\alpha \ll 1$ and $m|\alpha| \ll 1$, where α is defined as the size parameter and is given by

$$\alpha = \frac{\pi D}{\lambda} \tag{4}$$

where *D* is the diameter of the particles, and $m\left(= n + i\kappa\right)$ is defined as the normalized refractive index of the particles

$$m = \frac{m_{particles}}{n_{fluid}} \tag{5}$$

In physical terms, Rayleigh scattering can be understood as the regime in which the particle size is much smaller than the wavelength of the incident radiation. In general, the extinction coefficient can be given as

$$K_{e\lambda} = \frac{3\phi Q_{e\lambda}\left(\alpha, m\right)}{D} \tag{6}$$

where ϕ is the particle volume fraction, and $Q_{e\lambda}$ is the extinction efficiency. The extinction efficiency in the Rayleigh regime is given by the following relation [16]:

$$Q_{e\lambda} = 4\alpha\,\text{Im}\left\{\frac{m^2-1}{m^2+2}\left[1 + \frac{\alpha^2}{15}\left(\frac{m^2-1}{m^2+2}\right)\frac{m^4+27m^2+38}{2m^2+3}\right]\right\} + \frac{8}{3}\alpha^4\left|\left(\frac{m^2-1}{m^2+2}\right)\right|^2 \tag{7}$$

where the extinction efficiency $Q_{e\lambda}$ term shown above contains two terms - the absorption efficiency $Q_{a\lambda}$ and scattering efficiency $Q_{s\lambda}$ as shown below

$$Q_{a\lambda} = 4\alpha \,\mathrm{Im}\left\{\frac{m^2-1}{m^2+2}\left[1+\frac{\alpha^2}{15}\left(\frac{m^2-1}{m^2+2}\right)\frac{m^4+27m^2+38}{2m^2+3}\right]\right\} \tag{7a}$$

$$Q_{s\lambda} = \frac{8}{3}\alpha^4\left|\left(\frac{m^2-1}{m^2+2}\right)\right|^2 \tag{7b}$$

By examining Eq. (7b) it is evident that the scattering efficiency $Q_{s\lambda}$ varies as the fourth power of particle size. In addition, it is found that absorption efficiency $Q_{a\lambda}$ predominantly varies almost linearly with particle size. This is true even though there is a α^2 term inside the imaginary term of Eq. (7a) because $\alpha \leq 1$. This α^2 term does have a small influence. Further, by substituting Eqs. (4) and (7) into Eq. (6), the following expression for $K_{e\lambda}$ is obtained:

$$K_{e\lambda} = \frac{12\pi f_v}{\lambda}\,\mathrm{Im}\left\{\frac{m^2-1}{m^2+2}\left[1+\frac{\pi^2 D^2}{15\lambda^2}\left(\frac{m^2-1}{m^2+2}\right)\frac{m^4+27m^2+38}{2m^2+3}\right]\right\} + \frac{8\pi^4 D^3 f_v}{\lambda^4}\left|\left(\frac{m^2-1}{m^2+2}\right)\right|^2 \tag{8}$$

where the extinction coefficient $K_{e\lambda}$ contains two terms-the absorption coefficient $K_{a\lambda}$ and scattering coefficient $K_{s\lambda}$ as shown below

$$K_{a\lambda} = \frac{12\pi f_v}{\lambda}\,\mathrm{Im}\left\{\frac{m^2-1}{m^2+2}\left[1+\frac{\pi^2 D^2}{15\lambda^2}\left(\frac{m^2-1}{m^2+2}\right)\frac{m^4+27m^2+38}{2m^2+3}\right]\right\} \tag{8a}$$

$$K_{s\lambda} = \frac{8\pi^4 D^3 f_v}{\lambda^4}\left|\left(\frac{m^2-1}{m^2+2}\right)\right|^2 \tag{8b}$$

Finally, using Eqs. (5) and (7) the radiative properties of the nanofluid were evaluated. The net extinction caused by the nanofluid was obtained by adding the individual contributions from the nanoparticles (copper) as well as the base fluid (water). The intensity distribution within the solar collector iss obtained using:

$$\frac{\partial I_\lambda}{\partial y} = -K_{e\lambda,nanofluid}\,\tau I_\lambda = -\left(K_{a\lambda,water} + K_{e\lambda,nanoparticles}\right)\tau I_\lambda \tag{8c}$$

where, $K_{a\lambda,water}$ and $K_{e\lambda,nanoparticles}$ are obtained from Eqs. (3) and (6) respectively. When the volume fraction of nanoparticles is low the contributions of nanoparticles and base fluid (water) could be added together as shown in Eq. (8c). This is because the present model assumes independent scattering, where the scattered radiations do not depend on one another and hence the intensities can be added. Once the intensity distributions were evaluated, the energy balance on the solar collector is performed and the temperature profile within it is obtained. In order to carry out these steps, some assumptions are made.

The nanofluid is assumed incompressible and the flow is considered to be laminar. It is taken that water and nanoparticles are in thermal equilibrium and no slip occurs between them. The density of the nanofluid is approximated by the Boussinesq model. Only steady state case is considered. The governing equations for forced convection through a direct absorption solar collector in terms of the Navier-Stokes and energy equation (dimensionless form) are given as:

$$\frac{\partial U}{\partial X} + \frac{\partial V}{\partial Y} = 0 \tag{16}$$

$$U\frac{\partial U}{\partial X} + V\frac{\partial U}{\partial Y} = -\frac{\rho_f}{\rho_{nf}}\frac{\partial P}{\partial X} + \frac{\nu_{nf}}{\nu_f}\frac{1}{Re}\left(\frac{\partial^2 U}{\partial X^2} + \frac{\partial^2 U}{\partial Y^2}\right) \tag{17}$$

$$U\frac{\partial V}{\partial X} + V\frac{\partial V}{\partial Y} = -\frac{\rho_f}{\rho_{nf}}\frac{\partial P}{\partial Y} + \frac{\nu_{nf}}{\nu_f}\frac{1}{Re}\left(\frac{\partial^2 V}{\partial X^2} + \frac{\partial^2 V}{\partial Y^2}\right) \tag{18}$$

$$U\frac{\partial\theta}{\partial X}+V\frac{\partial\theta}{\partial Y}=\frac{1}{RePr}\frac{\alpha_{nf}}{\alpha_f}\left(\frac{\partial^2\theta}{\partial X^2}+\frac{\partial^2\theta}{\partial Y^2}\right)-Q \quad (19)$$

The above equations are non-dimensionalized by using the following dimensionless dependent and independent variables:

$$X=\frac{x}{L},\ Y=\frac{y}{L},\ U=\frac{u}{U_{in}},\ V=\frac{v}{U_{in}},\ P=\frac{p}{\rho_f U_{in}^{\ 2}},\ \theta=\frac{(T-T_{in})k_f}{qL} \quad (15)$$

$Pr=\frac{\nu_f}{\alpha_f}$ is the Prandtl number, $Re=\frac{U_{in}L}{\nu_f}$ is the Reynolds number and, $Q=\frac{k_f}{U_i qL\left(\rho C_p\right)_{nf}}\frac{\partial q_r}{\partial Y}$ is the dimensionless radiative heat flux parameter.

The energy equation is coupled to the Radiative Transport Equation (RTE) through the divergence of the radiative flux $\frac{\partial q_r}{\partial y}=\int_\lambda K_{e\lambda}\tau I_\lambda d\lambda$.

Also, $\rho_{nf}=(1-\phi)\rho_f+\phi\rho_s$ is the density,

$\left(\rho C_p\right)_{nf}=(1-\phi)\left(\rho C_p\right)_f+\phi\left(\rho C_p\right)_s$ is the heat capacitance,

$\alpha_{nf}=k_{nf}/\left(\rho C_p\right)_{nf}$ is the thermal diffusivity,

In the current study, the viscosity of the nanofluid is considered by the Pak and Cho correlation [17]. This correlation is given as $\mu_{nf}=\mu_f\left(1+39.11\phi+533.9\phi^2\right)$ (16)

and the thermal conductivity of Maxwell Garnett (MG) model [18] is

$$k_{nf}=k_f\frac{k_s+2k_f-2\phi\left(k_f-k_s\right)}{k_s+2k_f+\phi\left(k_f-k_s\right)} \quad (17)$$

The corresponding boundary conditions are:

at all solid boundaries: $U = V = 0$

at the upper wall: $\frac{\partial\theta}{\partial Y}=-\frac{k_f}{k_{nf}}$

at the inlet boundary: θ = 0, U = 1

at the outlet boundary: convective boundary condition P = 0

at the bottom wall: $\frac{\partial\theta}{\partial Y}=0$

The local and average Nusselt number (*Nu*) at the top surface can be written as

$\overline{Nu}=-\frac{k_{nf}}{k_f}\frac{\partial\theta}{\partial Y}$ and $Nu=\int_0^1\overline{Nu}\ dX$ respectively.

Heatfunction ξ is obtained from conductive heat fluxes $\left(-\frac{\partial\theta}{\partial X},-\frac{\partial\theta}{\partial Y}\right)$ as well as convective heat fluxes (Uθ, Vθ). It satisfies the steady energy balance equation such that $U\theta-\frac{\partial\theta}{\partial X}=\frac{\partial\xi}{\partial Y},\ V\theta-\frac{\partial\theta}{\partial Y}=-\frac{\partial\xi}{\partial X}$ (20)

The entropy generation in the flow field is caused by the non-equilibrium flow imposed by boundary conditions. In the convection process, the entropy generation is due to the irreversibility caused by the heat transfer phenomena and fluid flow friction. According to Bejan [10], the dimensional local entropy generation, s_{gen}, can be expressed by:

$$s_{gen}=\frac{k_{nf}}{T_0^2}\left[\left(\frac{\partial T}{\partial x}\right)^2+\left(\frac{\partial T}{\partial y}\right)^2\right]+\frac{\mu_{nf}}{T_0}\left[2\left(\frac{\partial u}{\partial x}\right)^2+2\left(\frac{\partial v}{\partial y}\right)^2+\left(\frac{\partial u}{\partial x}+\frac{\partial v}{\partial y}\right)^2\right] \quad (21)$$

where $T_0 = \frac{T_{col} + T_{in}}{2}$.

In equation (21), the first term represents the dimensional entropy generation due to heat transfer ($s_{gen,h}$), while the second term represents the dimensional entropy generation due to viscous dissipation ($s_{gen,v}$). By using dimensionless parameters presented in Eq. (14), the expression of the nondimensional entropy generation, S_{gen} can be written by:

$$S_{gen} = s_{gen} \frac{T_0 L^2}{k_f \left(T_{col} - T_{in}\right)^2}$$

$$= \frac{k_{nf}}{k_f}\left[\left(\frac{\partial \theta}{\partial X}\right)^2 + \left(\frac{\partial \theta}{\partial Y}\right)^2\right] + \chi \frac{\mu_{nf}}{\mu_f}\left[2\left(\frac{\partial U}{\partial X}\right)^2 + 2\left(\frac{\partial V}{\partial Y}\right)^2 + \left(\frac{\partial U}{\partial X} + \frac{\partial V}{\partial Y}\right)^2\right] \quad (22)$$

$$= S_{gen,h} + S_{gen,v}$$

Where $S_{gen,\,h}$ and $S_{gen,\,v}$ are the dimensionless entropy generation for heat transfer and viscous effect respectively. In Eq. (22), χ is the irreversibility factor which represents the ratio of the viscous entropy generation to thermal entropy generation. It is given as:

$$\chi = \frac{T_0 \mu_f}{k_f} \frac{U_i^2}{\left(T_{col} - T_{in}\right)^2}$$

The dimensionless average entropy generation, S for the entire computational domain is as follows:

$$S = \frac{1}{\overline{V}} \int S_{gen}\, d\overline{V} = S_{gen,h,m} + S_{gen,v,m}$$

where $\overline{V}$ is the volume occupied by the nanofluid and $S_{gen,\,h,\,m}$ and $S_{gen,\,v,\,m}$ are the average entropy generation for heat transfer and viscous effect respectively. The Bejan number, *Be*, defined as the ratio between the entropy generation due to heat transfer by the total entropy generation, is expressed as

$$Be = \frac{S_{gen,h,m}}{S}$$

It is known that the heat transfer irreversibility is dominant when *Be* approaches to 1. When *Be* becomes much smaller than 1/2 the irreversibility due to the viscous effects dominates the processes and if *Be* = 1/2 the entropy generation due to the viscous effects and the heat transfer effects are equal [11].

A measure of a collector performance is the collector efficiency (η) defined as the ratio of the useful energy gain to the incident solar energy which can be written as:

$$\eta = \frac{\text{useful gain}}{\text{available energy}} = \frac{mC_p\left(T_{out} - T_{in}\right)}{AI}$$

where m is the mass flow rate of the fluid flowing through the collector; C_p is the specific heat at constant pressure and T_{in} and T_{out} are the inlet and outlet fluid temperatures, respectively.

3. NUMERICAL IMPLEMENTATION

The Galerkin finite element method (Taylor and Hood [19]) is used to solve the non-dimensional governing equations along with boundary conditions for the considered problem. The equation of continuity has been used as a constraint due to mass conservation and this restriction may be used to find the pressure distribution. In the Eqs. (16) - (18), the pressure P is eliminated by a constraint. The continuity equation is automatically fulfilled for large values of this constraint. Then the velocity components (U, V) and temperature (θ) are expanded using a basis set. The Galerkin finite element technique yields the subsequent nonlinear residual equations. Three points Gaussian quadrature is used to evaluate the integrals in these equations. The non-linear residual equations are solved using Newton–Raphson method to determine the coefficients of the expansions. The convergence of solutions is assumed when the relative error for each variable between consecutive iterations is recorded below the

convergence criterion such that $\left|\psi^{n+1}-\psi^{n}\right| \le 10^{-4}$, where n is the number of iteration and Ψ is a function of U, V and θ.

3.1 GRID INDEPENDENT TEST

An extensive mesh testing procedure is conducted to guarantee a grid-independent solution for Re = 600 and Pr = 6.6 in a solar collector. In the present work, we examine five different non-uniform grid systems with the following number of elements within the resolution field: 48, 192, 768, 1616 and 3072. The numerical scheme is carried out for highly precise key in the average Nusselt number for water-Cu nanofluid (ϕ = 3%) as well as base fluid (ϕ = 0%) for the aforesaid elements to develop an understanding of the grid fineness as shown in Fig. 3. The scale of the average Nusselt numbers for nanofluid and clear water for 1616 elements shows a little difference with the results obtained for the other elements. Hence, considering the non-uniform grid system of 1616 elements is preferred for the computation.

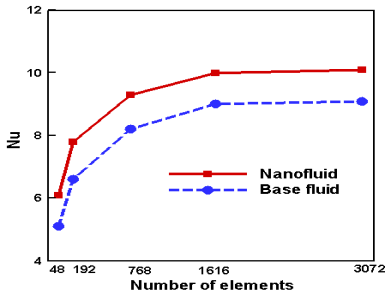

Fig. 3: Grid Independent Test

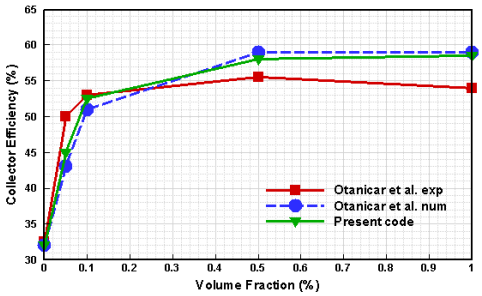

Fig. 4: Comparison of collector efficiency between present code and Otanicar et al. [5] at I = 1000 W/m^2 and flow rate 42 ml/h

3.2 CODE VALIDATION

The present numerical technique is validated by comparing the current code results for collector efficiency (%) – volume fraction (%) profile of water/graphite nanofluid for 30 nm spherical graphite nanoparticles with the graphical representation of Otanicar et al. [5]. They used direct absorption solar thermal collector at irradiation level I = 1000 W/m^2 and mass flow rate = 42 ml/h, respectively, where values of modeling and experimental results was shown. Fig. 4 demonstrates the above stated comparison where the numerical solutions (present work and Otanicar et al. [5]) are in good agreement.

4. RESULTS AND DISCUSSION

In this section, numerical results of isotherms and heatfunction for various values of Reynolds number (Re) with Cu /water nanofluid in a direct absorption solar collector are displayed. The considered values of Re are 200, 400, 600, 800 and 1000, while the Prandtl number Pr = 6.6, solid volume fraction ϕ = 3%, the mass flow rate m = 0.015 (kg/s), solar irradiance I = 1000 W/m^2. In addition, the values of the average

and normalized Nusselt number, Bejan number, mean and normalized entropy generation and percentage of collector efficiency of the DASC are shown graphically.

The non-dimensional temperature and conductive-convective heat flux fields in terms of isothermal lines and heatlines are displayed in Fig. 5 (a)-(b) for the effect of Reynolds number *Re* from 200 to 1000. The strength of the thermal current activities and heat flux are much more activated with escalating *Re*. In the temperature distribution isothermal lines for different values of Reynolds number shows that at low value of *Re* (= 200), the temperature of the nanofluid rapidly reaches to the temperature of hot walls due to low velocity. With increasing Reynolds number, increment of temperature of water-copper nonofluid is happened slowly, as a result the isotherms are more compressed near the hot upper wall and exit boundary. The thermal boundary layer thickness enhances for the greater values of inertia force.

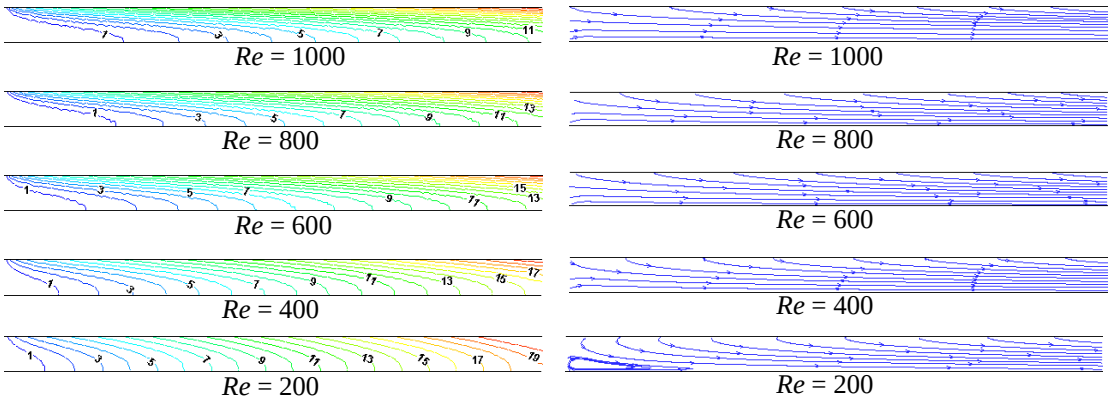

(a) Isotherms (b) Heatlines

Fig. 5: Effect of *Re* on (a) temperature and (b) heat function at ϕ = 3%

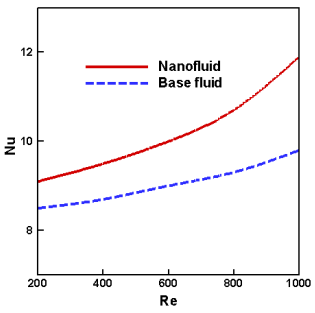

Fig. 6: Effect of *Re* on mean Nusselt number

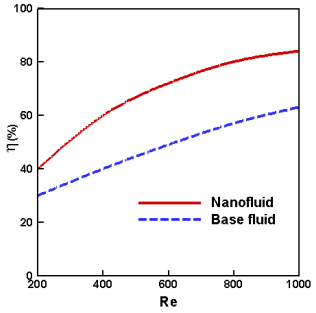

Fig. 7: Effect of *Re* on Collector efficiency

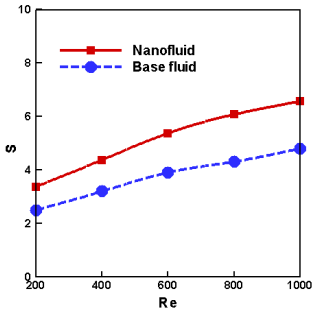

Fig. 8: Effect of *Re* on mean entropy generation

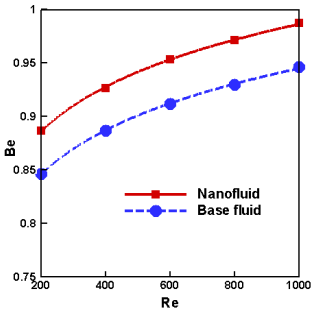

Fig. 9: Effect of *Re* on Bejan number

The heatlines illustrate that dominant inertia force effect plays a critical role on larger heat flow from upper wall to the passing fluid through the DASC. Heatlines also show that there is a clear difference in the heat flow trajectory for the influence of inertia force. This difference is largely attributed for *Re* = 1000 within the system. Deformation of heatlines near the upper portion of the computational domain is observed, showing the presence of forced convection in the system. However, the thermal mixing is not intense due to lower heat flow for *Re* = 200 as seen in Fig. 5 (b). Overall, larger heat may be recovered through the DASC for nanofluid with greater *Re*.

The *Nu*-*Re* profiles for water-Cu nanofluid as well as base fluid are depicted in Fig. 6. It is seen from the figure that average Nusselt number forms parabolic shape with mounting Reynolds number. The rate of forced convective heat transfer enhances 31% and 16% using nanofluid and water respectively for rising inertia force from 200 to 1000 while ϕ = 3%. The variation of percentage of collector efficiency as a function of the Reynolds number varies from 200-100 is exposed in Fig. 7. It is observed that by introducing greater inertia force the collector efficiency increases in parabolic form. More inertia force is able to augment heat loss system through the DASC. In this scheme water/copper nanofluid performs better than clear water. Collector efficiency enhances more than 2 times for increasing Reynolds number from 200 to 1000.

The variations of average entropy generation against Reynolds number is displayed in Fig.8. The entropy generation increases by Reynolds. The average entropy, for all considered values of *Re*, is higher with Cu-water and lower with water. As described above, under low Reynolds number conditions, the flow within the collector has only a low velocity and heat transfer is dominated by conduction effects. Therefore, the mean entropy generation (*S*) contributions of fluid friction irreversibility and heat transfer irreversibility, respectively, are both low, and thus *S* is also low. However, as the *Re* increases, the flow velocity within the collector increases and a larger temperature gradient is formed near the top wall surface and in the outlet. As a result, the effects of fluid friction irreversibility and heat transfer irreversibility in prompting mean entropy generation both increase. Consequently, the *S* increases rapidly. Fig.9 depicts the variations of Bejan number (*Be*) against Reynolds number. The Bejan number approaches unity, the fluid friction irreversibility effect can be ignored. In other words, mean entropy generation is dominated by the heat transfer irreversibility effect. Note that the Bejan number approaches unity for rising values of the Reynolds number for water/Cu nanofluid whereas for a particular *Re* lower *Be* is observed for base fluid. It is found that the heat transfer irreversibility is dominant since *Be* approaches to 1.

5. CORRELATION

From the current study the calculated average Nusselt number *Nu* and collector efficiency (%) η are correlated with Reynolds number (*Re*) and solid volume fraction (ϕ) with $0\% \le \phi \le 3\%$, $200 \le Re \le 1000$, *Pr* = 6.6 through the DASC. These correlations can be written as

$Nu = (3.442+0.157\phi)\,(Re)^{0.1528}$

where the confidence coefficient is $R^2 = 95.03\%$.

6. CONCLUSION

The influences of Reynolds number on forced convection flow inside the DASC with water-Cu nanofluid are accounted. Various *Re* have been considered for the temperature and heat flux fields as well as heat transfer rate, percentage of collector efficiency, mean entropy generation and Bejan number of the fluids through the collector. The results of the numerical analysis lead to the following conclusions:

- The structure of isotherms and heatlines through the solar collector is found to significantly depend upon the *Re*.
- The Cu nanoparticles with the highest *Re* are established to be most effective in enhancing performance of heat loss rate.
- The rate of heat transfer enhances 31% with the variation of *Re* .

- Collector efficiency enhances more than 2 times for increasing Reynolds number
- Mean entropy generation is obtained higher for rising *Re*.
- Bejan number approaches to 1 for Reynolds number variation.

REFERENCES

[1] A.R Taylor, E.P. Phelan, P.T. Otanicar, A.C. Walker, M.Nguyen, S. Trimble, P. Ravi, Int. J. of Renew. and Sust. Energy, 3, 023104, 2011.
[2] A.R. Taylor, E.P. Phelan, P.T. Otanicar, R. Adrian, R. Prasher, Nanoscale Research Letters, 6, 225, 2011.
[3] V. Verma, L. Kundan, Thermal performance evaluation of a Direct Absorption Flat Plate Solar Collector (DASC) using Al_2O_3-H_2O based nanofluids, IOSR J. of Mech. and Civil Engg. 6, 2, 29-35, 2013.
[4] H. Tyagi, P. Phelan, R. Prasher, J. of Solar Energy Engg., 131, 4, 041004, 7 pages, 2009.
[5] T.P. Otanicar, P.E. Phelan, R.S. Prasher, G. Rosengarten, and R.A. Taylor, J. of Renew. and Sustain. Energy 2, 033102, 2010.
[6] O. Mahian, A. Kianifar, S.A. Kalogirou, I. Pop, S. Wongwises, Int. J. of Heat and Mass Trans. 57 582–594, 2013.
[7] E. Zambolin, Scuola di Dottorato di Ricerca in Ingegneria Industriale, Indirizzo Fisica Tecnica, 2011.
[8] R. Nasrin, M.A. Alim and A.J. Chamkha, Heat Transfer—Asian Research, 42 1, 73-88, 2013
[9] A. Álvarez, M.C. Muñiz, L.M. Varela, O. Cabeza, Int. Conf. on Renew. Energies and Power Quality, Granada, 2010. (Spain).
[10] A. Bejan, Boca Raton:CRC Press;1996.
[11] H. Khorasanizadeh M, Nikfar. J, Amani, Eur J Mech B-Fluid, 37,143–152, 2013.
[12] CC.Cho, CL.Chen, CK. Chen., Int. J. of Heat and Mass Transf., 61, 749-758, 2012.
[13] R. Anandalakshmi, R.S. Kaluri, T. Basak, Energy 36, 4879-4896, 2011.
[14] T. Basak, G. Aravind, S. Roy, a.R. Balakrishnan, Int. J. of Heat and Mass Trans. 53, 3615–3628, 2010.
[15] E.B. Ogut, , Int. J. of Thermal Sci., 48, 11, 2063-2073, 2009.
[16] C. F. Bohren, and D. R. Huffman, Wiley, New York, 1983.
[17] B.C. Pak, Y. Cho, Experim. Heat Trans. 11, 151-170, 1998.
[18] J.C. Maxwell-Garnett, Philos. Trans. Roy. Soc. A 203, 385-420, 1904.
[19] C. Taylor, P. Hood, Computer and Fluids 1, 73–89, 1973.

VISCOELASTIC FLUID FLOW THROUGH A VERTICAL PLATE WITH DIFFUSION-THERMO AND THERMAL-DIFFUSION

Sheikh Imamul Hossain and Md. Mahmud Alam[**]
Mathematics Discipline, Khulna University, Khulna-9208, Bangladesh
Email: [**]alam_mahmud2000@yahoo.com, [*]s.imamul.ku@gmail.com

ABSTRACT: The finite difference solution of viscoelastic fluid flow through a porous medium along a semi-infinite vertical plate with diffusion-thermo and thermal-diffusion has been investigated. The above problem has been also considered for small magnetic Reynolds number. To obtain the non-dimensional, non-similar coupled momentum, energy and concentration equations, usual non-dimensional variables have been used. The obtained non-dimensional equations have been solved by explicit finite difference method. It has been also analyzed the stability and convergence criteria. The effects of the various parameters entering into the problem on the velocity, temperature, and concentration are shown graphically.

Keywords: Viscoelastic Fluid; Diffusion-thermo; Thermal-diffusion; Explicit Finite Difference.

1. INTRODUCTION

The viscoelastic fluid has been received momentum in the recent past because of its numerous applications in polymer technology, metallurgy, polymer sheet extrusion from a dye, polymer processing industry in particular in manufacturing process of artificial film. The study of boundary layer flow of a viscoelastic fluid through a vertical plate in the presence of Soret and Dufour's effect has wide range of applications in the field of chemical engineering and production of synthetic sheets. This is consequential to the production of heavy crude oils by means of thermal process. These oils considered as viscoelastic fluid which has both viscous and elastic property. Rajagopal et al. [1] studied the boundary layer flow of a viscoelastic fluid over a stretching sheet. The Soret and Dufour's effect described by Fourier's and Fick's laws respectively which are neglected in many studies because of their smaller order of magnitude. However, Eckert and Drake [2] have showed many cases where Dufour effect cannot be neglected. In this regards, Tsai and Huang [3] investigated the heat and mass transfer for Soret and Dufour's effects on Hiemenz flow through porous medium onto a stretching surface. Recently Damseh and Shannak [4] analyzed that the Visco-elastic fluid flow past an infinite vertical porous plate in the presence of first-order chemical reaction. Sreekanth et al. [5] studied about hydromagnetic natural convection flow of an incompressible viscoelastic fluid between two infinite vertical moving and oscillating plates. Very recent Gbadeyan et al. [6], examined heat and mass transfer for Soret and Dufour's effect on mixed convection boundary layer flow over a stretching vertical surface in a porous medium filled with a viscoelastic fluid in the presence of magnetic field.

Our aim is to extend the work of Gbadeyan et al. [6] for unsteady case and to solve the problem by explicit finite difference method. In this paper, the work has been done with the effects of both thermal and mass diffusion on two dimensional unsteady flow of an incompressible viscoelastic fluid through a vertical plate.

2. MATHEMATICAL MODEL OF FLOW

Consider the unsteady two-dimensional laminar flow of an incompressible viscoelastic fluid (obeying second grade model) through a vertical plate with Soret and Dufour's effects. The positive x coordinate is measured along the plate in the direction of fluid motion and the positive y coordinate is measured normal to the plate. The variable temperature T_w and variable concentration C_w at wall of the plate occupied with viscoelastic fluid of uniform ambient T_∞ and uniform ambient concentration C_∞. The physical configuration of the above problem is given in Fig. 1.

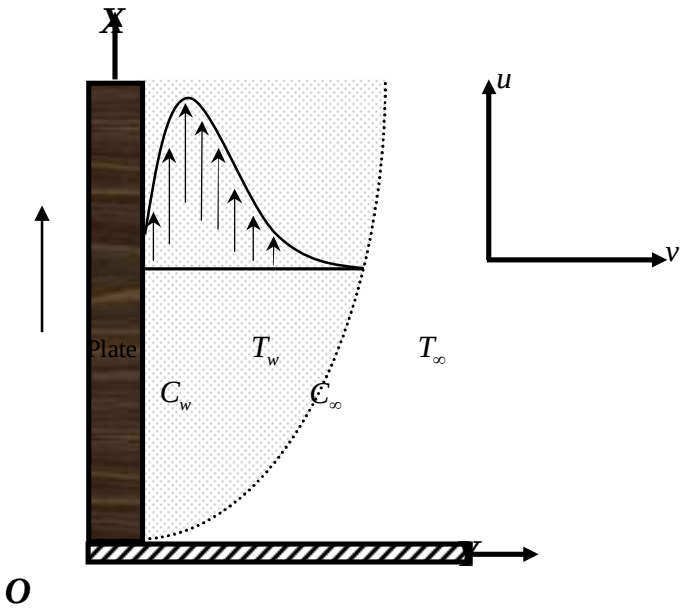

Fig.1. Physical configuration and coordinate system.

The basic governing equations are as follows;
The continuity equation;

$$\frac{\partial u}{\partial x}+\frac{\partial v}{\partial y}=0 \tag{1}$$

The momentum equation is as;

$$\frac{\partial u}{\partial t}+u\frac{\partial u}{\partial x}+v\frac{\partial u}{\partial y}=g\beta(T-T_\infty)+g\beta^*(C-C_\infty)+\upsilon\frac{\partial^2 u}{\partial y^2}+$$
$$\kappa_0\left[\frac{\partial^3 u}{\partial t\partial y^2}+u\frac{\partial^3 u}{\partial x\partial y^2}+v\frac{\partial^3 u}{\partial y^3}+\frac{\partial u}{\partial x}\frac{\partial^2 u}{\partial y^2}-\frac{\partial u}{\partial y}\frac{\partial^2 v}{\partial y^2}\right] \tag{2}$$

The energy equation;

$$\frac{\partial T}{\partial t}+u\frac{\partial T}{\partial x}+v\frac{\partial T}{\partial y}=\frac{k}{\rho c_p}\frac{\partial^2 T}{\partial y^2}+D_m\frac{\partial^2 C}{\partial y^2} \tag{3}$$

The concentration equation;

$$\frac{\partial C}{\partial t}+u\frac{\partial C}{\partial x}+v\frac{\partial C}{\partial y}=D_m\frac{\partial^2 C}{\partial y^2}+D_T\frac{\partial^2 T}{\partial y^2} \tag{4}$$

The initial and boundary conditions are;

$$u=U_0,\ v=0,\quad T=T_w,\quad \mathrm{C}=\mathrm{C}_w,\qquad \text{at y}=0 \tag{5}$$

$$u\to 0\ ,\frac{\partial u}{\partial y}\to 0\ ,T\to T_w, C\to C_w \text{ as }\ y\to\infty$$

where ρ is the density of the fluid, υ is the kinematic viscosity, g is the local acceleration due to gravity, D_m is the coefficient of mass diffusivity, D_T is the coefficient of the thermal diffusivity, α is the thermal diffusivity, κ is the thermal conductivity , U_0 is the uniform velocity. Also β is the volume expansion coefficient and β^* is the concentration expansion coefficient.
The dimensionless variables that are using in the equations (1)- (4)are as follows ;

$$X=\frac{xU_0}{\upsilon}, Y=\frac{yU_0}{\upsilon}, U=\frac{u}{U_0}, V=\frac{v}{U_0}, \tau=\frac{tU_0^2}{\upsilon}, \theta=\frac{T-T_\infty}{T_w-T_\infty}, \phi=\frac{C-C_\infty}{C_w-C_\infty}$$

Using these above dimensionless variables, the following dimensionless equations have been obtained as;

$$\frac{\partial U}{\partial X}+\frac{\partial V}{\partial Y}=0 \tag{6}$$

$$\frac{\partial U}{\partial \tau}+U\frac{\partial U}{\partial X}+V\frac{\partial U}{\partial Y}=G_r\theta+G_m\phi+\frac{\partial^2 U}{\partial Y^2}+K\left[\frac{\partial^3 U}{\partial \tau \partial Y^2}+U\frac{\partial^3 U}{\partial X\partial Y^2}+\frac{\partial U}{\partial X}\frac{\partial^2 U}{\partial Y^2}-\frac{\partial U}{\partial Y}\frac{\partial^2 V}{\partial Y^2}+V\frac{\partial^3 U}{\partial Y^3}\right] \tag{7}$$

$$\frac{\partial \theta}{\partial \tau}+U\frac{\partial \theta}{\partial X}+V\frac{\partial \theta}{\partial Y}=\frac{1}{P_r}\frac{\partial^2 \theta}{\partial Y^2}+D_u\frac{\partial^2 \phi}{\partial Y^2} \tag{8}$$

$$\therefore \frac{\partial \phi}{\partial \tau}+U\frac{\partial \phi}{\partial X}+V\frac{\partial \phi}{\partial Y}=\frac{1}{S_c}\frac{\partial^2 \phi}{\partial Y^2}+S_r\frac{\partial^2 \theta}{\partial Y^2} \tag{9}$$

The corresponding non-dimensional boundary conditions are as;

$$U=1,\quad V=0,\quad \theta=1,\quad \phi=1,\ \text{at}\quad Y=0 \tag{10}$$
$$U=0,\quad V=0,\quad \theta\to 0,\quad \phi\to 0,\ \text{as}\quad Y\to\infty$$

The non-dimensional quantities are; Grashof number, $G_r=\frac{\upsilon g\beta(T_w-T_\infty)}{U_0^3}$, Modified Groshof number, $G_m=\frac{\upsilon g^*\beta(C_w-C_\infty)}{U_0^3}$, Viscoelastic parameter, $K=k_0\frac{U_0^2}{\upsilon^2}$, Prandtl number, $P_r=\frac{\upsilon\rho c_p}{k}$, Dufour number, $D_u=\frac{D_m}{\upsilon}\frac{(C_w-C_\infty)}{(T_w-T_\infty)}$, Schmidt number, $S_c=\frac{\upsilon}{D_m}$, Soret number, $S_r=\frac{D_T}{\upsilon}\frac{(T_w-T_\infty)}{(C_w-C_\infty)}$.

3. NUMERICAL SOLUTIONS

To solve the governing second order nonlinear coupled dimensionless partial differential equations with the associated initial and boundary conditions by explicit finite difference method, it is required a set of finite difference equations. In this case, the region within the boundary layer is divided by some mash of lines parallel to X and Y axes where X – axis is taken along the plate and Y – axis is normal to the plate.

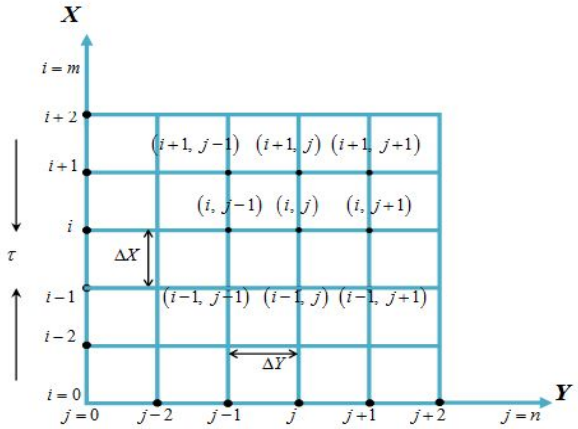

Fig. 2. Explicit finite difference system grid.

Here, the plate of height $X_{\max}=(100)$ i.e. X varies from 0 to 100 and regard $Y_{\max}=(35)$ as corresponding to $Y\to\infty$ i.e. Y varies from 0 to 35 have been considered. Consider $m=50$ and $n=50$ in X and Y directions. It is assumed that ΔX , ΔY are constant mesh sizes along X and Y directions respectively and taken as follows, $\Delta X=2(0\le x\le 100)$; $\Delta Y=.7(0\le y\le 35)$ with the smaller time-step, $\Delta\tau=0.005$.

Let U' , V' , θ' and ϕ' denote the values of U , V , θ and ϕ at the end of a time-step respectively. An appropriate set of finite difference equations have been obtained as;

$$\frac{U'_{i,j}-U'_{i-1,j}}{\Delta X}+\frac{V'_{i,j}-V'_{i,j-1}}{\Delta Y}=0 \tag{11}$$

$$\frac{U'_{i,j}-U'_{i,j}}{\Delta\tau}+U_{i,j}\frac{U_{i,j}-U_{i-1,j}}{\Delta X}+V_{i,j}\frac{U_{i,j+1}-U_{i,j}}{\Delta Y}=G_r\theta'_{i,j}+G_m\phi'_{i,j}+\frac{U_{i,j+1}-2U_{i,j}+U_{i,j-1}}{(\Delta Y)^2}$$
$$+K\left[\frac{U'_{i,j+1}-2U'_{i,j}+U'_{i,j-1}-U_{i,j+1}+2U_{i,j}-U_{i,j-1}}{\Delta\tau(\Delta Y)^2}\right.$$
$$+U_{i,j}\frac{U_{i,j+1}-2U_{i,j}+U_{i,j-1}-U_{i-1,j+1}+2U_{i-1,j}-U_{i-1,j-1}}{\Delta X(\Delta Y)^2}$$
$$+V_{i,j}\frac{U_{i,j+2}-3U_{i,j+1}+3U_{i,j}-U_{i,j-1}}{(\Delta Y)^3}+\frac{U_{i,j}-U_{i-1,j}}{\Delta X}\frac{U_{i,j+1}-2U_{i,j}+U_{i,j-1}}{(\Delta Y)^2}$$
$$\left.-\frac{U_{i,j+1}-U_{i,j}}{\Delta Y}\frac{V_{i,j+1}-2V_{i,j}+V_{i,j-1}}{(\Delta Y)^2}\right] \tag{12}$$

$$\frac{\theta'_{i,j}-\theta_{i,j}}{\Delta\tau}+U_{i,j}\frac{\theta_{i,j}-\theta_{i-1,j}}{\Delta X}+V_{i,j}\frac{\theta_{i,j+1}-\theta_{i,j}}{\Delta Y}=\frac{1}{P_r}\frac{\theta_{i,j+1}-2\theta_{i,j}+\theta_{i,j-1}}{(\Delta Y)^2}$$
$$+D_u\frac{\phi_{i,j+1}-2\phi_{i,j}+\phi_{i,j-1}}{(\Delta Y)^2} \tag{13}$$

$$\frac{\phi'_{i,j}-\phi_{i,j}}{\Delta\tau}+U_{i,j}\frac{\phi_{i,j}-\phi_{i-1,j}}{\Delta X}+V_{i,j}\frac{\phi_{i,j+1}-\phi_{i,j}}{\Delta Y}=\frac{1}{S_c}\frac{\phi_{i,j+1}-2\phi_{i,j}+\phi_{i,j-1}}{(\Delta Y)^2}$$
$$+S_r\frac{\theta_{i,j+1}-2\theta_{i,j}+\theta_{i,j-1}}{(\Delta Y)^2} \tag{14}$$

with initial and boundary conditions;

$$U^n_{i,0}=1,\ V^n_{i,0}=0,\ \theta^n_{i,0}=1,\ \phi^n_{i,0}=1 \tag{20}$$

$U^n_{i,L}=0$, $V^n_{i,L}=0$, $\theta^n_{i,L}=0$, $\phi^n_{i,L}=0$ Where $L\to\infty$.

Here the subscripts i and j designate the grid points with X and Y coordinates respectively and the subscript n represents a value of time, $\tau=n\Delta\tau$ where $n=0,1,2,3,\ldots\ldots\ldots$. The Stability conditions of the method are not shown brevity.

4. RESULTS AND DISCUSSION

The main goal of the computation is to obtain the steady- state solutions for the dimensionless velocity U , temperature θ and concentration ϕ for different values of dimensionless Soret number S_r and Dufour number D_u , viscoelastic parameter K , Schmidt number S_c , Grashof number G_r , modified Grashof number G_m , and Prandtl number P_r . For this purpose computations have been carried out up to dimensionless time $\tau=80$. The results of the computations, however, show little changes in the above mentioned quantities after dimensionless time $\tau=50$ have been reached. Thus the solutions for dimensionless time $\tau=50$ are essentially steady-state solutions.

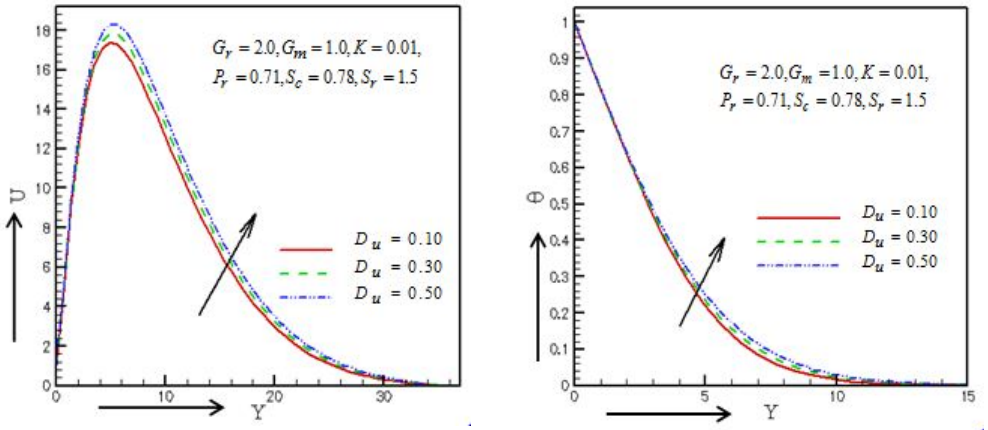

(a) (b)

Figs.3 (a) Velocity distributions and (b) Temperature distributions for different values of Dufuor number.

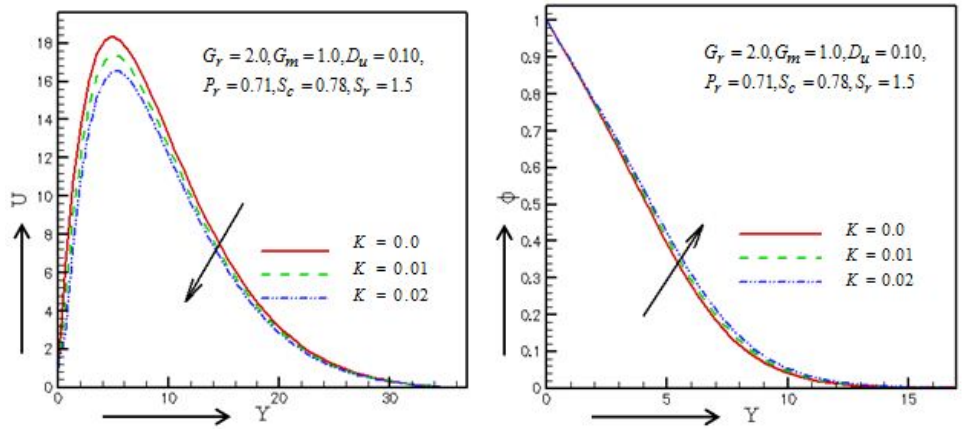

(a) (b)

Figs.4 (a) Velocity distributions and (b) Concentration distributions for different values of Viscoelastic parameter.

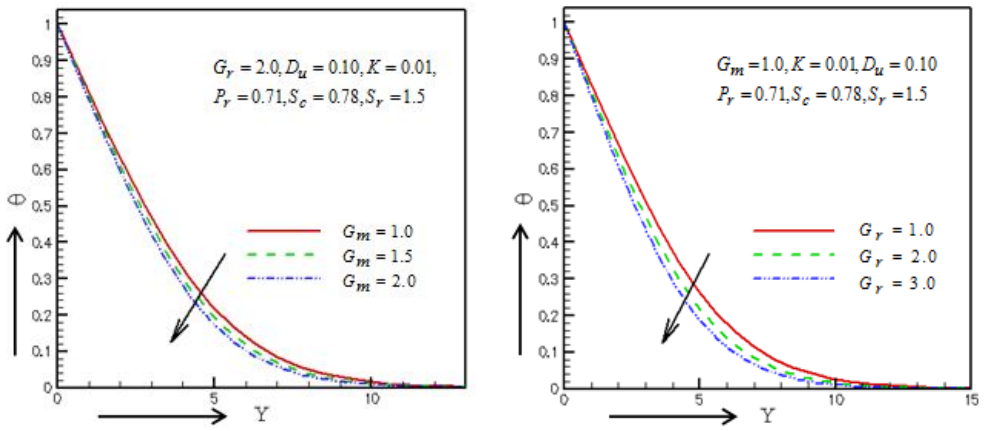

(a) (b)

Figs.5 (a) Temperature distributions for different values of Modified Grashof number and (b) Temperature distributions for different values of Grashof number.

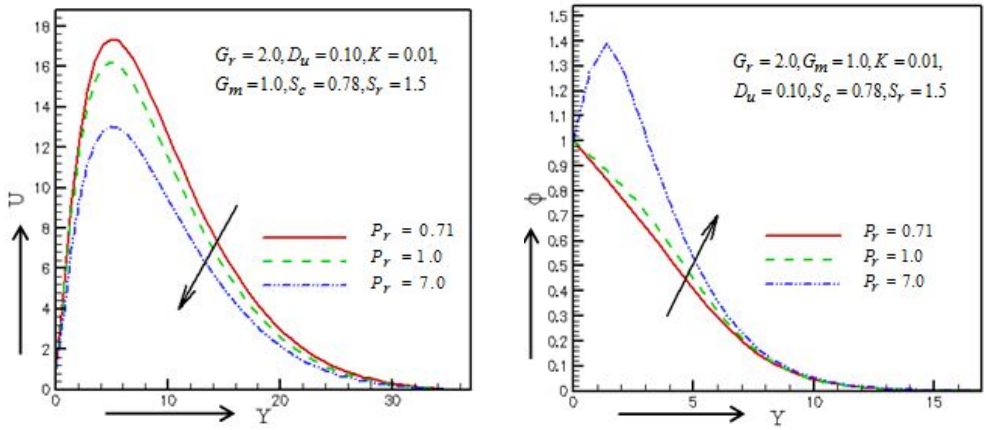

(a) (b)

Figs.6 (a) Velocity distributions and (b) Concentration distributions for different values of Prandtl number.

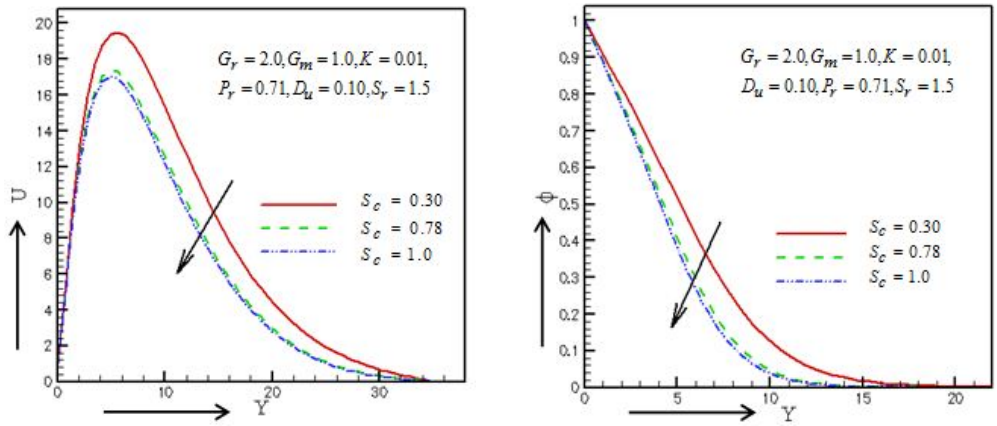

(a) (b)

Figs. 7(a) Velocity distributions and (b) Concentration distributions for different values of the Schmidt number.

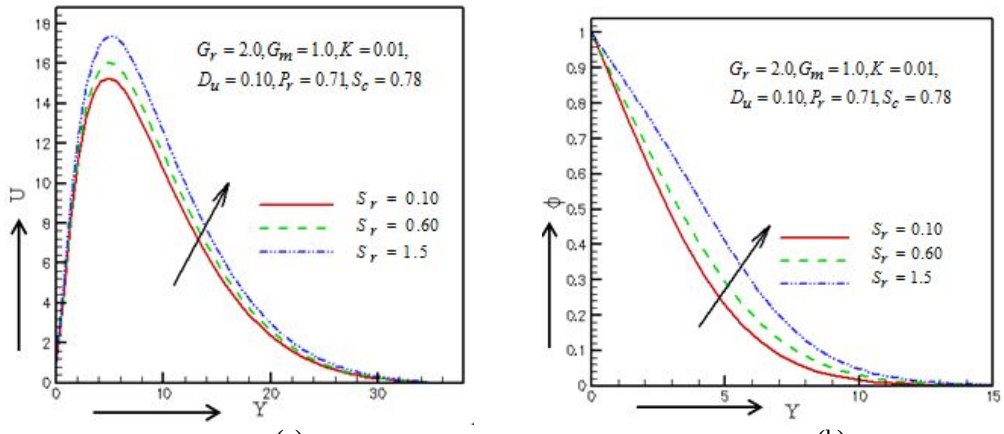

(a) (b)

Figs.8 (a) Velocity distributions and (b) Concentration distributions for different values of Soret number.

The velocity and temperature distributions have been shown in Figs. 3(a) and 3(b) for different values of Dufuor number D_u. Both the velocity and temperature distribution increase with the

increase of Dufuor number D_u. The velocity and concentration distributions have been shown in Figs. 4(a) and 4(b) for different values of Viscoelastic parameter K. The velocity distributions decrease with the increase of Viscoelatic parameter K while the concentration distributions increase with the increase of Viscoelastic parameter K. The temperature distributions have been shown in Figs. 5(a) and 5(b) for different values of Modified Grashof number G_m and Grashof number G_r respectively. Both the temperature distributions decrease with the increase Modified Grashof number G_m and Grashof number G_r respectively. The velocity distributions have been plotted in Figs. 6(a) and in Fig. 6(b) the concentration distributions have been plotted for different values of Prandtl nember P_r. The velocity distributions decreases with the increase of Prandtl number P_r while the concentration distributions increases with the increase of P_r. The velocity and concentration distributions have been shown in Figs. 7(a) and 7(b) for different values of Schmidt number S_c. Both the velocity and concentration distributions decrease with the increase of Schmidt number S_c. The velocity and concentration distributions have been shown in Figs. 8(a) and 8(b) for different values of Soret number S_r. Both the velocity and concentration distributions increase with the increase of Soret number S_r.

5. CONCLUSIONS

In this research work, the explicit finite difference solution of unsteady two-dimensional laminar flow of an incompressible viscoelastic fluid through a vertical plate with Soret and Dufour's effects has been studied. The physical properties are discussed for different values of various parameters and the accuracy of our results is qualitatively good in case of all the flow parameters. Some important findings of this study are given below;

1. For the increase of Dufuor number D_u, the velocity and temperature distributions have been increased.
2. For the increase Viscoelatic parameter K, Prandtl nember P_r and Schmidt number S_c, velocity distributions have been decreased.
3. Concentration distributions have been increased with the increase of Viscoelatic parameter K.
4. Temperature distributions have been decreased with the increase of Modified Grashof number G_m and Grashof number G_r.
5. Concentration distributions have been increased with the increase of Prandtl nember P_r and Soret number S_r.
6. Concentration distributions have been decreased with the increase of Schmidt number S_c.

REFERENCES

[1] K. R. Rajagopal, T. Y. Na, A. S. Gupta, (1984), "Flow of a viscoelastic fluid over a stretching sheet", Rheol. Acta. Vol. 23, pp 213-215.
[2] Eckert ER, Drake RM., (1972), "Analysis of heat and mass transfer" , McGraw Hill, New York.
[3] R. Tsai, J. S. Huang, (2009), "Heat and mass transfer for Soret and Dufour's effects on Hiemenz flow through porous medium onto a stretching surface", int. j. Heat Mass Transfer. vol. 52, pp2399-2406.
[4] R. A. Damseh and B.A. Shannak, (2010), "Visco-elastic fluid flow past an infinite vertical porous plate in the presence of first-order chemical reaction ", Appl. Math. Mech. -Engl. Ed. vol. 31(8), pp955–962.
[5] S.Sreekanth, S. Venkataramana, G. Sreedhar Rao and R. Saravana, (2011), "Hydromagnetic natural convection flow of an incompressible viscoelastic fluid between two infinite vertical moving and oscillating plates", Adv. Appl. Sci. Res., vol. 2(5), pp185-196.
[6] Gbadeyan, J.A., Idowu, A.S., Ogunsola, A.W., Agboola, O.O., Olanrewaju, P.O., (2011), "Heat and mass transfer for Soret and Dufour's effect on mixed convection boundary layer flow over a stretching vertical surface in a porous medium filled with a viscoelastic fluid in the presence of magnetic field", Global Journal of science Frontier Research, vol. 11(8), pp96-114.

ANALYTICAL SOLUTION OF BURGER'S EQUATION BY USING COLE-HOPF TRANSFORMATION

M.A.Awal Sheikh
Assistant professor, Department of Mathematics
University of South Asia, Banani, Dhaka, Bangladesh

Dr. Laek Sazzad Andallah
Professor, Department of Mathematics
Janhangirnagar University, Savar, Bangladesh

Dr. Md. Arefin Kowser
Associate Professor, Department of Mechanical Engineering
Dhaka University of Engineering and Technology (DUET), Gazipur, Bangladesh.

ABSTRACT: In this paper the analytical solution of Burger's equation [8, 14] has been presented. In order to understand the qualitative behavior of the analytical solution will provide good result of the scheme. For the presentation of analytical solution for burger's equation we present some important topics such as Cole-Hopf transformation, Cauchy problems from C-H transformation, the fundamental solution, solution of the Cauchy problem, uniqueness of analytical solution. In this work we present the numerical evaluation of analytical solution of inviscid Burger's equation for different time steps. We present the graph of the solution by choosing a suitable initial condition. In addition, we have calculated the magnitudes of derivative of solution analytically. We will show the performance and efficiency of the deterministic solutions of Burger's equation.

Keywords: Burger's equation, Finite difference schemes, Analytical solution, initial value problem.

1. INTRODUCTION

Burger's equation is mostly used to study the performance, stability and accuracy of different numerical methods used in solving the pde's obtained from Navier-Stokes equation. It has got an enormous amount of attention since the studies by J.M. Burger's in the 1940's, principally as a model Problem of the interaction between nonlinear and dissipative phenomena. In 1915, Harry Bateman considered a nonlinear equation whose steady solution was thought to describe certain viscous flows (Bateman, 1915), this equation had modeled a diffusive nonlinear wave which is now widely known as the Burgers' equation and is given by

$$u_t + uu_x = \nu uu_x \qquad (1)$$

Where υ is a constant measuring the viscosity of the fluid , it is a nonlinear parabolic equation , simply describing a temporal evolution where nonlinear convection and linear diffusion are combined and it can be derived as a nonlinear approximation to the equation of gas dynamics . Although the nonlinear equation (1) is very simple , and interest in it was revived in 1940, when Dutch physicist Jan Burgers proposed it to describe a mathematical model of turbulence in gas (Burgers,1940) , As a model for gas dynamics , it was then studied extensively by Burgers (1940), Enberhard Hopf (1950), Julian Cole (1951)and others , in particular , after the discovery of a coordinate transformation that map into the heat equation , while as a model for gas turbulence , the equation soon rivaled by more complicated models , the linear transformation just mentioned added importance to the equation as mathematical model, which has since been extensively studied .The limit $\nu \to 0$ is a hyperbolic equation , called the inviscid – Burger's equation

$$u_t + uu_x = 0 \qquad (2)$$

This limiting equation is important because it provides a simple example of conservation law; capturing the crucial phenomenon of shock formation indeed it was originally introduced as a model to describe the formation of shock waves in gas dynamics. Many numerical studies on turbulence flows have been conducted by solving Burger's equation, despite the fact that numerous investigations have been performed on the solution of Burger's equation. Only three solutions have employed in study of the theory.

A. Shock problem-the solution of Burger's equation exhibits 1-D shock weave feature. It should be remark that shock solutions are just the simple type solutions of Burger's equation.
B. Second solution is sine function which change either in time or space or both. This type of solution is driven by rather simple nonhomogeneous functions or initial condition if the nonhomogeneous function is zero
C. Random solution – This solution exhibits random feature like Burger's turbulence, if the nonhomogeneous function changes randomly in time the initial condition changes randomly in space with a zero nonhomogeneous function. The statistical properties of Burgers' turbulence have been investigated by many Authors.

In the present paper it is intended to present the analytical solution has been performed of Burger's equation via Cole-Hopf transformation using I.C: $u_0(x) = \sin x$ at different times steps.

2. COLE-HOPF TRANSFORMATIONS

We need to solve the following IV problem [9]

$$\frac{\partial u}{\partial t} + u\,\frac{\partial u}{\partial x} = \nu\,\frac{\partial^2 u}{\partial x^2} \tag{3}$$

With initial condition u(x, 0) = $u_0(x),\ for\ -\infty < x < \infty$ (4)

(3) Can be linearized by C-H transformation

$$u(x,t) = -2\nu\,\frac{\phi_x}{\phi} \tag{5}$$

We perform the transformation in two steps.

First let us assume $u = \varphi_x$ (6)

With this transformation (3) becomes,

$$\varphi_{xt} + \varphi_x\varphi_{xx} = \nu\,\varphi_{xxx}$$

$$\Rightarrow \varphi_{xt} + \frac{\partial}{\partial x}\left(\frac{1}{2}\varphi_x^2\right) = \nu\varphi_{xxx} \tag{7}$$

Now integrating the transformed equation w .r. to x then we have

$$\varphi_t + \frac{1}{2}\varphi_x^2 = \nu\varphi_{xx} \tag{8}$$

Then we make the transformation

$$\varphi = -2\nu\,\ln\,\phi \tag{9}$$

Which turns (8) into $\phi_t = \nu\phi_{xx}$ (10)

Which is the well-known first order PDE called heat or diffusion equation. Solving (5) for ϕ we have

$$\phi(x,t) = Ce^{-\frac{1}{2\nu}\int u\nu dx} \qquad For, t = 0,\ \phi(x,0) = Ce^{-\frac{1}{2\nu}\int u_0 x dx}$$

From (5), it is clear that C has no effect on our final solution of Burger's equation. So we can consider φ(x, 0) as

$$\phi(x,0) = e^{\frac{-1}{2\nu}\int_0^x u_0(z)\,dz} = \phi_0(x)(\,let\,) \tag{11}$$

3. CAUCHY PROBLEM FROM THE C-H TRANSFORMATION

After C-H transformation our problem turns into the following Cauchy problem for the heat equation [10]

$$\phi_t = \nu \phi_{xx} \tag{12}$$

$$\phi(x,0) = \phi_0 = e^{-\frac{1}{2\nu}\int_0^x u_0(z)dz} \tag{13}$$

This is a pure initial value problem

4. THE FUNDAMENTAL SOLUTION

In this section, we derive the fundamental solution and show how it is used to solve the above Cauchy problem [10].The heat equation has a scale invariance property that is analogous to scale invariance of the wave equation or scalar conservation laws, but the scaling is different.

Let a>0 be a constant. Under the scaling $x \rightarrow ax$, t$\rightarrow a^2 t$ the heat equation is unchanged. More precisely, if we introduce the change of variable in the form as $\bar{t} = a^2 t, x = ax$

Then the heat equation becomes $\phi_t = \nu \phi_{xx}$

This scale invariance suggests that weak solutions ν depending on the variable $\frac{x^2}{t^2} or \frac{x}{\sqrt{t}}$ however there is a property of the heat equation we would like to preserve in our similarity solution, that of conservation of energy. Suppose ϕ is a Solution of the heat equation with the property that $\left|\int_{-\alpha}^{\alpha} \phi(x,0)dx\right|$ <∞ and the another property such as $\phi(x,t) \rightarrow 0$ and as $x \rightarrow \infty$ then integrating the PDE it can be find that

$$\frac{d}{dt}\int_{-\infty}^{\infty} \phi(x,t)\,dx = 0 \tag{14}$$

The total heat energy is conserved

$$\int_{-\infty}^{\infty} \phi(x,t)\,dx = \text{Constant} \tag{15}$$

However $\int_{-\infty}^{\infty} w\left(\frac{x}{\sqrt{t}}\right)dx = t^2 \int_{-\infty}^{\infty} w(y)dy$ this suggests we should scale the function

$$\phi(x,t) = \frac{T}{\sqrt{t}} w\left(\frac{x}{\sqrt{t}}\right) \tag{16}$$

With the scaling, heat is conserved in the sense of (15) Substituting (16) into the PDE (12) leads an ODE for w=w(y) with non-constant coefficients.

$$\nu w'(y) + \frac{1}{2} y w(y) + \frac{1}{2} w(y) = 0 \tag{17}$$

Since this is a second order equation, we should have two independent solutions. First rewrite the ODE as

$$\nu w''(y) + \frac{1}{2}(y w(y)) = 0 \tag{18}$$

Thus $\nu w'(y) + \frac{1}{2} y w(y) = \text{Constant}$ (19)

Since we are really only seeking one solution, it is convenient to set the constant to zero, and write the solution of the homogeneous equation

$$W(y) = Ae^{\frac{y^2}{4\nu}} \tag{20}$$

Converting back to (x,t) with $y = \frac{x}{\sqrt{t}}$ we obtain the similarity solution

$$\phi(x,t) = A\frac{1}{\sqrt{t}}e^{-\frac{x^2}{4vt}} \tag{21}$$

Usually we choose a particular value of A so that the constant in (21) unity

i.e. $$1=\frac{A}{\sqrt{t}}\int_{-\infty}^{\infty} e^{-\frac{x^2}{4vt}}dx=\frac{2A}{\sqrt{t}}\int_{0}^{\infty} e^{-\frac{x^2}{4vt}}dx \tag{22}$$

Making the variable transformation $y=\frac{x^2}{4vt}$ we have

$$1=\frac{2A}{\sqrt{t}}\int_{0}^{\infty} e^{-y\frac{2vt}{\sqrt{4vty}}}dy=A\sqrt{4v}\sqrt{\pi} \tag{23}$$

The above term gives $$A=\frac{1}{\sqrt{4\pi v}} \tag{24}$$

For this choice of constant, we have the fundamental solution of the heat equation

$$\phi(x,t) = \frac{1}{\sqrt{4\pi vt}}e^{-\frac{x^2}{4vt}} \tag{25}$$

5. SOLUTION OF THE CAUCHY PROBLEM

The fundamental solution (23) satisfies (12) for t>0, Now $\phi(x-y,t)$ is a solution of (3.4a) for all y, by translation invariance we have $x = x - y$ does not change the heat equation. Thus, $\phi(x-y,t)\phi_0(y)$ is also a solution of (12). For later reference, we note that the heat equation is invariant under time translation also .By linearity and homogeneity of the PDE. We can also take the linear combinations of solutions. This suggests that $\phi(x,t) = \int_{-\infty}^{\infty}\varphi(x-y,t)\phi_0(y)dy$ (26)

The equation (26) should also be a solution. Moreover properties of φ suggests that

$t \to 0^+,\ \phi(x,t) \to \phi_0(x)$

$since \quad \phi(x-y,t)$

Collapse to zero away from $y = x$ and blows up at $y = x$ in such a way that the initial condition is satisfied in the sense $\phi(x,t) \to \phi_0(x)\ as\ t \to 0^+$

It is straight forward to check that the integrals for $\phi,\ \phi_t, \phi_{xx}$ all converge provided $g \varepsilon C(IR)$ is bounded.

Then $\phi_t = \int_{-\infty}^{\infty}\frac{\partial\Phi}{\partial t}(x-y,t)\phi_0(y)dy,\ \phi_{xx} = \int_{-\infty}^{\infty}\frac{\partial^2\phi}{\partial x^2}(x-y,t)\phi_0(y)dy$ (27)

So that u satisfies the PDE for t >0 It is more complicated to check the initial conditional is satisfied. We need to show $\phi(x,0) = \phi_0(x)$ But $t = 0$ is a singular point for ϕ: $\phi(x,t)$ is not

defined at $t = 0$ to get an idea of why $\lim_{t\to 0^+} \phi(x,t) = \phi_0$ let's fix x Then for

$$\delta \to 0\ \phi(x,t) = \int_{-\infty}^{\infty} \phi(x-y,t)\phi_0(y)dy = \int_{(x-y)\le\delta} \phi(x-y,t)\phi_0(y)dy + \int_{(x-y)\ge\delta} \phi(x-y,t)\phi_0(y)dy \quad (28)$$

$$= \int_{|x-y|\le\delta} \phi(x-y,t)\phi_0(y)dy$$

By continuity, $\phi_0(y) \approx \phi_0(x)$ for y near x, this explains how the first integral is approximately the final line. The second integral approaches to zero as $t \to 0$ because φ→0 uniformly, and exponentially away from $y = x$ as $t \to 0^+$

Finally we get the solution of the Cauchy problem described in(3) as follows

$$\phi(x,t) = \int_{-\infty}^{\infty} \phi(x-y,t)\phi_0(y)dy \quad (29)$$

Theorem 1 Let $\phi_0 \varepsilon C(R)$ be bounded and let $\phi(x,t)$ be given by the formula (26) then

1. $\phi \varepsilon C^{\infty}$ For t>0
2. Φ satisfies the heat equation such as

$$\phi_t = v\phi_{xx} \quad x \in R \quad \text{For t>0}$$

$$Lim\ (x,t) \to \phi(x_0,0)\ \phi(x,t) = \phi_0(x_0)\ \ for\ \ all\ \ x_0 \varepsilon R$$

3. Proof

Property 1 follows because φ is C^{∞} for t >0, and derivatives of φ all decay Exponentially as $|x| \to \infty$ so the integrals converge. Property follows from $\phi_t = v\phi_{xx}$ $x \in R$ for t>0

To prove property: 3 we look at the difference $|u(x,t) - g(x_0)|$, estimate and show that the pieces we get behave as we expect, i.e. in the rough argument preceding the proof. Let e □0 this measure the estimation and we have the relations as follows

$$|\phi(x,t) - \phi_0(x_0)|)\ \ then\ \ \sin ce\ \int \phi.dx = 1\ \ we\ \ have$$

$$|\phi(x,t) - \phi_0(x_0)| = \left| \int_{-\infty}^{\infty} \phi(x-y,t)(\phi_0(Y) - \phi_0(x_0))dy \right| \quad (30)$$

Let δ >0 and break the integrals in (30)

$$|\phi(x,t) - \phi_0(x_0)| \le \left| \int_{|x_0-y|\le\delta} \phi(x-y,t)(\phi_0(y) - \phi_0(x_0))dy \right| + \left| \int \phi(x-y,t)(\phi_0(y) - \phi(x_0)dy \right| \quad (31)$$

Now we use δ two ways to show the two integrals are small:

1st

$$\phi_0(y) \approx \phi_0(x).\ For\ y\ near\ \ x, \phi(x-y,t)\ blows\ up\ as\ t \to 0,$$

$$but \int \phi(x-y,t)dy\ is\ bounded\ uniformly\ \ by\ \ 1$$

2nd: $\int \phi(x-y,t)dy \to 0\ \ as\ \ t \to 0,\ \ provided\ |x - x_0| \le \frac{\delta}{2}\ \ while\ \ \phi_0(y)$ is bounded

We write the right hand sight of (29) as

$$I_{\delta} + J_{\delta}$$

Choose δ>0 so that $|\phi_0(y) - \phi(x_0)|$ <e for $|y - x_0|$ <δ

Then we have

$$I_\delta \le \int_{|x_{0-y}|\le\delta} \phi(x-y,t)|\phi_0(y)-\phi_0(x_0)| \le e \int_{|x_{0-y}|\le\delta} \phi(x-y,t)dy \le e$$

The second integral is some what trickier. Since ϕ_0 is bounded, there is k >0 such that $|\phi_0(y)| \le K$ for all y we find that

$$J_\delta \le \int_{|x_{0-y}|\ge\delta} \phi(x-y,t)|\phi_0(y)-\phi_0(x_0)|dy \le 2K\int \frac{1}{\sqrt{4\pi Kt}} e^{-\frac{(x-y)^2}{4Kt}} dy$$

Here is the second use of δ: Consider x satisfying $|x-x_0| \le \frac{\delta}{2}$. *Then* $|x-y| \ge \frac{\delta}{2}$

In the range of integration $|x_0 - y|$ >δ .But this is not a good enough estimate of the exponential, because we would still be left with an integral an infinite interval of a small but positive quantity. So we need to observe that region of integration,

$$|x-y| \ge \frac{1}{2}|y-x_0| \ \textit{Then} \ J_\delta \le \int_{|x_0-y|\ge\delta} \frac{1}{\sqrt{t}} e^{-\frac{x_0-)^2}{\sqrt{6kt}}} dy \le C\int e^{-z^2} dz$$ <e for t>0

Thus $|\phi(x,t)-\phi_0(x_0)|$ <2e for $|x-x_0| < \frac{\delta}{2}$, t>0 sufficiently small. This is clearly proved the property 3.The above theorem assures us that (29) is a solution of (3.4a) satisfying the initial condition (3.4b)

Using the expression for and ϕ_0 in (12), we finally get

$$\phi(x,t) = \frac{1}{\sqrt{4\pi kt}} \int_{-\infty}^{\infty} \exp\left[-\frac{(x-y)^2}{4\nu t} - \frac{1}{2\nu}\int_0^y u_0(z)dz\right] dy \qquad (32)$$

5.1 Analytical solution of the Burgers' equation

Differentiating (32) w.r.to.x we have

$$\phi_x = \frac{1}{\sqrt{4\pi kt}} \times \frac{-1}{2\nu t} \times \int_{-\infty}^{\infty} (x-y)\exp\left[-\frac{(x-y)^2}{4\nu t} - \frac{1}{2\nu}\int_0^y u_0(z)dz\right] dy$$

Now from (2) we have $u(x,t) = -2\nu\frac{\phi_x}{\phi}$

$$\Rightarrow u(x,t) = \frac{\int_{-\infty}^{\infty}(x-y)\exp\left[-\frac{(x-y)^2}{4\nu t} - \frac{1}{2\nu}\int_0^y u_0(z)dz\right]dy}{t\int_{-\infty}^{\infty}\exp\left[-\frac{(x-y)^2}{4\nu t} - \frac{1}{2\nu}\int_0^y u_0(z)dz\right]dy} \qquad (33)$$

5.2 Boundary values of the analytical solution

We find the values of the analytical solution with initial condition $u_0(x) = \sin(x)$ at the boundaries of the spatial domain $[0,\ 2\pi]$ which in further will be used as boundary conditions for numerical schemes.

For initial condition $u_0(x) = \sin x$ we get the analytical solution:

$$u(x,t)=\frac{\int_{-\infty}^{\infty}(x-y)\exp\left[-\frac{(x-y)^2}{4\nu t}+\frac{1}{2\nu}\cos y\right]dy}{t\int_{-\infty}^{\infty}\exp\left[-\frac{(x-y)^2}{4\nu t}+\frac{1}{2\nu}\cos y\right]dy} \quad (34)$$

For x=0 (34) gives

$$u(0,t)=\frac{\int_{-\infty}^{\infty}(-y)\exp\left[-\frac{y^2}{4\nu t}+\frac{1}{2\nu}\cos y\right]dy}{t\int_{-\infty}^{\infty}\exp\left[-\frac{y^2}{4\nu t}+\frac{1}{2\nu}\cos y\right]dy} \quad (35)$$

The numerator of (2) is an odd function, so we must have u (0, t) =0
Now for $x=2\pi$ we have

$$u(2\pi,t)=\frac{\int_{-\infty}^{\infty}(2\pi-y)\exp\left[-\frac{(2\pi-y)^2}{4\nu t}+\frac{1}{2\nu}\cos y\right]dy}{t\int_{-\infty}^{\infty}\exp\left[-\frac{(2\pi-y)^2}{4\nu t}+\frac{1}{2\nu}\cos y\right]dy} \quad (36)$$

Making the variable change $z=2\pi-y$, we have

$$u(2\pi,t)=\frac{\int_{-\infty}^{\infty}z\exp\left[-\frac{(z)^2}{4\nu t}+\frac{1}{2\nu}\cos z\right]dz}{t\int_{-\infty}^{\infty}\exp\left[-\frac{(z)^2}{4\nu t}+\frac{1}{2\nu}\cos z\right]dz} \quad (37)$$

The function under integration sign in the numerator of (4) is an odd function
So we have

$$\int_{-\infty}^{\infty}z\exp\left[-\frac{z^2}{4\nu t}+\frac{1}{2\nu}\cos z\right]dz=0 \quad (38)$$

This implies that $u(2\pi,t)=0$.So we have the boundary values

$$u(0,t)=u(2\pi,t)=0 \quad (39)$$

This boundary value is very important for analytical solution

5.3 Numerical evaluation of analytical solution of Burger's equation

Let us consider the initial condition $u_0(x)=\sin(x)$ over a bounded space $[0 \quad 2\pi]$ at different time steps. For the initial condition we use the analytical solution of (37) of burgers equation in equation (39) we observe that both in numerator and denominator ν is a factor in finding the solution of burgers' equation .For very small v then equation (37) get more closed to zero
Or get larger which becomes very difficult to handle. So considering the value of v arbitrarily very small and there is another problem of calculating of u near initial time .We observe from (37) that for small t both numerator and denominator get much closed to zero and thus difficult to handle numerically. We have got the behavior of the solution at three different times. Now we are interested how our analytical solution behaves when we try to implement it graphically by using the computer programming code

The analytical solution of Burgers' equation is:

$$u(x,t) = -2v\frac{\phi_x}{\phi} \quad \Rightarrow u(x,t) = \frac{\int_{-\infty}^{\infty}(x-y)\exp\left[-\frac{(x-y)^2}{4vt} - \frac{1}{2v}\int_0^y u_0(z)dz\right]dy}{t\int_{-\infty}^{\infty}\exp\left[-\frac{(x-y)^2}{4vt} - \frac{1}{2v}\int_0^y u_0(z)dz\right]dy} \tag{40}$$

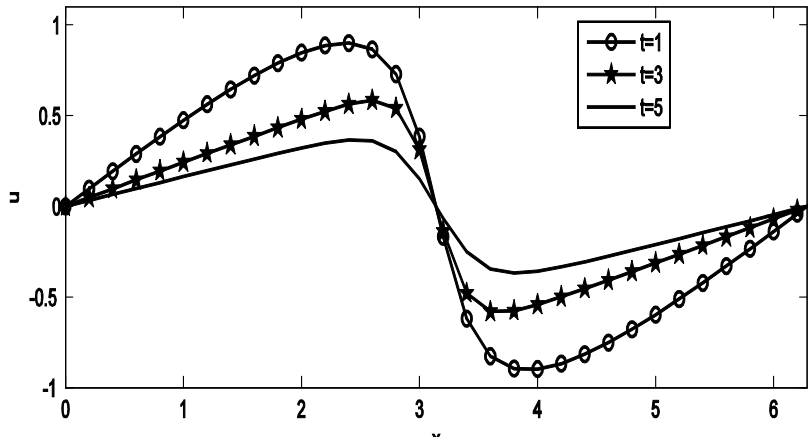

Figure 1: Analytical solution of viscid Burger's equation at=1, 3, 5

5.4 Analytical solution of Burger's equation at=10

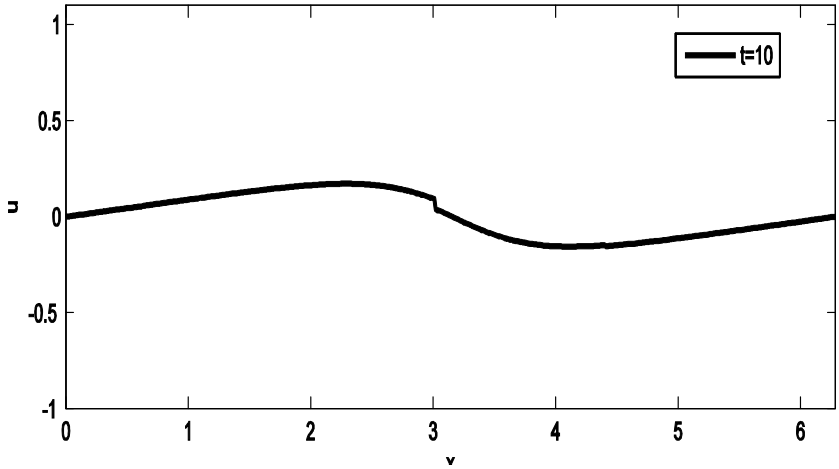

Figure 2: Analytical solution of Burger's equation at=10

5.5 Numerical evaluation of analytical solution of inviscid Burger's equation

Considering the initial condition $u_0(x) = \sin(x)$, we get the following solutions:

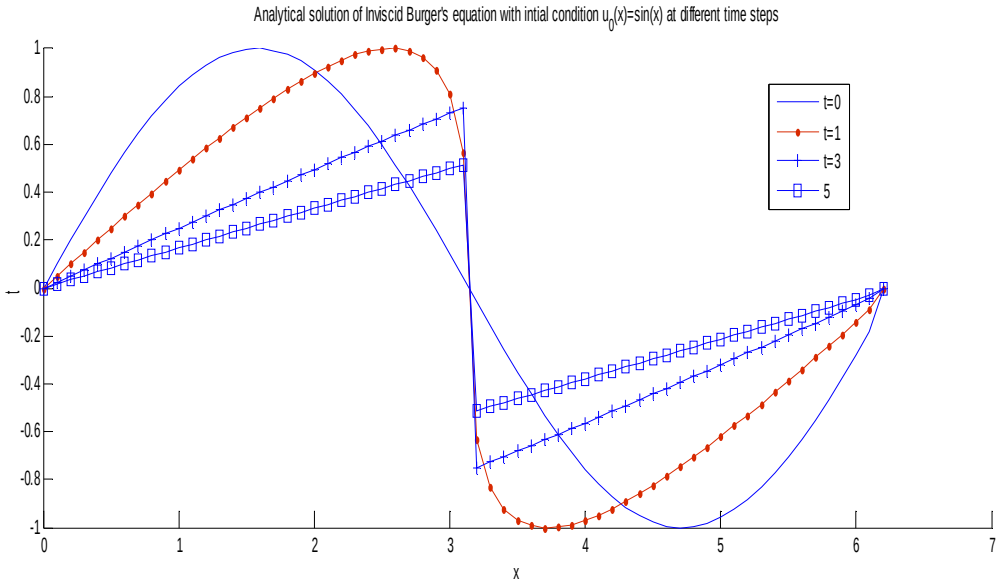

Figure 3: The analytical solution of inviscid burger's equation with initial condition $u_0(x) = \sin(x)$ at different time steps

From Figure 3 it is clear that the curve is more flatten as time grow we observe that after a certain amount of time the solution becomes discontinuous at $x = \pi$ .It would happen because since at the left neighborhood of $x = \pi$ the flow is in positive direction and at the right neighborhood of $x = \pi$ the flow is in negative direction so for flow without viscosity we must get a discontinuity at $x = \pi$

6. CONCLUSION

In this paper, Cole-Hopf transformation has been derived by using a new model. Presented model can generate the solution of initial value $u(x,t)$ problem. We can observe that for a fixed x and t we may get many solutions if $u_0(x)$ is not an algebraic function. To get the solution of problem we first discretize time. Then in calculating the solution in a time step and we take the solution. The analytical solution of inviscid burger's equation with initial condition $u_0(x) = \sin(x)$ at different time steps, the figure exhibits that the curve is more flatten as time grow. We observe that after a certain amount of time the solution becomes discontinuous at $x = \pi$ .Burger's equation can be solved in implementing the generalized solution. Our goal has been interplay between nonlinear steeping and viscous diffusion wave of motion.

REFERENCES

[1] Mohamed A. Ramadan, Talaat S. EL-Danaf; Numerical treatment for the Modified Burger's equation-2005.
[2] P.L. Sachdev; A class of exact solutions of boundary value problems for Burger's equation.
[3] L.S. Andallah. Analytical & Numerical methods for PDE'' lecture note, Department of Mathematics.Jahangirnagar University-2010.
[4] L.S. Andallah. "Finite difference Difference Methods – Explicit upwind Difference scheme, lecture note Department of Mathematics-J.U.
[5] Randall J.Leveque,"Numerical Methods for Conservation Laws", second Edition -1992, Springer.
[6] F. Chorlton, "Fluid Dynamics" first Indian edition- 1985.
[7] Charles 1, Fefferman "Existence and smoothness of the Navier- Stokes Equation, Princeton University, Department of Mathematics Princeton

[8] J.D.Cole on a Quasilinear Parabolic Equation Occurring in Quart Appl Vol. 9, 225-236(1951)
[9] B.H.Batema, Some Recent Researches of the Motion of Fluid; Monthly Weather Rev,Vol. 43 pp.163-170.1915.
[10] A.R.Forsyth; Theory of differential equations. Vol 6. Cambridge Univ, press-1906.
[11] D.V Widder; The heat equation. Academic Press, 1975
[12] D.V.Widder, positive temperatures on an infinite rod Trans. Amer.Math, Sec. 55.(1944) pp. 85-86
[13] Stephanie Roy "1D Burgers' equation'',(hyb56)
[14] E.hopf, The partial Differential equation, Comm.

EXPERIMENTAL STUDY ON A MICROCONTROLLER BASED DIRECT GASOLINE FUEL INJECTION SYSTEM WITH HIGH TURBULENCE FUEL- AIR MIXING AND ENHANCED ENGINE SECURITY MEASURES

Md. Syed Ali Molla[1], Md. Shafiq Sayid[2], & Md. Al -Mamun[3],
[1] Dept. of M. E., Khulna University of Engineering & Technology (KUET), Bangladesh
[2] Motor Walla Ltd, USA
[3] BUET , Bamgladesh
E-mail: mmsali03@yahoo.com [1], *S.Sayid@gmail.com*[2] , *almamuneee07@gmail.com*[3]

ABSTRACT: The major advantages of a Direct Gasoline Fuel (GDI) engine are increased fuel economy and higher engine efficiency. Harmful emissions levels can also be controlled accurately with the GDI system. The cited gains are achieved by the precise control over the amount of fuel injection and injection timings that are varied according to engine load and operating conditions. In addition, there are no throttling losses in some GDI engines, when compared to a conventional fuel injection system, which greatly improves efficiency, and reduces 'pumping losses' in engines without a throttle plate. The Direct Gasoline Injection (DGI) technologies have the advantages over manifold fuel injection system and port fuel injection system for maximum fuel economy, and thereby it can minimize environmental pollution at an accessible price by harnessing the DGI's inherent advantages. DGI-technologies deliver a 10~30 % improvement in fuel economy over a current other model engine, along with enhanced drivability. The present research work has been modeled with different approach of direct gasoline fuel injection inside the cylinder at low pressure availing high turbulence air-fuel mixing in suction and compression stroke unlike presently used direct gasoline fuel injection system in SI engine. More over high coolant temperature and low oil pressure are the main causes of major failures in engine. This fuel injection system is designed and programmed with additional security measure in this DGI system. Here the fuel injection as well as engine will stop to avoid engine damage as soon as it receives signals from high coolant temperature and low oil pressure during engine operation.

Keywords: Direct gasoline fuel injection system (DGI), microcontroller, high turbulence , low pressure.

1. INTRODUCTION

The construction of the carburetor is relatively simple and it has been used almost exclusively on gasoline engines in the past. However, in response to recent demands for cleaner exhaust emissions, more economical fuel consumption, and improved drivability, the carburetor now must be equipped with various compensating devices and it makes carburetor more complex. In place of carburetor, therefore, the injection system is used, assuring the proper air-fuel ratio to the cylinder by using electronic controlling devices in accordance with various driving conditions. Compared with throttle body (TBI) and port fuel injection (PFI) systems, direct gasoline injection system (DGI) is more difficult and expensive. But the payback for the added complexity is higher torque, dramatically reduced emissions and increased engine efficiency. This is possible as fuel can be injected in the exact quantity, time and location that it's demand by the engine.

Engines generate their worst emissions-just after cold-start. During warm-up of a DGI engine, a small shot of fuel is injected just before the exhaust valve opens. There's still enough heat and oxygen in the chamber for this charge to ignite, and the heat from that after burn gets the catalyst up to operating temperature just seconds after cold-start. The injectors are either open or closed, and pulsed as in a port-injection system (PFI). Since the fuel flows directly into the combustion chamber instead of impinging on the intake valve, the nozzle can be designed to form a "cloud" of fuel with a specific size and shape [1]. The DGI-technologies can deliver a 10~30 % improvement in fuel economy over a current EFI-engine, along with enhanced drivability [1].

The engine management system continually chooses among three combustion modes: ultra lean burn, stoichiometric and full power output. Each mode is characterized by the air fuel ratio. The stoichiometric air-fuel ratio for gasoline is 14.7:1 by weight (mass), but ultra lean mode can involve ratios as high as 25:1 (or even higher in some engines, for very limited periods). These mixtures are much leaner than in a conventional engine and reduce fuel consumption considerably [2].

The 1955 Mercedes-Benz 300SL, the first production sports car to use fuel injection, used direct injection. The Bosch fuel injectors were placed into the bores on the cylinder wall used by the spark plugs in other Mercedes-Benz six-cylinder engines (the spark plugs were relocated to the cylinder head). Later, more mainstream applications of fuel injection favored the less-expensive indirect injection methods.

Toyota's D4 direct injection system first appeared on various Japanese market vehicles equipped with the SZ and NY engines [3-5]. Toyota later introduced its D4 system to European markets with the *1AZ-FSE* engine found in the 2001 Avenis [6] and US markets in 2005 with the *3GRE-FSE* engine found in the *Lexus GS 300*. Toyota's *2GR-FSE* V6 first found in the Lexus IS 350 uses a more advanced direct injection system, which combines both direct and indirect injection using two fuel injectors per cylinder, a traditional port fuel injector (low pressure) and a direct fuel injector (high-pressure) in a system known as D4-S [6].

Renault introduced the 2.0 IDE (Injection Directe Essence) [7], first on the Megane. Rather than following the lean burn approach in 1999. Renault's design uses high ratios of exhaust gas recirculation to improve economy at low engine loads, with direct injection allowing the fuel to be concentrated around the spark [8]. Later gasoline direct injection engines have been tuned and marketed for their high performance as well as increased fuel efficiency. PSA Peugeot Citrogen, Hyundai, and Volvo entered into a development agreements and licensed Mitsubishi's GDI technology in 1999 [9-13]. The Mitsubishi engines were also produced in the NetCar factory and used in the 1.8 L Carisma and the GDI-powered Volvo S40/V40 models [14-15].

In 2002, the Alfa Romeo 156 with a direct-injection engine, the JTS (Jet Thrust Stoichiometric) went on sale[16] and today the technology is used on almost every Alfa Romeo engine. Infiniti produced the M56 which includes DI. Motus Motorcycles is developing, with Katech Engines, a direct-injected V4 engine named the KMV4 as the powertrain for their MST Motorcycle. In 2011 the Hyundai Snonata 2011 model l came with GDI engines, including a turbo-charged 2.0-litre that produces 274 hp. Hyundai's Theta I-4 engine family is a proprietary design, engineered in Namyang, Korea and currently in production for applications all over the world [17]

MM Syed Ali et al. carried out experimental investigation in on direct fuel injection system in 2010 and found that fuel injection quantity can be varied with engine speed and load [18]. M. M. Syed Ali et al. also took research investigations [19-20] on single cylinder EFI System and 4 cylinder Port Fuel Injection System where fuel could be controlled according to engine demands.

M.M. Syed Ali also investigated with a different model for a low pressure DGI System instead of existing high pressure DGI model considerating several advantages. Instead of high pressure fuel injection system Low Pressure DGI System was modeled for a 4 cylinder SI engine where air fuel mixing gets high turbulence and long duration for air fuel mixing. This can provide better fuel air mixing before combustion. The experimental investigation [21] showed fuel air ratio at different operating condition can be maintained to achieve high fuel economy and less pollution formation specially carbon monoxide (CO) and hydrocarbon (HC) pollutants..

2. LAYOUT AND COMPONENTS OF A DGI SYSTEM

The fuel delivery system incorporates the following components:
(i) Fuel tank, (ii) Fuel pump (iii) Fuel filter (iv) Fuel delivery pipe (rail) (v) Pulsation damper (in many engines) (vi) Fuel injectors (vii) Cold start injectors (most engines) (viii) Fuel pressure regulator etc.

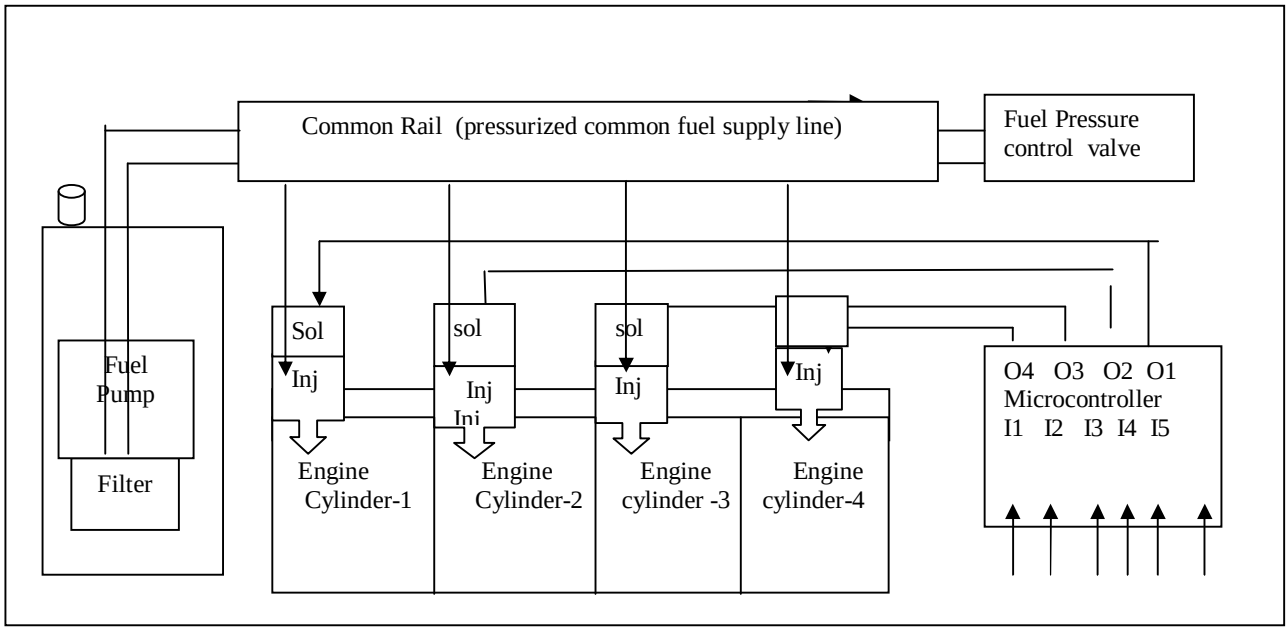

Fig. 1: Fuel supply in direct gasoline injection (DGI) system

Usually fuel injection pressure in DGI system is nearly 40 times higher than the fuel injection pressure in EFI system. Fuel injection at low pressure is preferred considering several advantages in system. There are two types of electric fuel pump used in the EFI systems. The early conventional EFI system used an externally mounted in-line pump. These roller cells pumps incorporate an integral pressure pulse damper or silencer designed to smooth out pressure pulses and provide quiet operation. Later model engines utilize an in-tank pump integrated with the fuel sender unit. These turbine pumps operate with less discharge pulsation and run quieter than the in-line variety. In-tank pumps can be serviced by removing the fuel sender unit from the tank. In this case intake turbine pump has been selected and used.

Injector:
In a direct fuel injection engine, the fuel must be injected in a short period of time and at pressures at least 40 times higher than in port fuel injection [4]. The electric fuel pump supplies the fuel to the injectors under pressure. As soon as the injector opens, fuel sprays out. An electric solenoid in the injector opens and closes the injector.

High pressure fuel injector in the present DGI System

Low Pressure fuel injector in the test model of DGI

Fig. 2: Fuel injector

In this investigation low pressure fuel injectors are taken considering fuel injection at low pressure inside the cylinder and availing high turbulence air-fuel mixing. This can enhance homogeneous air fuel mixture and can reduce CO and HC pollutions. More over the cost of fuel pump and injectors will be reduced considerably.

3. DESIGN CONSIDERATIONS AND PROGRAM ON MICROCONTROLLER

A microcontroller has been built with an ATMega 28 IC for controlling device. DGI system was designed for variable speed and variable load and other operating conditions of a real engine.
The engine management system usually continually chooses among three combustion modes: ultra lean burn, stoichiometric, and full power output. Each mode is characterized by the air-fuel ratio. The stoichiometric air-fuel ratio for petrol (gasoline) is 14.7 to 1 by weight, but ultra lean mode can involve ratios as high as 25:1. These leaner mixtures of DGI system is much leaner than in a conventional engine, reduce fuel consumption [4].

In this design instead of three mode six modes of engine operation with specially, staring (choke circuit) idle circuit, slow speed circuit, medium speed circuit, high-speed circuit, acceleration circuit. In each running condition there is provision of extra fuel supply for high load and low load operation so that wide varying of fuel air ratio can be supplied keeping in conformity of engine operation conditions. Various types of sensors, ICs and transistors are used to sense the speed and suction pressure and engine operating conditions

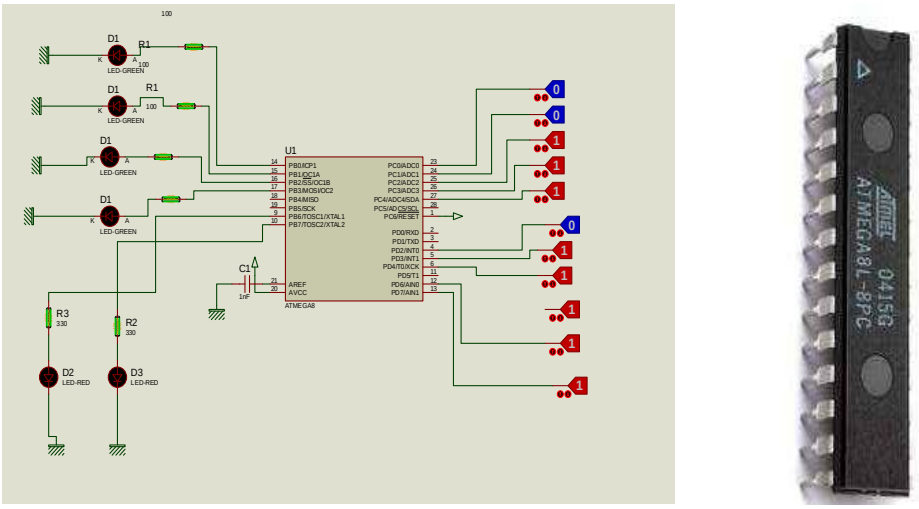

Fig. 3: Microcontroller IC and input output diagram.

An engine demand various quantity of air depending on load and speed. The intake air flow and air pressure represents the variation of load. The distributor of EFI and DGI systems have built in signaling system for engine rpm and crank angle position. Ne – signal and Ge-signal give engine rpm and crank angle position. Oxygen signal fitted in Catalytic converter give presence of oxygen in exhaust gas which in term give information to the engine that it is running with lean or rich or with optimum fuel air ratio. The program was made on the logics required for operating conditions of the engine. The air velocity and pressure in the intake manifold can determine the loading position in each mode. The Oxygen sensor gives the level of fuel air ratio. All these parameter are set to the program to get required output signal for fuel flow injector.

Before programming on a microcontroller based DGI system, the fuel air ratio required in all engine operating conditions like starting system (choke system), idle system, slow speed, medium speed, high speed system, acceleration system with variable engine load are considered accordingly the required input are set to microcontroller. The output of microcontroller controls the injectors, where the fuel injection quantity varies depending on engine operating conditions.

3. Experimental Setup

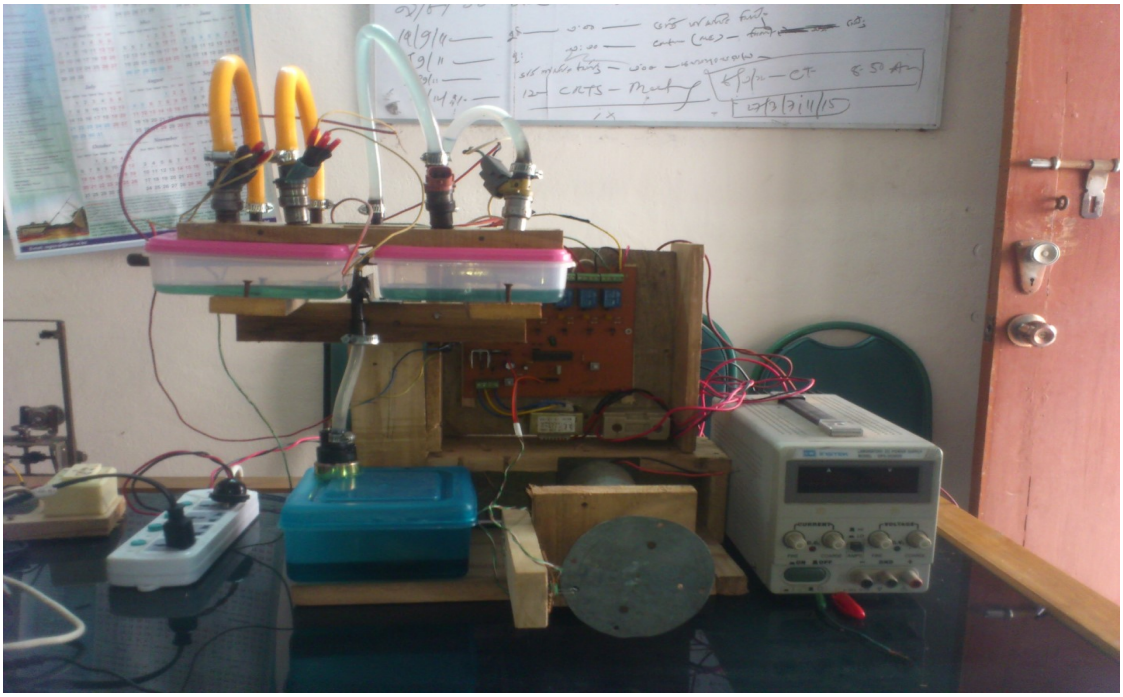

Fig. 4: Experimental set up for low pressure direct gasoline injection (DGI) system

4. RESULTS & DISCUSSION

After completion of the experimental set-up of the fuel injection system, the performance of the direct gasoline fuel injection system was tested. The fuel injection quantity can be varied to any required quantity depending upon engine load and speed. Moreover the fuel injection is found to be stopped as soon as it receive signals from high coolant temperature and low oil pressure during engine operation. This will immediately stop the engine avoiding major damage of crankshaft, crankshaft bearing, piston and piston-rings etc.

This module can be used in other model like EFI or Port Fuel Injection system vehicle with small modification. Carburetor vehicle with electronic distributor has the facility to give engine speed (rpm), crank angle position. In other word carburetor mounted vehicle with electronic distributor can be modified to this system where the amount of fuel to be supplied from injector to engine cylinder in all engine operation modes can be controlled by this microcontroller.

5. CONCLUSION

At the end, it may be concluded that-

(i) The microcontroller based Low pressure direct fuel injection system is found to work properly.

(iii) The model test showed that variable fuel injection quantity at different speed and load can be maintained.

(iv) There more opportunity of homogeneous air-fuel inside the cylinder during high turbulence phase in suction and compression stroke. This can help to reduce the formation of carbon monoxide (CO) and hydrocarbon (HC) pollution during combustion of fuel- air mixture..

(v) The emission reduction potential is very high as fuel injection can be controlled depending upon the engine running condition.

(vi) Fuel delivery cost of module of DGI system is nearly 1500-2000 USD in US market but this microcontroller based module costs early 20-25 USD.

(vii) The introduction of low pressure direct gasoline fuel injection system will also reduce the cost of presently used high pressure direct fuel injection system.

REFERENCES

[1] W. H, Crouse and D, L. Anglin, "Automotive Mechanics", 10th revision/McGraw-Hill Book Company, USA
[2] Fuel Systems at Sears® | Sears.com
[3] 30_39-Jfl/'Ý,,v" (PDF). Retrieved 2009-07-17.
[4] "D4English". Alflash.com.ua. Retrieved 2009-05-16.
[5] Visnic, Bill (1996-09-01). "Direct-injection coming for the masses". Wardsautoworld.com. Retrieved 2012-06-21.
[4] www.Sears.com/Fuel-System-Services
[5] JEGS.com/Electric
[6] "Improving the Environmental Performance of Internal Combustion Engines — Engine". Toyota. 1999-02-22. Retrieved 2009-08-21.
[7] Crouch, Jonathan. "Renault Megane Cabriolet 1997-2003". uk.cars.yahoo.com. Archived from the original on 2011-07-18. Retrieved 2012-06-21.
[8] Wan, Mark (2000). "Lean Burn Engine". Autozine Technical School. Retrieved 2010-11-14.
[9] Yamaguchi, Jack (2000-02-01). "Mitsubishi's new GDI applications". Automotive Engineering International (highbeam). Retrieved 2013-09-09.
[10] Beecham, Matthew (2007-12-07). "Research Analysis: a review of gasoline direct injection systems". Just-Auto. Retrieved 2013-09-09.
[11] "Mitsubishi Motors and PSA Peugeot Citroen Reach Agreement on GDI Engine Technical Cooperation" (Press release). Mitsubishi Motors. 1999-01-12. Archived from the original on 2009-01-12. Retrieved 2013-09-08.
[12] "Mitsubishi Motors Supplies Hyundai Motor Co. with GDI Technology for New V8 GDI Engine" (Press release). Mitsubishi Motors. 1999-04-28. Archived from the original on 2009-01-12. Retrieved 2013-09-08.
[13] Motor Business Japan. Economist Intelligence Unit. 1997. p. 128. Retrieved 2013-09-09. "Hyundai is second only to Volvo among companies borrowing the technology from Mitsubishi."
[14] Japan Quarterly 46. Asahi Shimbun. 1999. p. 22. Retrieved 2013-09-09.
[15] "Not so nuts" (98). AutoSpeed. 2000-09-19. Retrieved 2013-09-09.
[16] "News 2002". italiaspeed.com. Retrieved 2007-10-24.
[17] Abuelsamid, Sam (2009-11-13). "New Hyundai 2.4-liter GDI four cylinder makes 200 hp in 2011 Sonata". AOL Inc. Retrieved 2010-11-14.
[18] M. M. Syed Ali, Husnay Mobarok and Md. Mominul Haque " Experimental study on a program controlled direct gasoline fuel injection (DGI) system in SI engine for variable speed and load", Undergraduate project thesis 2010, Department of Mechanical Engineering , KUET, Khulna, Bangladesh.
[19] M. M. Syed Ali,; Rubel Shikder,; Md. Jahirul Islam, "Development of a Microcontroller based EFI System f**or** a Single Cylinder Four SI Engine**," Undergraduate project thesis, Department of** Mechanical Engineering, Khhulna University of Engineering & Technology, Khulna-9203, Bangladesh, 2012-2013.